

2024

# Strategies for molecular junctions with expanded degrees of freedom

---

<https://hdl.handle.net/2144/50039>

*"Downloaded from OpenBU. Boston University's institutional repository."*

BOSTON UNIVERSITY  
GRADUATE SCHOOL OF ARTS AND SCIENCES

Dissertation

**STRATEGIES FOR MOLECULAR JUNCTIONS WITH  
EXPANDED DEGREES OF FREEDOM**

by

**BRENT LAWSON**

A.S. Marine Science, Southern Maine Community College, 2014  
B.S. Physics, University of New Hampshire, 2018  
B.S. Chemistry, University of New Hampshire, 2018

Submitted in partial fulfillment of the  
requirements for the degree of  
Doctor of Philosophy

2024



Approved by

First Reader

---

Maria Kamenetska, Ph.D.  
Assistant Professor of Physics  
Assistant Professor of Chemistry

Second Reader

---

Shyamsunder Erramilli, Ph.D.  
Professor of Physics

Third Reader

---

Alexander Sushkov, Ph.D.  
Associate Professor of Physics

## **DEDICATION**

I would like to dedicate this to Colleen.

## ACKNOWLEDGMENTS

I would like to thank my advisor, Prof. Masha Kamenetska. I am grateful that she allowed me to pursue the projects that interested me ranging from building an STMBJ to implementing and learning new computational methods and theories. It has made my time during my Ph.D. interesting and unexpected and made me a more well-rounded scientist. I am also grateful to all of the times she has been there to help when things take unexpected turns and have to be done last minute. I am glad I decided to come to Boston University and got to be a part of her lab.

Thank you to my dissertation defense committee: Prof. Shyamsunder Erramilli, Prof. Karl Ludwig, Prof. Qiang Cui, Prof. Alexander Sushkov, and Prof. Kevin Smith. I especially want to thank my committee for being flexible especially with last minute changes before my defense. I would also like to thank and acknowledge the assistance, advice, and guidance from collaborators: Dr. Percy Zahl (Brookhaven National Laboratory) for operating the UHV-LT-STM, Dr. Mark Hybertsen (Brookhaven National Laboratory) for guidance on DFT, Prof. Michael Haley (University of Oregon) for discussions associated with their molecules as well as Efrain Vidal (University of Oregon) for synthesizing the molecules for the diradical project. I also want to thank Dr. James McNeely (Boston University) as well as Dr. Jan Wilhem (University of Regensburg) for teaching me how to do DFT calculations and being willing to answer my random questions throughout my Ph.D.

I also would like to thank everyone in the Kamenetska Lab: Dr. Hannah Skipper, Dr. Xiaoyun Pan, Daniel Jackson, Brian Dawes, Zelin Miao, Favian Liu, Freddy Luna,

Alona Maslennykov and Nick Miller. I especially want to mention my appreciation and enjoyment working with Dr. Hannah Skipper and Dr. Xiaoyun Pan over the course of multiple projects.

I also want to thank my whole family. Without them and their support throughout my whole life, I know that I would not have been able to get to this point. And finally, I have the deepest love and gratitude for my wife, Colleen, who has always been there to help me throughout my numerous degrees. I could not have gotten through my Ph.D. without you and all of your help and endless support. You are amazing and thank you. Oh, and thank you Ted Lasso.

**STRATEGIES FOR MOLECULAR JUNCTIONS WITH  
EXPANDED DEGREES OF FREEDOM**

**BRENT LAWSON**

Boston University, Graduate School of Arts and Sciences 2024

Major Professor: Maria Kamenetska, Assistant Professor of Physics and Chemistry

**ABSTRACT**

Increasing the degrees of freedom in molecule-metal junctions presents new opportunities for expanded functionality in molecular circuits and could pave the way to next generation electronics integrating single molecules as active components. For example, molecular junctions with spin degrees of freedom have been explored as a materials platform for Quantum Information Science (QIS). In this thesis, I present experimental and computational investigations of how incorporating transition metal atoms (Chapter 1), new oxygen-based linker groups (Chapter 2) and radical backbone elements (Chapter 3) into molecular junctions can expand the range of observable phenomena in molecular circuits.

In Chapter 1, I present a collaborative investigation of the nature of group 8 metallocenes, which can be prepared with a range of transition metal atoms at the center of the molecule, in molecular junctions formed at both cryogenic and room temperature. We characterize the direct gold- $\pi$  bonds between the molecule and the metal electrodes and their effect on molecular conductance during molecular junction evolution. Analysis of the junction persistence as well as conductance fluctuations reveals these metal containing “barrel-shaped” molecules preferentially bind to dull atomic electrode tips through van der

Waals interactions. We support our measurements by modeling different binding motifs within density functional theory (DFT). Interestingly, our study finds that for closed-shell metallocenes, the electrode-molecule interface and environmental conditions have by far larger influence on electron transport than the identity of the metal atom in the molecular backbone.

In Chapter 2, I report single molecule conductance measurements with a new phenol-based linker group involving the formation of a direct, single O-Au bond to anchor the molecule to the electrode. We find that deprotonation of the phenol is necessary for molecule-metal binding, enabling pH control of junction formation. The activation of metal-phenol binding through deprotonation is supported with DFT calculations that model the binding interaction before and after deprotonation. We determine that transport through phenol systems is mediated by the molecular HOMO orbital. Accurate quantitative predictions of the electron transport properties of phenol-based linkers require higher levels of corrections to DFT which underestimates the HOMO-LUMO gap, unless supplemented by DFT+ $\Sigma$  methodology. Crucially, our study establishes principles for achieving pH control of the metal-molecule interface for the molecular electronics community.

Last, I demonstrate experimentally and from first principles, the unique transport properties of a family of quinoidal cyclic aromatic hydrocarbons with intermediate diradical character. These molecules exhibit “anti-ohmic” conductance, with the longer molecules having greater single molecule conductance than shorter ones. This behavior is atypical of quantum tunneling commonly observed in molecular junctions. Unlike prior examples of diradicals in molecular junctions, these compounds do not require oxidation

or complex environments. We accurately model the electronic and conductance properties of these molecules by developing a modification to the 1D Su-Schrieffer-Heeger (SSH) model for cyclic quinoidal molecules with accurate experiment-based parameterization. The 1D SSH model suggests that the anti-ohmic behavior is typical of intermediate diradical molecules and predicts anti-ohmic trends across a broad range of molecular length regimes. Our work suggests the search for long range high conducting molecular wires should focus on molecules with neutral intermediate diradical character that have the increased benefit of stability, diversity, and experimental accessibility.

## TABLE OF CONTENTS

DEDICATION.....	iv
ACKNOWLEDGMENTS .....	v
ABSTRACT.....	vii
TABLE OF CONTENTS.....	x
LIST OF TABLES .....	xiii
LIST OF FIGURES .....	xiv
LIST OF ABBREVIATIONS.....	xxi
CHAPTER 1 Introduction.....	1
1.1 Motivation.....	1
1.2 Scanning Tunneling Microscope Break Junction (STMBJ) Technique .....	3
1.3 Fundamentals of Electron Transport.....	6
1.4 Anatomy of a Molecular Junction .....	8
1.4.1 Molecule Backbone .....	9
1.4.2 Linker Group.....	11
1.4.3 Electrodes.....	12
1.5 Thesis Outline .....	13
CHAPTER 2 Formation and evolution of metallocene single molecule circuits with direct gold- $\pi$ links .....	15
2.1 Introduction.....	15
2.3 Experimental Section .....	18
2.2.1 Molecular Deposition and Measurements in Cryogenic Conditions .....	18

2.2.2 Room Temperature Break Junction Measurements .....	20
2.2.3 Data Analysis .....	21
2.2.4 Data Filtering Details and Analysis .....	22
2.2.5 Density Functional Theory Calculations .....	24
2.3 Results and Discussion .....	25
2.3.1 Experimental Measurements.....	25
2.3.2 DFT Calculations .....	38
2.3.3 Discussion .....	48
2.4 Conclusion .....	52
CHAPTER 3 Phenol is a pH-activated linker to gold: a single molecule conductance	
study .....	54
3.1 Introduction.....	54
3.2 Methods .....	56
3.2.1 Break Junction Measurements .....	56
3.2.2 Theoretical Calculations .....	58
3.3 Results and Discussion .....	62
3.3.1 Experimental Measurements.....	62
3.3.2 Theoretical Calculations .....	72
3.4 Conclusions.....	77
CHAPTER 4 Topological Insulator Single Molecule Junctions with Intermediate	
Diradicals Result in Anti-ohmic Conductance .....	79
4.1 Introduction.....	79

4.2 Experimental Section .....	81
4.3 Results and Discussion .....	83
4.3 Conclusions.....	89
BIBLIOGRAPHY.....	91
List of Journal Abbreviations .....	91
References.....	93
CURRICULUM VITAE.....	120

## LIST OF TABLES

<b>Table 2.1</b> Number of remaining push and pull traces for both ferrocene and ruthenocene following each step in applying the filtering criteria. ....	23
<b>Table 2.2</b> Number of push and pull traces within each snapback bin range for both ferrocene and ruthenocene. ....	31
<b>Table 2.3</b> The calculated [HOMO and LUMO from] ionization potential (IP) and electron affinity (EA) based on total energy differences. Frontier orbital energy values from the SCF calculations. ....	40
<b>Table 3.1.</b> Calculated gas phase correction, $\Delta 1$ , used for DFT+ $\Sigma$ for $\text{NH}_2\text{C}_1\text{PhO}^-$ , $\text{NH}_2\text{C}_2\text{PhO}^-$ , $\text{NH}_2\text{C}_3\text{PhO}^-$ , and $\text{NH}_2\text{C}_4\text{PhO}^-$ . The calculated HOMO energy levels from Ionization Potential calculations ( $E_{\text{HOMO}}$ ) and the HOMO energy eigenvalue from KS-DFT ( $\epsilon_{\text{HOMO}}$ ) are also shown.....	60
<b>Table 3.2.</b> Calculated values for the image-charge correction term, $\Delta 2$ , for $\text{NH}_2\text{C}_1\text{PhO}^-$ , $\text{NH}_2\text{C}_2\text{PhO}^-$ , $\text{NH}_2\text{C}_3\text{PhO}^-$ , and $\text{NH}_2\text{C}_4\text{PhO}^-$ . ....	61
<b>Table 3.3.</b> Calculated total DFT+ $\Sigma$ correction ( $\Delta\Sigma$ ) from $\Delta 1$ and $\Delta 2$ . ....	61
<b>Table 3.4.</b> Lorentzian Fitting parameters from the NEGF transmission spectra as well as the DFT+ $\Sigma$ corrected HOMO resonance energy ( $\epsilon_\Sigma$ ). ....	73
<b>Table 3.5.</b> Morse Potential Fitting Parameters determined from Figure 3.8.A [well depth ( $D_e$ ), equilibrium bond length ( $R_e$ ), well width ( $a$ )]. ....	74
<b>Table 3.6</b> Morse Potential fitting parameters obtained from Figure 3.9. ....	76

## LIST OF FIGURES

<b>Figure 1.1</b> Single conductance traces of clean Au (orange) and an example molecule (red).....	3
<b>Figure 1.2.</b> (A) Image of the ultra-high vacuum 4K STMBJ Createc setup with the tip and substrate shown in the inset. (B) Image of the home-built ambient room temperature STMBJ setup with the tip and substrate shown in the inset. ....	4
<b>Figure 1.3.</b> (A) 1D conductance histograms of clean Au (orange) and the example molecule (red). (B) 2D conductance versus displacement histogram of the example molecule.....	6
<b>Figure 1.4.</b> (A) General molecular energy levels of a molecule before coupling to the continuous energy bands of Au electrodes related to electron transport. (B) Molecular junction energy levels, $\epsilon_i$ after coupling, given by $\Gamma$ , to the continuous energy bands of Au electrodes related to electron transport.....	7
<b>Figure 1.5.</b> Schematic representation of a single molecule junction in an electrical circuit with a voltage source and ammeter.....	8
<b>Figure 2.1.</b> (A) Structure of Group 8 metallocenes: ferrocene, ruthenocene, and osmocene. Also shown is a ball-and-stick model of ferrocene with a constant charge density contour color-coded to the electrostatic potential, indicating electron rich (red) and electron deficient (blue) regions. (B) STM image and height profile (inset) of sub-monolayer clusters of ferrocene deposited on Au(111) at 5 K. (C) Conductance trace measured in the presence of ferrocene on the Au(111) surface while pulling the tip out of contact with the surface and then pushing the tip back in to contact. The snapback distance is calculated from the difference in the displacement (grey) at the points when the tip breaks and reforms contact, as indicated by the dashed arrows. ....	16
<b>Figure 2.2</b> (A,C,E) 2D conductance vs displacement histograms of ferrocene pull traces after each filtering criteria. (B,D,F) 2D conductance vs displacement histograms of ferrocene push traces after each filtering criteria. (A,B) Entire dataset, (C,D) Traces	

lacking G0 plateaus filtered out, (E,F) Traces without molecular plateaus filtered out. ....	24
<b>Figure 2.3.</b> 2D conductance vs displacement for ferrocene (A) and ruthenocene (B) on Au(111) constructed from pull traces (tip withdrawal). 2D conductance vs Au-Au separation for ferrocene (C) and ruthenocene (D) on Au(111) constructed from push traces (tip approach). The solid black lines are exponential fits to the clean Au pull and push data in Figure 2.4 and indicate the average tunnelling current evolution on clean gold. For conductance values corresponding to the most probable values in the histograms (E), arrows indicate an extension beyond the Au separation for vacuum tunnelling by 2 Å in (A) and 5 Å in (C). 1D conductance histograms constructed with the push and pull traces separately for ferrocene (E) and ruthenocene (F). Traces that do not exhibit a molecular plateau are filtered out in (E) and (F) only..	26
<b>Figure 2.4.</b> 2D conductance vs displacement histograms of traces measured on clean Au without any metallocene present. Measurements were taken during while pulling out of contact (A) and pushing back into contact (B). ....	27
<b>Figure 2.5.</b> Snapback distribution determined from the set of traces measured in the presence of ferrocene that exhibit a molecular step signature or just tunneling through vacuum. The red fit is generated by fitting a sum of 5 Gaussian distribution functions. The numbers indicate the means of the normal distributions extracted from the fitting. ....	29
<b>Figure 2.6.</b> Correlation histograms of snapback and 1 G0 step length for both push and pull traces in the presence of ferrocene. (A, B) Data set including tunneling and single molecule signatures; (C, D) After filtering leaving only those traces with a single molecule signature.....	29
<b>Figure 2.7.</b> (A) Left: 1D conductance histogram of ferrocene push traces with snapback values in the range from 0 to 2 Å (gray), 2 to 5 Å (blue), 5 to 8 Å (black) and 8 to 12 Å (red). Main panel: 2D conductance vs inter-electrode distance histogram of ferrocene push traces with a snapback distance between 0 and 2 Å and (B) between 2 and 5 Å, (C) between 5 and 8 Å, and (D) between 8 and 12 Å. ....	31

**Figure 2.8.** (A) Left: 1D conductance histogram of clean Au push traces (orange) and the ferrocene push traces filtered by snapback distance ranges of 0 to 2 Å (gray) and 8 to 12 Å (red). Main panel: 2D conductance vs inter-electrode distance histogram of ferrocene push traces with a snapback distance between 0 and 2 Å. (B) As in (A), but with snapback distance between 8 and 12 Å. Heavy dashed lines (black) in (A) and (B) indicate the most probable conductance at each distance. Light dash lines mark the half-sigma range around the most probable conductance from the 1D histogram at left. (C) Five selected traces for each case (0 to 2 Å, grey; 8 to 12 Å, red). ..... 32

**Figure 2.9.** (A) Left: 1D conductance histogram of ruthenocene push traces with snapback values in the range from 0 to 2 Å (gray) and 8 to 12 Å (red). Main panel: 2D conductance vs inter-electrode distance histogram of ruthenocene push traces with a snapback distance between 0 and 2 Å and (B) between 8 and 12 Å. Heavy dashed line (black) indicates the most probable conductance at each distance. (C) Five selected traces for each case (0 to 2 Å, grey; 8 to 12 Å, red). ..... 33

**Figure 2.10.** (A) 2D conductance vs inter-electrode distance histogram of ferrocene pull traces with a snapback distance between 0 and 2 Å and (B) Main panel: between 8 and 12 Å. Right: 1D conductance histogram of ferrocene pull traces filtered by snapback distance ranges of 0 to 2 Å (gray) and 8 to 12 Å (red). Heavy dashed line (black) indicates the most probable conductance at each distance. (C) Five selected traces for each case (0 to 2 Å, grey; 8 to 12 Å, red). ..... 34

**Figure 2.11.** (A) 2D conductance vs inter-electrode distance histogram of ruthenocene pull traces with a snapback distance between 0 and 2 Å and (B) Main panel: between 8 and 12 Å. Right: 1D conductance histogram of ruthenocene pull traces filtered by snapback distance ranges of 0 to 2 Å (gray) and 8 to 12 Å (red). Heavy dashed line (black) indicates the most probable conductance at each distance. (C) Five selected traces for each case (0 to 2 Å, grey; 8 to 12 Å, red). ..... 34

**Figure 2.12.** Correlation histogram of snapback versus molecular step length of ferrocene push and pull traces..... 35

<b>Figure 2.13.</b> Normalized 1D Histograms of the molecular push step length of ferrocene. .....	36
<b>Figure 2.14.</b> Pull 2D conductance versus tip displacement histograms present room temperature STMBJ measurements of 1 mM ruthenocene (A) and osmocene (B) dissolved to 1 mM in 1,4-trichlorobenzene (TCB) with Au electrodes. Conductance traces were recorded pulling the Au tip out of contact with the Au sample. ....	37
<b>Figure 2.15.</b> Calculated frontier orbitals of gas phase ferrocene using FHI-aims with PBE functional and tight basis level. ....	39
<b>Figure 2.16.</b> Calculated relaxed geometries for ferrocene bound to gold electrodes in three distinct junction motifs at a tip separation corresponding to the potential energy minimum and the corresponding charge transfer induced by bonding of the ferrocene to the electrodes. (A, red) Ferrocene bound to sharp electrodes in a trans geometry. (B, blue) Ferrocene bound to sharp electrodes in a cis geometry. (C, green) Ferrocene bound to dull electrodes. Numbers report the net change in Mulliken population in each indicated slice of the junction structure. ....	41
<b>Figure 2.17.</b> Calculated transmission spectrum for each of the three junction structures illustrated in Figure 2.16: Sharp electrodes, trans (red); sharp electrodes, cis (blue); and dull electrodes (green). Bottom: Isosurface plots of molecular orbitals for the dominant eigenstates related to transmission. ....	43
<b>Figure 2.18.</b> (A) Binding energy calculated for ferrocene bound to sharp electrodes in trans configuration (red), to sharp electrodes in cis configuration (blue) and to dull electrodes (green) versus electrode separation as the electrodes are pushed together. (B) Calculated transmission versus electrode separation for each junction structure on the three trajectories shown in (A) and for a model of Au electrodes without ferrocene (neon) as a reference. The structure of the clean Au junction is shown in Figure 2.19. (C) Ball-and-stick figures showing junction structure for the numbered snapshots from the trajectories in (A). ....	45
<b>Figure 2.19.</b> Left (black): Calculated binding energy versus electrode separation for ferrocene bound to Au electrodes at the iron atom. Representative junction structures	

for the numbered points are shown below. Right: Calculated transmission for ferrocene bound in the junction versus electrode separation, corresponding to the trajectory shown at left. Also shown is the transmission calculated for Au electrodes without a molecule present as a function of electrode separation (neon).

Representative junction structures for the numbered points in the latter case are shown below. .... 47

**Figure 3.1.** (A) 1D conductance measurements of 4-hydroxybenzylamine in pH 7 (black) and pH 12 (blue) aqueous conditions, as well as 4-hydroxybenzylamine in trichlorobenzene (green). (B) 1D Conductance measurements of 4-hydroxybenzylamine (blue), 4-hydroxybenzyl alcohol (red), and 4-aminobenzyl alcohol (gray) in pH 12 aqueous conditions. .... 62

**Figure 3.2.** (A) Conductance histogram of 1 mM 1,4-benzenediamine in pH 7 H<sub>2</sub>O with a wax coated Au tip (black), 1.5 mM 4-aminobenzylamine in TCB (maroon) and NH<sub>2</sub>C<sub>1</sub>PhO<sup>-</sup> in pH 12 H<sub>2</sub>O (red). The structure of 4-aminobenzylamine is shown in the inset. (B, C) Conductance vs. displacement histogram of 4-aminobenzylamine and NH<sub>2</sub>C<sub>1</sub>PhO<sup>-</sup>. The dashed vertical line emphasizes the similar persistence of the two molecules with identical backbones but differing linkers..... 64

**Figure 3.3.** 1D conductance histograms and 2D conductance vs displacement histograms of NH<sub>2</sub>C<sub>1</sub>PhO<sup>-</sup> (A, E), NH<sub>2</sub>C<sub>2</sub>PhO<sup>-</sup> (B, F), NH<sub>2</sub>C<sub>3</sub>PhO<sup>-</sup> (C, G) and NH<sub>2</sub>C<sub>4</sub>PhO<sup>-</sup> (D, H). The black line in (E-H) is the gaussian fit of each vertical slice in the 2D histogram. The line cuts off after the amplitude of the Gaussian fit falls off by 85% below the maximum..... 66

**Figure 3.4.** Junction persistence lengths of NH<sub>2</sub>C<sub>1</sub>PhO<sup>-</sup> (red), NH<sub>2</sub>C<sub>2</sub>PhO<sup>-</sup> (blue), NH<sub>2</sub>C<sub>3</sub>PhO<sup>-</sup> (green), and NH<sub>2</sub>C<sub>4</sub>PhO<sup>-</sup> (gray). The inset shows the calculated junction formation fraction for each molecule..... 67

**Figure 3.5.** (A) Conductance histogram of NH<sub>2</sub>C<sub>1</sub>PhO<sup>-</sup> at different junction biases (B) Conductance histogram of NH<sub>2</sub>C<sub>2</sub>PhO<sup>-</sup> at different junction biases. (C) Conductance histogram of NH<sub>2</sub>C<sub>3</sub>PhO<sup>-</sup> at different junction biases. (D) Conductance histogram of NH<sub>2</sub>C<sub>4</sub>PhO<sup>-</sup> at different junction biases. .... 69

- Figure 3.6.** Conductance histograms of (A)  $\text{NH}_2\text{C}_1\text{PhO}^-$ , (B)  $\text{NH}_2\text{C}_2\text{PhO}^-$ , (C)  $\text{NH}_2\text{C}_3\text{PhO}^-$ , and (D)  $\text{NH}_2\text{C}_4\text{PhO}^-$  constructed from at least 5000 STMBJ traces collected in aqueous pH 12 conditions with a wax-coated tip at 500 mV bias. .... 70
- Figure 3.7.** (A) Comparison of the experimentally determined and DFT+ $\Sigma$  calculated conductance values of  $\text{NH}_2\text{C}_n\text{PhO}^-$  ( $n=1-4$ ) including the exponential fit for both and the corresponding parameters. (B) DFT+ $\Sigma$  adjusted single level HOMO resonance involved in transmission calculated at  $E-E_F=0$  eV (dashed black line) for  $\text{NH}_2\text{C}_n\text{PhO}^-$  ( $n=1-4$ ). (B, inset) Initial transmission spectra calculated using NEGF. (C-F) Visualization of the lowest energy geometries of  $\text{NH}_2\text{C}_n\text{PhO}^-$  ( $n=1-4$ ) bound to two  $\text{Au}_{34}$  electrodes that are used for transmission calculations. .... 71
- Figure 3.8** (A) Binding configuration of  $\text{Au}_{34}\text{-NH}_2\text{C}_2\text{PhO}^-$ . (B) Potential energy scan against length of the Au-X ( $X=\text{PhO}^-$ ,  $\text{PhOH}$ ,  $\text{CH}_2\text{S}^-$ ,  $\text{CH}_2\text{SH}$ ,  $\text{CH}_2\text{O}^-$ ,  $\text{CH}_2\text{OH}$ ) bond, with Au electrode modelled as  $\text{Au}_{34}$ . The Au apex atom is bound to either O or S in all cases. Data points were fit with Morse potential function, plotted as solid lines. 74
- Figure 3.9** Potential Energy scan of the Au-S bond with molecules terminated by -  $(\text{CH}_2)_2\text{SH}$ ,  $-(\text{CH}_2)_2\text{S}^-$ ,  $-\text{PhSH}$ ,  $-\text{PhS}^-$ , and  $-\text{PhSMe}$ . Data points were fit with a Morse Potential Fitting function. .... 75
- Figure 4.1** Resonance structures converting between the quinone, delocalized and diradical form of the family of benzofused quinoids ( $\text{BQ}_n$ ) where  $n=1-3$  with thioanisole linkers (ThA). .... 81
- Figure 4.2** (A) Single-molecule conductance histograms of  $\text{BQ}_n$  ( $n=1-3$ ) in BNP at low bias (-100 mV) in the top panel and high bias (-833 mV for  $\text{BQ}_{1-2}$  and -250 mV for  $\text{BQ}_3$ ) in the bottom panel. (B) Single-molecule 2D conductance vs displacement histograms of  $\text{BQ}_n$  ( $n=1-3$ ) at low bias in the top three panels and high bias in the bottom three panels. (C) Calculated conductance from gaussian fits to the peaks in Figure 4.2.A for both low bias (black) and high bias (gray) with exponential fits given by the dashed lines. .... 84
- Figure 4.3** (A) Current-Voltage histograms for  $\text{BQ}_n$  ( $n=1-3$ ) from thousands of IV curves taken while holding each molecule between two Au electrodes. Dotted lines

correspond to the linear grid lines and the white lines are calculated from the average of gaussian fits of vertical slices of each histogram IV histogram. (B) Fits of the conductance-voltage histograms derived from the current-voltage histograms for  $n=1,2,3$ . ..... 84

**Figure 4.4** (A) Description of the hopping terms ( $t_1, t_2, u_1, u_2, c_1, c_2$ ) describe by bond order alternation parameter ( $\delta$ ) used in the modified 1D SSH Hamiltonian. (B) Graphical representation of the hopping terms  $t_1, t_2, u_1, u_2$  and the calculated band structure for  $n=1,2,3$  molecules as a function of  $\delta$ . (C) Transmission spectra near  $E_f$  using NEGF from the 1D-SSH Hamiltonian for  $n=1,2,3$  molecules at  $\delta = -1, 0, 1$ . (D) Calculated transmission for  $n=1,2,3$  molecules as a function of  $\delta$ . The region of  $\delta$  where the molecules exhibit anti-ohmic conductance is shown in the shaded gray region. .... 86

## LIST OF ABBREVIATIONS

$\beta$	Conductance Decay Constant
$\beta_{expt}$	Experimental Conductance Decay Constant
$\beta_{DFT+\Sigma}$	Density Functional Theory + Sigma Conductance Decay Constant
$\gamma$	Lorentzian Width
$\Gamma$	Coupling Term
$\delta$	Diradical Parameter
$\Delta_1$	Gas Phase Correction to Density Functional Theory
$\Delta_2$	Image Charge Correction to Density Functional Theory
$\Delta E$	Total Density Functional Theory Plus Sigma Energy Correction
$\epsilon_0$	Resonance Peak Position
$\epsilon_\Sigma$	Density Functional Theory + Sigma Corrected Resonance Energy
$\epsilon_{HOMO}$	Energy of Highest Occupied Molecular Orbital
$\epsilon_i$	Energy of a Molecular Energy Level
$\epsilon_{LUMO}$	Energy of Lowest Unoccupied Molecular Orbital
$\zeta$	Zeta
$\sigma$	Conductivity
1D	One-Dimensional
2D	Two-Dimensional
3D	Three-Dimensional
4ABA	4-Aminobenzilamine
Å	Angstrom

$a$	Width of Potential
$A$	Cross-sectional Area
$A$	Lorentzian Amplitude
Ag	Silver
Au	Gold
BQ <sub>n</sub>	Benzofused Quinones
C	Carbon
$c_1, c_2$	Fixed Hopping Parameters
CH <sub>2</sub>	Methylene Group
CH <sub>2</sub> O <sup>-</sup>	Deprotonated Alcohol Group
CH <sub>2</sub> S <sup>-</sup>	Thiolate
CH <sub>2</sub> OH	Alcohol
CO <sub>2</sub> H	Carboxylic Acid
Cp	Cyclopentadiene
Cu	Copper
$D_e$	Well Depth
DFT	Density Functional Theory
DFT+ $\Sigma$	Density Functional Theory Plus Sigma
$e$	Elementary Charge
E	Energy
EA	Electron Affinity
eV	Electron Volt

$E_F$	Fermi Energy
$E_{\text{gap}}$	HOMO-LUMO Energy Gap
Fe	Iron
$G$	Conductance
$G_0$	Quantum Unit of Conductance
$I$	Current
IP	Ionization Potential
IV	Current-Voltage
$h$	Planck's Constant
HOMO	Highest Occupied Molecular Orbital
JACS	Journal of the American Chemical Society
K	Kelvin
KS-DFT	Kohn Sham Density Functional Theory
$k\Omega$	Kilohm
L	Length
LT	Low Temperature
LUMO	Lowest Unoccupied Molecular Orbital
m	Milli
mM	Millimole
mV	Millivolt
M	Metal Atom
$M\Omega$	Megaohm

MCBJ .....	Mechanically Controlled Break Junction
MO .....	Molecular Orbital
n.....	Number
N.....	Nitrogen
<i>N</i> .....	Number
NH <sub>2</sub> .....	Amine
nm .....	Nanometer
NaOH .....	Sodium Hydroxide
NEGF .....	Nonequilibrium Greens Function
NH <sub>2</sub> C <sub>1</sub> .....	Methylamine
NH <sub>2</sub> C <sub>1</sub> PhO <sup>-</sup> .....	Deprotonated 4-Hydroxybenzylamine
NH <sub>2</sub> C <sub>1</sub> PhOH .....	4-Hydroxybenzylamine
NH <sub>2</sub> C <sub>2</sub> PhO <sup>-</sup> .....	Deprotonated 4-(2-aminoethyl)phenol
NH <sub>2</sub> C <sub>2</sub> PhOH .....	4-(2-aminoethyl)phenol
NH <sub>2</sub> C <sub>3</sub> PhO <sup>-</sup> .....	Deprotonated 4-(3-aminopropyl)phenol
NH <sub>2</sub> C <sub>3</sub> PhOH .....	4-(3-aminopropyl)phenol
NH <sub>2</sub> C <sub>4</sub> PhO <sup>-</sup> .....	Deprotonated 4-(4-aminobutyl)phenol
NH <sub>2</sub> C <sub>4</sub> PhOH .....	4-(4-aminobutyl)phenol
Ni.....	Nickel
O.....	Oxygen
OH.....	Hydroxyl Group
Os .....	Osmium

PhO <sup>-</sup> .....	Phenolate
PhOH.....	Phenol
PMe <sub>2</sub> .....	Dimethylphosphine
Pt.....	Platinum
q <sub>i</sub> .....	Mulliken Charge
r.....	Bond Length
R.....	Resistance
R <sub>c</sub> .....	Contact Resistance
R <sub>e</sub> .....	Equilibrium Bond Length
RT.....	Room Temperature
Ru.....	Ruthenium
S.....	Siemen
S.....	Sulfur
SAM.....	Self-Assembled Monolayer
SH.....	Thiol
SMe.....	Thiomethyl
SSH.....	Su-Schrieffer-Heeger
STMBJ.....	Scanning Tunneling Microscope Break Junction
t <sub>1</sub> , t <sub>2</sub> .....	Variable Hopping Parameters
T <sub>i</sub> .....	Transmission Function of Single Channel
T.....	Total Transmission
TCB.....	1,2,4-Trichlorobenzene

ThA .....	Thioanisole
$u_1, u_2$ .....	Variable Hopping Parameters
UHV .....	Ultra-High-Vacuum
$V$ .....	Voltage
$V(r)$ .....	Morse Potential
$y$ .....	Diradical Character
$z_i$ .....	Position in Vertical Direction

## CHAPTER 1 Introduction

### 1.1 Motivation

With the realization in the middle of the 20<sup>th</sup> century that silicon-based electronics will likely reach their minimum size limits due to quantum effects, alternatives to silicon were proposed. Aviram & Ratner suggested in 1974 that a molecule could behave like a diode in a simple circuit, driving forward the possibility of molecular electronics as a viable alternative for silicon.<sup>1</sup> Within two decades the first set of experimental measurements of conductance of single molecules via the use of scanning tunneling microscopes was reported with additional techniques such as mechanical break junctions introduced soon after.<sup>2-6</sup> Since those first measurements, the number and types of molecules that have been incorporated into single molecule circuits has widely grown. Nevertheless, a real-world commercial single molecule based electronic has not been realized. On the other hand, the study of single molecule electronics has led to developments in the fields of chemistry, biology, and physics with gains in fundamental understanding of molecule-surface interactions and advances in technologies such as quantum information science, nanoscale sensing, and electron transport.

The multi-field impacts of single molecule conductance research is due to the enormous diversity of molecules. This includes variations of molecular core structure (backbone) or of terminal groups (linkers) which provide the ability to chemically bind/link to the external metal electrodes to form the molecular circuit. For example, recent studies have used single molecule conductance measurements to probe dative donor-acceptor

bonds to metal electrodes as well as van der Waals inter and intramolecular interactions which are not easily studied in macroscale systems.<sup>7-9</sup>

One of the largest drawbacks associated with single molecule electronics, is the low conductivity of molecular systems. This phenomenon derives from the quantum nature of electron transport at the sub-nanometer scale. A number of solutions have been proposed and reported to overcome this drawback such as incorporating a metal atom or diradicals into molecules.<sup>10-14</sup> Both approaches are hypothesized to provide additional conducting channels within the molecule. Transition metal atom-containing molecules have *d* and *f* electronic states leading to an increased density of electronic states and switching functionality due to distinct redox states which can be accessed through environmental control. Diradical containing molecules have additional nontrivial topological electronic states which have been shown to be high conducting in some circumstances.

To further the development of the field of molecular electronics, it is critical to understand how these degrees of freedom, such as new metal-molecular linking modalities and atypical molecular backbones with additional electronic or spin states, contribute to electron transport through single molecule circuits. This thesis presents three experimental and computational investigations of electron transport phenomena in metal-containing metallocenes molecules (Chapter 1), oxygen-linked molecular junctions (Chapter 2) and neutral organic diradicaloids (Chapter 3).

## 1.2 Scanning Tunneling Microscope Break Junction (STMBJ) Technique

The scanning tunneling microscope break junction (STMBJ) is a technique based on scanning tunneling microscopy that was modified to study the conductance of single molecules bound to electrodes. The STMBJ involves repeatedly smashing and pulling apart two metal electrodes (tip and substrate) which are connected to a voltage source. As the electrodes are pulled apart and a sub nanometer junction is formed in the presence of molecules, a molecule can bind to the tip and substrate electrodes, creating a single molecule circuit. The electrode position is maintained using a piezoelectric positioner with the voltage ( $V$ ) and current ( $I$ ) measured across the junction using a voltmeter and ammeter respectively. This allows for the conductance ( $G$ ), the inverse of resistance ( $R$ ):

$$G = \frac{I}{V}$$

to be determined as the electrode displacement is monitored to create an individual conductance trace, shown in **Figure 1.1**.

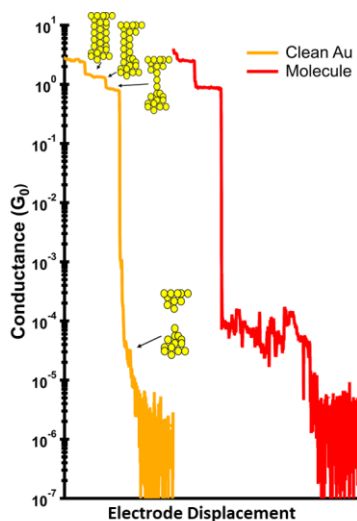


**Figure 1.1** Single conductance traces of clean Au (orange) and an example molecule (red).

The measurements in this thesis were done using two different types of STMBJ instruments: a commercial Createc STM, shown in **Figure 1.2.A** at ultra-high vacuum (UHV) and 4 K (LT) was used in Chapter 2; a home built STMBJ under ambient conditions and at room temperature (RT), shown in **Figure 1.2.B** was used in Chapters 2, 3, and 4.<sup>3,15,16</sup> A significant difference in the two instruments is in the choice of amplifier. While the UHV-LT-STMBJ uses a logarithmic amplifier to convert the picoamp current to a voltage, the RT-STMBJ uses a fixed gain linear current to voltage amplifier. Operationally, the technique for depositing molecules in the junction are different depending on the environment, with vapor-deposition onto pristine Au[111] substrate and solution-deposition onto a gold-coated metal AFM substrate used for the UHV-LT-STMBJ and RT-STMBJ respectively.

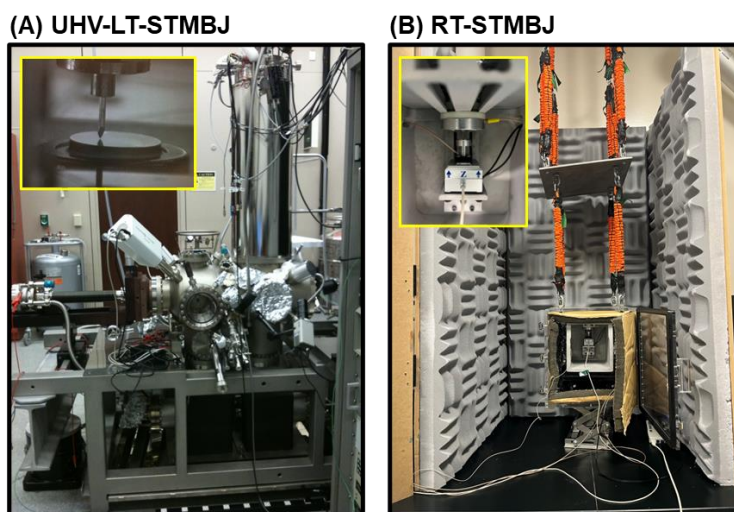


**Figure 1.2.** (A) Image of the ultra-high vacuum 4K STMBJ Createc setup with the tip and substrate shown in the inset. (B) Image of the home-built ambient room temperature STMBJ setup with the tip and substrate shown in the inset.

In both instruments, junction conductance is determined by collecting thousands of conductance traces as the electrodes are pulled apart and pushed back together. A typical individual conductance versus tip displacement trace without the presence of molecules using gold (Au) electrodes is shown in orange in **Figure 1.1**. The conductance is shown on a log scale in units  $G_0$ , the quantum unit of conductance ( $G_0$ ):

$$1 G_0 = \frac{2e^2}{h} \approx 77.5 \mu S$$

where  $e$  is the elementary charge,  $h$  is Planks constant and  $S$  is the SI unit of conductance, Siemens. As the substrate and tip stretch, the conductance decreases in quantized steps which correspond to the formation of a tip-substrate contacts with only a couple (integer) of Au atoms in the cross-section.<sup>17</sup> A single Au atom contact is characterized by a conductance of  $1 G_0$ .<sup>18</sup> Upon further electrode displacement, the tip and substrate break contact, and the conductance drops off exponentially with electrode displacement, due to quantum tunneling of electrons across the gap, until reaching the noise floor of the instrument below  $\sim 10^{-5} G_0$  as shown in **Figure 1.1**.

Thousands of these individual traces are then analyzed by binning the trace into a 1D conductance histogram, as shown in **Figure 1.3.A**, which allows us to identify molecular conductance features when compared to 1D conductance histograms from clean Au measurements. Additionally, 2D conductance versus displacement histograms are created to investigate and compare the lengths of the molecular conductance features as shown in **Figure 1.3.B**.

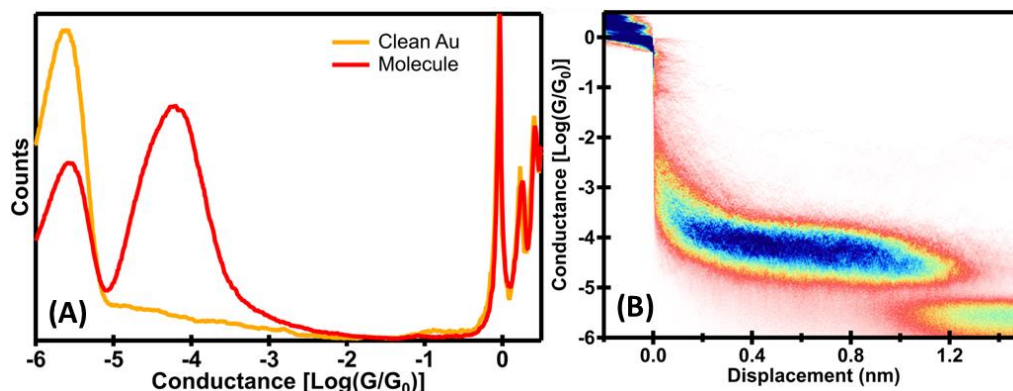


**Figure 1.3. (A) 1D conductance histograms of clean Au (orange) and the example molecule (red). (B) 2D conductance versus displacement histogram of the example molecule.**

### 1.3 Fundamentals of Electron Transport

Charge transport on the macroscopic scale, occurs by diffusive transport and behaves according to Ohms Law:

$$V = IR$$

where  $V$  is the voltage across a resistor,  $I$  is the current flowing across the resistor and  $R$  is the resistance of said resistor. The resistance is largely a product of the scattering of electrons off atoms as they are driven by the voltage through the resistor.<sup>19</sup> For a typical conductor or resistor with some given length ( $L$ ), cross-sectional area ( $A$ ), conductivity ( $\sigma$ ), the conductance is expected to obey the relation:

$$G = \frac{\sigma A}{L}$$

which predicts typical “Ohmic-conductance” where conductance decreases as the length of a conductor or resistor increases.

At the single molecule level, electron transport is no longer diffusive but instead ballistic governed by the Landauer formula:

$$G = G_0 \sum_i T_i(E)$$

which states that the total conductance is given by the sum over all energy dependent transmission channels ( $T_i(E)$ ) in a ballistic conductor, which in this case is either a single atom contact or molecule.<sup>20–22</sup> This transmission function,  $T_i$  describes the probability that an electron with energy  $E$  will transmit across the junction rather than be reflected back. For molecular junctions, these transmission channels derive from discrete energy states of the molecule, as shown in **Figure 1.4**. To first approximation, we only include the frontier orbitals  $\varepsilon_{HOMO}$  and  $\varepsilon_{LUMO}$ , corresponding to the Highest Occupied Molecular Orbital (HOMO) and the Lowest Unoccupied Molecular Orbital (LUMO). When a molecule binds to metal electrodes, the discrete molecular energy levels hybridize with the continuous band structure of the metal electrodes, resulting in broadening of the energy levels, given by  $\Gamma$ . In addition, energy renormalization near the metal surfaces causes a shift in the energy levels (from  $\varepsilon_{HOMO}$  or  $\varepsilon_{LUMO}$  to  $\varepsilon_i$ ) around the Fermi Energy ( $E_F$ ).<sup>23</sup>

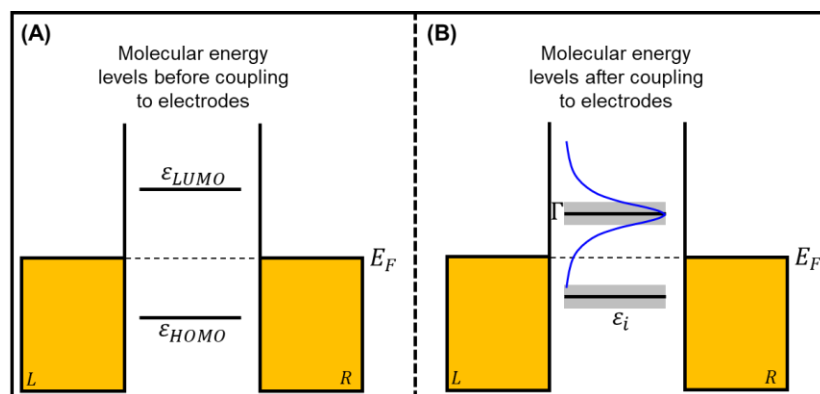


**Figure 1.4.** (A) General molecular energy levels of a molecule before coupling to the continuous energy bands of Au electrodes related to electron transport. (B) Molecular junction energy levels,  $\varepsilon_i$  after coupling, given by  $\Gamma$ , to the continuous energy bands of Au electrodes related to electron transport.

In most molecules, the energy levels are offset from the energy of the incident electrons  $E_F$ , leading to off-resonant transport. The transmission function,  $T(E)$  associated with a coupled single energy level can be approximated as a Lorentzian function, shown in **Figure 1.4.B**, and given by:

$$T(E) = \frac{(\Gamma^2/4)}{(E - \varepsilon_i)^2 + (\Gamma^2/4)^2}$$

#### 1.4 Anatomy of a Molecular Junction

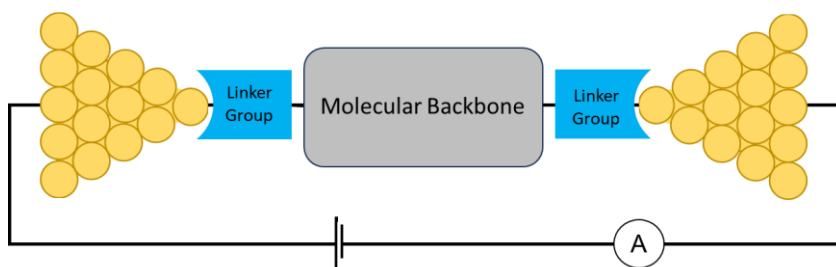


**Figure 1.5.** Schematic representation of a single molecule junction in an electrical circuit with a voltage source and ammeter.

A molecular junction is typically composed of a molecule characterized by a backbone structure and by functionalized linker groups that bind to metal electrodes on both sides, as diagrammed in **Figure 1.5**. Each of these components, (1) molecular backbone, (2) linker group, and the (3) atomic structure and composition of the electrodes all contribute to transport characteristics and conductance of the molecular junction.

### 1.4.1 Molecule Backbone

The molecular backbone is the core of the molecule which determines the nature of the molecular orbitals and the dependence of conductance on molecule length. Most often, the backbone is composed of a series of repeating units such as alkanes, alkenes, phenylene, thiophenes, silanes, or others.<sup>24-30</sup> One of the main differences between the various backbones is the electronic structure composed of either conjugated  $\pi$  orbitals (alkenes and phenylenes) or localized  $\sigma$  orbitals (alkanes, silanes). Since single molecule conductance occurs via quantum tunneling, the conductance is expected to decrease exponentially with length or each additional repeating unit, described by:

$$G \propto e^{-\beta N}, e^{-\beta L}$$

where  $\beta$  is the decay constant associated with an individual unit (or per unit length).<sup>31</sup> Prior measurements comparing  $\beta$  associated with alkane versus alkene chains, showed  $\beta_{alkane} > \beta_{alkene}$ .<sup>24,25</sup> This result indicates that the conjugated  $\pi$  orbitals characteristic of alkenes make for better transmission channels than the localized  $\sigma$  orbitals in alkanes. This is due to a smaller HOMO-LUMO gap in the conjugated molecules and a smaller energy offset between the molecular transmission channels and  $E_F$ . Similar considerations apply to cyclic conjugated molecular systems, composed of phenyl rings for example, though additional effects arising from quantum interference need to be considered as well.<sup>32-34</sup>

Prior work suggests that incorporating metal atoms or diradicals into the molecular backbone can mediate conductance decay associated with tunneling.<sup>10,12,14</sup> Unlike organic molecules composed of  $p$ -block elements C, O, N with 2s and 2p frontier orbitals, organometallics also incorporate transition metal atoms with additional frontier energy

levels coming from the d band ( $d_{xy}$ ,  $d_{xz}$ ,  $d_{yz}$ ,  $d_{z^2}$ , and  $d_{x^2-y^2}$ ). Molecular orbitals derived from the  $d$  states typically have a certain degree of degeneracy depending on the molecular symmetry and can have a range of effects on molecular conductance. Studies report both low and high conductance due to destructive and constructive interference in transition-metal containing systems, respectively.<sup>14,35,36</sup> Overall, the impact of metal atoms on electron transport in molecular junctions is not fully understood and requires further study to inform the design of highly conductive and robust molecular circuits.

The energy levels of diradical containing molecules are described through the framework of topological insulators, within the 1D Su-Schrieffer-Heeger (SSH) Model.<sup>37–39</sup> The energy levels associated with the frontier orbitals in diradical containing molecules are known as edge states. These edge states are topologically distinct from the typical conjugated molecular energy levels and are associated with a localized orbital at the Fermi energy  $E_F$  that can provide a viable transmission channel with high transmission near unity as long as the molecule is relatively short,  $\sim 1.5$  nm.<sup>39</sup> Electron transport through charged diradical containing molecules have been shown to behave “anti-ohmically” with conductance increasing as molecular length also increases. In prior studies, the limitation of these ionic diradicals is in the high localization of electronic edge state, which leads to the reversal of the anti-ohmic behavior to standard tunneling decay beyond a certain molecule length. Synthetic incorporation of repeating units of radicals with edge states has been shown to restore anti-ohmic behavior in molecules longer than  $\sim 1.5$  nm.<sup>40</sup> But the caustic solvent requirements and long-term instability of charged radical species, particularly in molecular junctions under an applied field, decrease the feasibility of this

approach. New and more stable molecular materials with topological edge states are required to realize high-conducting molecular junctions in accessible experimental conditions.

#### *1.4.2 Linker Group*

The linker group is fundamental for the formation of molecular junctions. Typical linker groups used in single molecule conductance studies are amines ( $\text{NH}_2$ ), thiomethyl (SMe), dimethylphosphine ( $\text{PMe}_2$ ), pyridine, and carboxylic acids ( $\text{CO}_2\text{H}$ ).<sup>14,16,28,30,41–49</sup> All of these linkers bind to undercoordinated atoms on the electrodes via a dative donor acceptor bond where a lone pair on the linker donates electron density to the metal.<sup>50</sup> It has been shown that donor-acceptor bonds select for a narrow range of metal-molecule binding configurations and result in consistent and reproducible molecular conductance signatures.<sup>44</sup> Functional groups such as thiols, bind to gold covalently and not specifically leading to broad conductance signatures<sup>2,3,51</sup>

Other studies report linker groups, such as pyridine, which exhibit two discrete binding geometries characterized by distinct conductance values that can be toggled mechanically.<sup>48</sup> Other linker functionality includes switched on an off through external control.<sup>52</sup> The choice of solvent has been shown to impact the ability for linker groups to bind to electrodes. For example, while amines readily bind to metal electrodes in organic solvents, they are protonated in neutral aqueous conditions, preventing the lone pair from donating to the electrodes.<sup>49</sup> On the other hand, linker groups such as imidazole and carboxylic acids have been shown to require deprotonation and only bind to metal

electrodes under basic aqueous conditions.<sup>15,41,53-55</sup> The variability in linker group properties warrants further study and presents an opportunity for engineering a diverse range of molecular circuits with switching or sensing capabilities.

### *1.4.3 Electrodes*

The structure of the electrode and its effect on junction conductance is largely overlooked in molecular junction studies. Most STMBJ measurements are done using metal electrodes (Au, Ag, Pt, Ni, and Cu).<sup>56-61</sup> A few reports include measurements on nonmetal electrodes such as graphene or carbon nanotubes.<sup>62-64</sup> The choice of metal is important for transport properties in part because it sets the value of  $E_F$  and determines the mismatch with frontier molecular orbitals (MOs).<sup>22</sup> Au is most often used in ambient conditions because it is inert in the presence of oxygen, while more reactive metals such as Cu are reserved for UHV. Soft metals such as Au and Ag are easily deformable and rupture easily in typical break junction pulling experiments, leading to undercoordinated atoms at the surface upon rupture.<sup>44,56,65</sup> However, the exact atomic structure of the electrode contact varies hugely over the thousands of junctions that are probed during an experiment. Variability in the electrode structure at the junction can impact the measured conductance by promoting distinct binding configurations.<sup>66,67</sup> This variability is difficult to control and is an obstacle for reproducible junction formation. The effect of metal-molecule interface on electron transport is an unsolved challenge in the field requiring further study. for molecular junctions which is why it's worth better understanding.

## 1.5 Thesis Outline

This thesis explores different distinct degrees of freedom that can lead to new functionality in single molecule junctions.

Chapter 2 focuses on single molecule conductance measurements as well as density functional theory calculations of metallocenes made using a LT-STMBJ. We study how the flat conjugated metallocenes bind preferentially to dull electrodes during junction pushing and the transport properties of the resulting junctions. We also study the role of the metal atom, M, in the molecule on the conductance and junction evolution, comparing junctions formed at 4K and at room temperature with ferrocene (M = Fe) and ruthenocene (M = Ru). This work was published in *JACS* in 2022.<sup>66</sup>

Chapter 3 reports reproducible single molecule conductance measurements using a new linker group, the phenol. We show that phenols only bind to metal electrodes to bridge the junction in basic aqueous conditions upon deprotonation. This switching behavior is not observed with more conventional linkers or with other hydroxyl groups such as alcohol. This work was published in *Nanoscale* in 2024.<sup>68</sup>

Chapter 4 reports the single molecule conductance measurements of a series of neutral diradical molecules that exhibit “anti-ohmic” conductance. We also develop a theoretical approach modifying the 1D Su-Schrieffer-Heeger model to accommodate fused, cyclic, conjugated carbon diradical systems, such as those probed here. We find that these types of molecular backbones are characterized by an intermediate diradical character which results in anti-ohmic conductance across a broad range of molecular lengths. Our work lays the foundation for development of highly conductive molecular wires realized

in simple and accessible experimental conditions. This work is currently in preparation for publication.

## **CHAPTER 2 Formation and evolution of metallocene single molecule circuits with direct gold- $\pi$ links**

### **2.1 Introduction**

Formation and characterization of single-molecule circuits with organometallic molecules enhance the scope of observable phenomena due to the incorporation of a transition-metal atom with new degrees of freedom.<sup>69–72</sup> Metallocenes are a class of such molecules where a metal ion (M) is sandwiched between two cyclopentadienyl rings (Cp). They are synthetically accessible, tunable, and stable in a variety of conditions, making them ideal model compounds for these applications. It has been theoretically predicted and later experimentally observed that molecular junctions and self-assembled monolayers (SAMs) containing ferrocene (M = Fe) bound to gold through organic linkers exhibit electronic functionality such as current rectification, conductivity enhancement, negative differential resistance, and spin filtration.<sup>14,36,40,73–82</sup> Other metallocenes (M = nickel, vanadium, cobalt) have also been studied using single-molecule methods such as scanning tunneling microscopy (STM) and break junction (BJ) approaches. Similar electron transport properties such as spin filtration, spin sensing, and near-unity conductance were found to depend on the orientation of the molecule in the junction.<sup>83–86</sup> The sensitivity of conductance phenomena to the physical structure of the nanoscale junction highlights the need for a clear understanding of how these molecules coordinate to the electrodes and for methods to control the metal–molecule interface structure.

Most organic molecules incorporated into single-molecule circuits to date closely approximate one-dimensional (1D) molecular wire rods with high aspect ratios and specific

linker motifs that bind to the electrodes and form the electrical contacts that close the circuit. We have previously demonstrated that junction evolution and conductance of organic molecular wires are sensitive to the atomic shape of the Au electrode and to the length of the molecule between the linking moieties.<sup>16,87,88</sup> In those junctions, the Au–molecule interface is a localized bond between an Au undercoordinated atom and a single donor atom on the organic molecule, usually nitrogen (N) or sulfur (S). During junction elongation, the molecular linker can slide along the electrode and change its attachment point on the Au structure, resulting in a flat conductance plateau during pulling over a distance range significantly longer than can be understood from just stretching the link bonds.

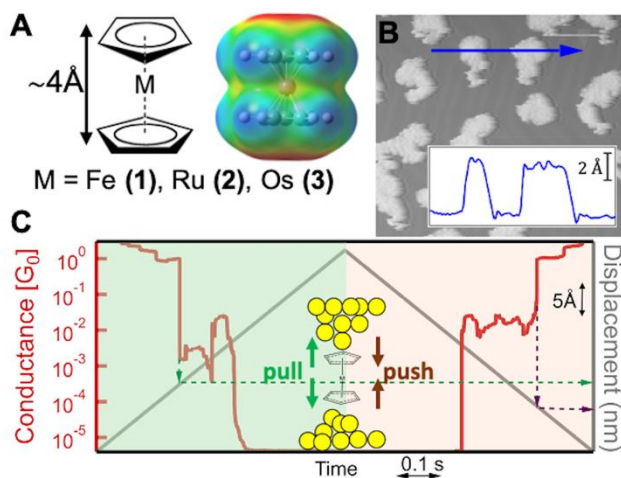


**Figure 2.1.** (A) Structure of Group 8 metallocenes: ferrocene, ruthenocene, and osmocene. Also shown is a ball-and-stick model of ferrocene with a constant charge density contour color-coded to the electrostatic potential, indicating electron rich (red) and electron deficient (blue) regions. (B) STM image and height profile (inset) of sub-monolayer clusters of ferrocene deposited on Au(111) at 5 K. (C) Conductance trace measured in the presence of ferrocene on the Au(111) surface while pulling the tip out of contact with the surface and then pushing the tip back in to contact. The snapback distance is calculated from the difference in the displacement (grey) at the points when the tip breaks and reforms contact, as indicated by the dashed arrows.

In contrast, organometallic compounds such as metallocenes (**Figure 2.1.A**) are bulkier with a “barrel” shape. Recently, both vanadocene ( $M = \text{vanadium}$ ) and nickelocene ( $M = \text{nickel}$ ), studied by STM, have been found to bind to metal electrodes either through the metal atom for vanadocene ( $\text{Au-M-Au}$ ) or through the Cp ring ( $\text{Au-Cp-M-Cp-Au}$ ) for nickelocene and vanadocene.<sup>85,86,89</sup> Metallocenes can also be extended with specific functional linker groups to direct the anchor point to gold, as demonstrated in some conductance studies.<sup>14,35,80,90</sup> Significantly, the metallocenes as such offer a distinctive feature, the delocalized electrons on the Cp rings that can coordinate to the electrodes. This aspect is emphasized by the electrostatic potential map of the molecule in **Figure 2.1.A**, which shows increased electron density on the flat Cp ends of the barrel and relatively decreased density along the sides of the molecule. We hypothesize that the formation and evolution of molecular junctions with barrel-shaped organometallic molecules, without functional linker groups, follow scenarios dictated by the electron-rich rings and the atomic-scale shape of the metal electrodes.

Specifically, we investigate the geometry, conductance, and evolution of molecular junctions made with group 8 metallocenes ( $M = \text{Fe}$  (**1**),  $\text{Ru}$  (**2**),  $\text{Os}$  (**3**)) on gold, as shown in **Figure 2.1.A**. These closed-shell, barrel-shaped molecules serve as a convenient test case for studying atomic arrangements and evolution of molecular junctions with organometallic molecules containing multihaptic ligands forming a three-dimensional (3D) structure rather than a 1D rod. Here, using scanning tunneling microscope break junction (STMBJ) conductance measurements in cryogenic and room-temperature (RT) conditions, we show that the metallocenes form reproducible metal–molecule–metal junctions despite

a lack of coordinated linker groups such as amines or thiols. At 5 K in vacuum, we measure and correlate the conductance evolution of each junction during pushing and pulling to the shape of the electrodes deduced from the measured electrode snapback distance. Supported by density functional theory (DFT)-based calculations of junction structure and conductance as a function of tip-sample distance, we find that the metallocenes bind primarily through the electron-rich cyclopentadiene (Cp) conjugated moieties on both sides of the molecule. In addition to bonding between undercoordinated Au atoms and specific C atoms of the Cp rings, we find a significant, additional role for binding of the barrel-shaped molecule to flatter binding areas exposed on blunt electrodes, promoted by van der Waals interactions.

## 2.3 Experimental Section

### *2.2.1 Molecular Deposition and Measurements in Cryogenic Conditions*

We perform single-molecule conductance measurements in ultrahigh vacuum using a commercial STM (Createc) with custom control hard and software GXSM at the Center for Functional Nanomaterials at Brookhaven National Laboratory.<sup>91,92</sup> The low-temperature STM break junction (LT-STMBJ) measurements are performed at 5 K and less than  $10^{-10}$  mbar. We repeatedly form and break quantum point contacts in the presence of a sub-monolayer of molecules. Metallocenes are deposited on atomically flat Au(111). A clean surface is achieved through two cycles of sputtering and annealing of a single-crystal gold sample according to standard methods.<sup>93</sup> To create the sub-monolayer, we expose the Au(111) surface at 5 K to a  $\sim 10^{-7}$  mbar vapor pressure of either ferrocene (**1**)

(CAS: 102-54-5) or ruthenocene (**2**) (CAS: 1287-13-4) molecules sublimed at room temperature in the preparation chamber of the STM under base pressure of  $10^{-10}$  mbar for 30 s. All gold tips are formed by mechanically cutting a 0.35 mm wire purchased from Fisher Scientific (99.99% metals basis for Au). STM images of both **1** (**Figure 2.1.B**) and **2** on Au(111) are taken at 0.7 V bias in Gain 9 to verify sub-monolayer formation. The height profile of molecular islands, shown in **Figure 2.1.B**, is measured to be 3.5 Å, which is in good agreement with the long axis of the molecule and consistent with a sub-monolayer of **1** adsorbed on the Au(111) surface.<sup>94</sup> We do not observe dissociation of **1** or **2** on the surface under the mild imaging conditions used here.<sup>94-96</sup>

Break junction measurements are performed both on the clean Au(111) sample prior to the vapor deposition and on the sample with a submonolayer coverage of metallocenes. For LT-STMBJ measurements, we record the current between a gold tip and substrate under the constant bias of 50 mV while displacing the tip relative to the substrate with sub-Angstrom resolution. To maximize the dynamic range of our measurement, we use a log amplifier (part #AD8304). Our break junction measurement consists of a repeated series of tip pulls and pushes. Using STM imaging, we first locate an unperturbed region of the surface with submonolayer coverage of molecules such as the one shown in **Figure 2.1.B**. Then, we position the tip a few nanometers above the surface by adjusting the set point current under 50 mV bias. We then initiate an automated protocol to collect 1000s of conductance vs displacement curves. The protocol establishes tip-sample contact by smashing the tip to a conductance  $> 1 G_0$  and then successively pulls and pushes the tip in and out of the sample by 4 nm as shown. We perform this pull-push motion 10 times in

the same location. Then, we displace the tip by several nanometers laterally to access a new area of the surface and repeat the pull–push protocol. Overall, this cycle is repeated hundreds of times to acquire the full data set.

A single conductance trace measured at 5 K as a function of tip displacement during junction pulling and pushing is shown in **Figure 2.1.C**. Both pull and push portions of the trace display plateaus at multiples of  $G_0$ , allowing us to identify the displacement coordinates along the trace (dashed arrows in **Figure 2.1.C**), where the gold quantum point contact breaks and reforms, respectively. To measure the snapback distance, we determine the distance between the electrodes immediately after rupture relative to when the electrodes come back into electrical contact during push and the conductance jumps to near  $G_0$ , as shown in **Figure 2.1.C**. At the latter point, the interelectrode distance is taken to be nominally 0 Å.<sup>43</sup> Physically, the centers of the apex atoms on the tip and sample are approximately separated by 2.5 Å, the diameter of Au atoms.<sup>87,97</sup> This analysis ignores jump-to-contact, which can occur during junction closing. While this affects our snapback distance measurements, the scale of the jump-to-contact effect (up to 1 Å) is significantly smaller than that of the snapback range observed here.<sup>98</sup>

### *2.2.2 Room Temperature Break Junction Measurements*

Room-temperature measurements are performed using previously described protocols.<sup>3,16,87</sup> Briefly, we repeatedly break and reform quantum point contacts of gold in a solution of molecules at standard temperature and pressure while recording the junction conductance and relative displacement. We form our gold tips by mechanically cutting 0.25 mm wire purchased from Fisher Scientific (#AA14730BY 99.999% metals basis). To

make Au samples, we polish metal specimen disks (Ted Pella #16219) and then coat the samples with 150 nm of gold (Fisher Scientific #AA14726BS, 99.999% metals basis) in a thermal evaporator. All measurements are done in a 1 mM or less solution in 1,2,4-trichlorobenzene (Sigma Aldrich #296104), a nonpolar solvent. Data collection and processing are automated with a home built Wavemetrics Igor Pro code. All measurements are done at 100 mV bias, with a relative tip-sample speed of  $\sim 20$  nm/s.

### *2.2.3 Data Analysis*

To analyze the formation, evolution, and conductance of metallocene junctions with statistical significance, we collect and bin push and pull traces in the corresponding push and pull logarithmically binned conductance histograms.<sup>3,16,87</sup> To create log-binned 1D conductance histograms, the logarithm of conductance values along hundreds (5 K) or thousands (room temperature) of conductance traces are binned into equally spaced bins. For 5 K measurements, traces without pronounced  $1 G_0$  plateaus or molecular features may be filtered out using well-established approaches that are described below.<sup>46,99</sup>

Recently, several data analytics techniques have been demonstrated for unsupervised clustering of experimental traces, distinguishing traces with molecular features as such as well as different classes of molecular junction structure.<sup>100–102</sup> In the present study, the identification of traces with molecular features did not prove to be ambiguous. The analysis of the molecular junction structure discussed below is based on physically measured descriptors.

To create two-dimensional (2D) conductance versus tip displacement histograms, we identify the point where Au junction ruptures (for pull) or reforms (for push) in each

trace as the zero of displacement. Individual traces are added up into histograms with linear bins along the displacement axis using this common distance origin. The conductance is binned logarithmically as for 1D histograms. The resulting 2D heat maps demonstrate the average evolution of junction conductance with changing tip-sample distance.

#### *2.2.4 Data Filtering Details and Analysis*

To determine statistically significant conductance values, we construct 1D conductance histograms as well as 2D conductance vs. displacement histograms from the data collected with and without filtering. The histograms shown in the paper use log binning of the conductance axis as discussed in the methods section of the manuscript. Before binning, the complete data set is initially separated into the corresponding push and pull traces. Any trace where tip-sample contact—a conductance of  $1.2 G_0$  or higher—is not achieved during push is filtered out. In addition, traces that do not break contact during pull by reaching a conductance of  $0.0001 G_0$  or lower, are discarded. The remaining ferrocene push and pull data, (labeled as All Data), is shown in the 2D conductance vs. displacement histograms in **Figures 2.2.A-B**. Two further filtering steps are also applied. First traces which did not exhibit clear  $G_0$  plateaus but instead display decaying tunneling in this conductance range are filtered out. Traces of this type exhibit a large number of points between  $0.5 G_0$  and  $0.1 G_0$  and they are distinct from traces with  $1 G_0$  plateau ruptures and molecular signatures. The remaining data is shown in **Figures 2.2.C-D**.

Second, traces which exhibit tunneling through vacuum only and no molecular signatures are filtered out for histograms in **Figure 2.2.E-F**. These traces exhibit a continuous decaying signature, characterized by a negative decay factor and a

monotonically declining conductance. We identify these traces by taking the derivative of a logarithm of the conductance and remove those traces which display only negative slope. Traces that show some  $\geq 0$  slope are identified as having a molecular signature. The results of all these filtering steps for ferrocene are demonstrated in **Figure 2.2** with the numbers of traces after each step of filtering are recorded in **Table 2.1**.

	Ferrocene		Ruthenocene	
	Pull Traces	Push Traces	Pull Traces	Push Traces
All Data (Used for <b>Figures 2.2.A-B</b> )	4833	4833	2472	2472
Remaining after poor tip filter (Used for <b>Figures 2.2.C-D</b> , <b>Figures 2.3.A-D</b> )	4238	3971	1803	1762
Remaining after tunneling filter (Used for <b>Figures 2.2.E-F</b> , <b>Figures 2.3.E-F</b> )	1264	1621	294	375

**Table 2.1** Number of remaining push and pull traces for both ferrocene and ruthenocene following each step in applying the filtering criteria.

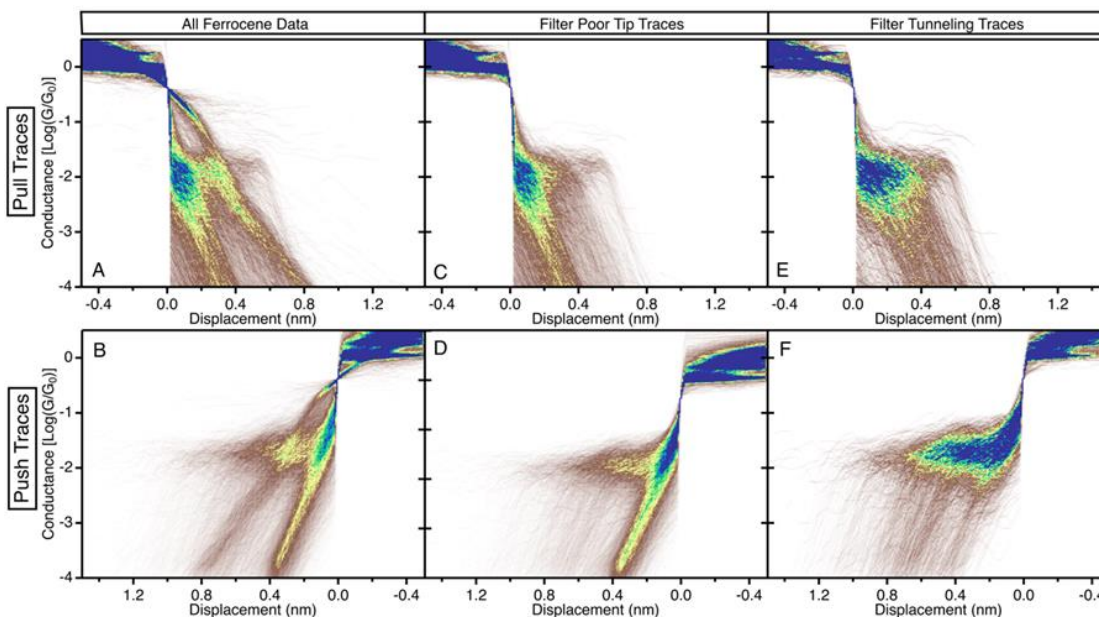


**Figure 2.2 (A,C,E) 2D conductance vs displacement histograms of ferrocene pull traces after each filtering criteria. (B,D,F) 2D conductance vs displacement histograms of ferrocene push traces after each filtering criteria. (A,B) Entire dataset, (C,D) Traces lacking G0 plateaus filtered out, (E,F) Traces without molecular plateaus filtered out.**

### *2.2.5 Density Functional Theory Calculations*

All DFT calculations are performed with the FHI-aims suite to obtain total energy, relaxed atomic-scale structure, and electronic structure. The nonequilibrium Green function method is used for calculating electron transmission through specific models for nanoscale junctions, as implemented in the AITRANSS package.<sup>103–107</sup> Various geometries of different gold electrodes with either **1** or **2** are relaxed using the PBE exchange–correlation functional and van der Waals corrections (Tkatchenko–Scheffler). The Kohn–Sham states are computed with an all-electron, atom-centered basis set. The FHI-aims suite supplies several options for optimized, numerical basis sets. Final results were computed using the “tight” level (similar to double  $\zeta$  plus polarization) for the atoms in the molecule and the “loose” level (double  $\zeta$ ) for the Au atoms in the electrodes.<sup>108,109</sup> The size of the gold structures used to model gold electrodes is converged with an increasing number of gold atoms. The final calculations are performed with at least 18 atoms per electrode, with adaptations to model different features of the tip structure (sharp versus blunt). In these calculations, the positions of the atoms in the molecule and two apex layers of gold atoms on each electrode are allowed to relax. Relaxation was considered complete when all force components/atoms were less than  $10^{-2}$  eV/Å. Charge-transfer calculations are performed and checked for convergence within FHI-aims using a Mulliken population analysis.

We simulate the pushing and pulling process in the break junction measurements by moving the electrodes in or out in steps of 0.15 Å or less and then relaxing the complete structure. For each step in the calculated trajectory, the interaction energy is the energy difference between the relaxed junction structure and the relaxed components (the two electrodes and the metallocene molecule). The transmission spectra across the molecular junction as a function of energy at zero bias for each step are calculated using AITRANSS.<sup>105,106</sup> We also compute the transmission for model junction structures without molecules present. To establish the reference electrode separation, we determine the electrode separation where the calculated transmission crosses  $1 G_0$  and designate that reference separation to be 0 Å, parallel to the convention used for the experimental push trajectories as described above. This approach allows us to compare the calculated distances to the experimentally measured Au–Au distances plotted in push 2D histograms.

## 2.3 Results and Discussion

### 2.3.1 Experimental Measurements

The data collected at 5 K for ferrocene and ruthenocene are summarized in **Figure 2.3**. For these histograms, all traces that displayed a pronounced  $1 G_0$  feature during pull were included. The exponentially decaying signature (black lines in **Figure 2.3.A–D**) in the histograms is due to tunneling background through vacuum and is also observed on clean gold traces (**Figure 2.4**).<sup>88</sup> In addition, we observe molecular conductance plateaus in the range from  $\sim 0.005 G_0$  to  $\sim 0.08 G_0$ , attributable to the formation of ferrocene and ruthenocene junctions during both the pull and push portions of the cycle. We determine

that  $\sim 30\%$  of pull and  $\sim 40\%$  of push traces measured in the presence of **1** and  $\sim 20\%$  of traces in the presence of **2** (Table 2.1, after filtering for poor tips) display molecular conductance features below  $1 G_0$ . For comparison, we note that ethylenediamine is a saturated molecular wire with a similar length to ferrocene of  $3.8 \text{ \AA}$  (N–N distance) and a conductance of  $\sim 0.005 G_0$ . On pull, this molecule is found to bridge  $\sim 25\%$  of junctions.<sup>16</sup>

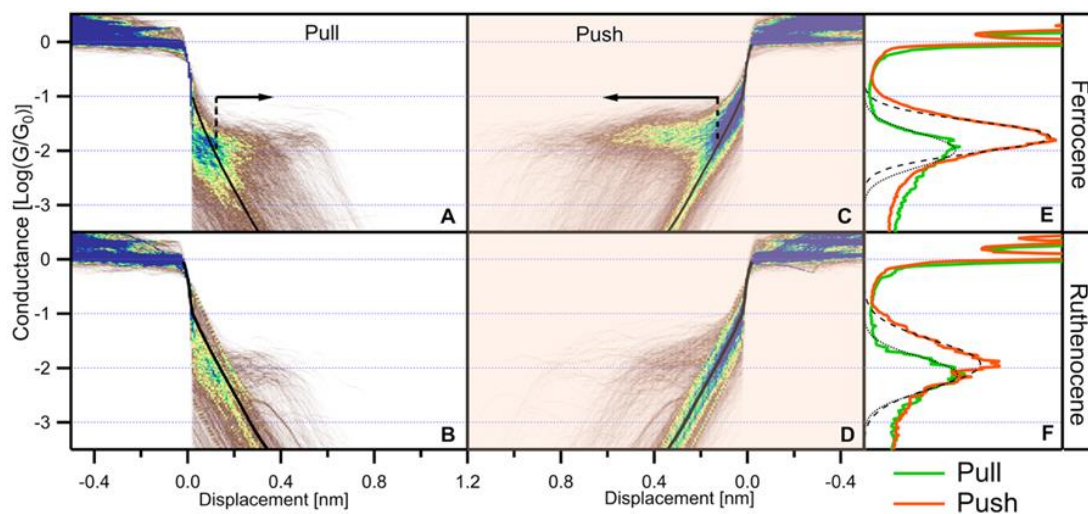


**Figure 2.3.** 2D conductance vs displacement for ferrocene (A) and ruthenocene (B) on Au(111) constructed from pull traces (tip withdrawal). 2D conductance vs Au-Au separation for ferrocene (C) and ruthenocene (D) on Au(111) constructed from push traces (tip approach). The solid black lines are exponential fits to the clean Au pull and push data in Figure 2.4 and indicate the average tunnelling current evolution on clean gold. For conductance values corresponding to the most probable values in the histograms (E), arrows indicate an extension beyond the Au separation for vacuum tunnelling by  $2 \text{ \AA}$  in (A) and  $5 \text{ \AA}$  in (C). 1D conductance histograms constructed with the push and pull traces separately for ferrocene (E) and ruthenocene (F). Traces that do not exhibit a molecular plateau are filtered out in (E) and (F) only.

We focus on metallocene junction properties by filtering out traces with no molecular signature. This eliminates the background counts in the histograms that arise from the exponentially decaying tunneling current in junctions that are not bridged by a

molecule. We then construct filtered 1D log-binned histograms. As shown in **Figure 2.3.E** and **Figure 2.3.F**, the resulting 1D histograms for both **1** and **2** display a more prominent molecular conductance peak for the push traces than for the pull traces. We determine the most probable conductance, histogram peak position, for the push (pull) signal: 0.017 (0.010)  $G_0$  and 0.011 (0.008)  $G_0$  for **1** and **2**, respectively. While the most probable conductance for **2** is 30–40% smaller than for **1**, these differences are smaller than the widths of the histograms and suggest that transport in group 8 metallocenes does not depend strongly on the metal center.

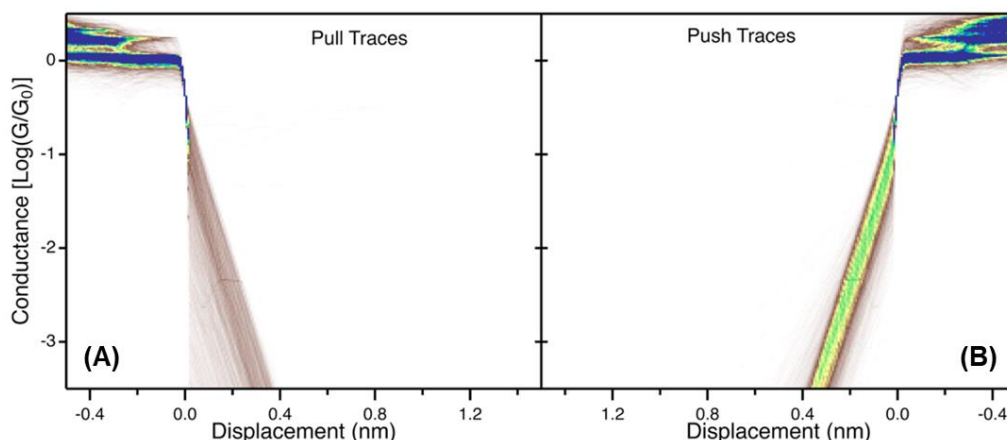


**Figure 2.4.** 2D conductance vs displacement histograms of traces measured on clean Au without any metallocene present. Measurements were taken during while pulling out of contact (A) and pushing back into contact (B).

To compare the persistence statistics of molecular plateaus, we turn back to the 2D histograms for **1** in **Figure 2.3.A** and **Figure 2.3.C**. At the pull conductance value of 0.010  $G_0$  (1D histogram peak), the average molecular plateau extends  $\sim 2$  Å (length of the arrow in **Figure 2.3.A**) past the tunneling background to where the Au–Au distance is  $\sim 4$

Å, comparable to the length of the molecule. In contrast, at the push conductance of  $0.017 G_0$  (1D histogram peak), molecular signatures extend at least 5 Å (length of the arrow in **Figure 2.3.C**) past tunneling. Furthermore, the distribution of traces includes junctions in which the molecular conductance signature remains for Au–Au separation of more than  $\sim 8$  Å. This characteristic of more extended molecular signatures during the push for metallocenes is distinct from previous results for junctions formed with organic molecular wires linked to Au by amine or thiomethyl groups in cryogenic conditions.<sup>88,89,110</sup>

To probe metallocene binding geometry and persistence in the junction, we examine the occurrence and step length of the ferrocene molecular junctions as a function of electrode snapback and  $1 G_0$  step length. For each pull–push trace, we use an automated protocol to calculate the snapback, as illustrated in **Figure 2.1.C**. The 5 K snapback distribution determined for the present data set is shown in **Figure 2.5** and agrees with previous measurements.<sup>16,88,97,111</sup> We observe that the snapback distribution is roughly quantized in multiples of gold atom lengths.<sup>112</sup> Furthermore, **Figure 2.6.A** and **Figure 2.6.C** illustrates that traces with longer snapbacks on average display longer  $1 G_0$  plateaus during the pull.<sup>111</sup> This pattern is consistent with the accepted view in the field that a gold atom chain containing an integer number of gold atoms can be pulled out during the stretch portion of the cycle. The chain eventually collapses leading to  $1 G_0$  rupture and a nanogap between the two electrodes.<sup>111–114</sup> The length of this snapback has been previously shown to correlate strongly with electrode geometry. Snapback values less than 2 Å are characteristic of Au electrodes that do not undergo significant plastic deformations and retain their atomically sharp structure after rupture.<sup>88,98</sup> Larger snapback values,

characteristically  $>8 \text{ \AA}$ , are associated with rearrangement of the apex atoms that collapse the electrodes into a flatter structure after  $1 G_0$  rupture.<sup>88,114</sup>

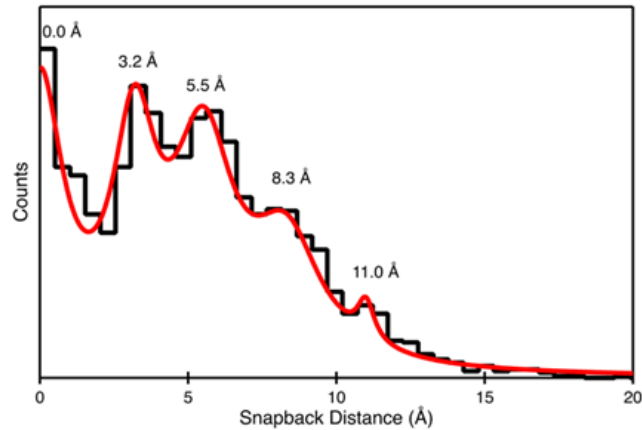


**Figure 2.5.** Snapback distribution determined from the set of traces measured in the presence of ferrocene that exhibit a molecular step signature or just tunneling through vacuum. The red fit is generated by fitting a sum of 5 Gaussian distribution functions. The numbers indicate the means of the normal distributions extracted from the fitting.

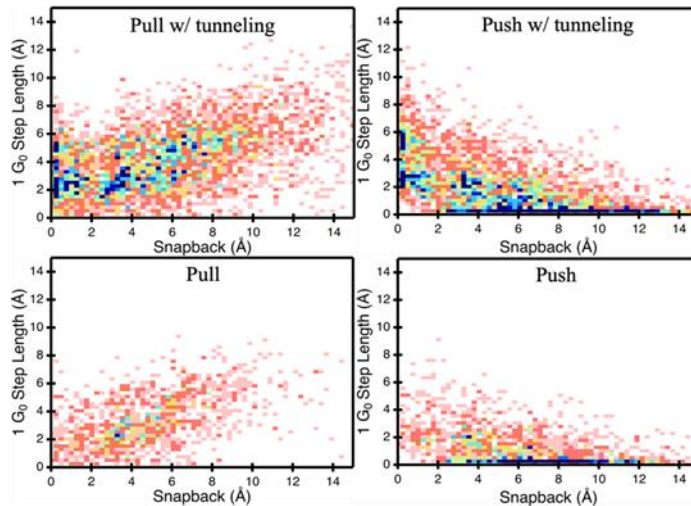


**Figure 2.6.** Correlation histograms of snapback and  $1 G_0$  step length for both push and pull traces in the presence of ferrocene. (A, B) Data set including tunneling and single molecule signatures; (C, D) After filtering leaving only those traces with a single molecule signature.

We sort traces that exhibit a molecular conductance signature based on the snapback determined for each pull–push trace. The data is sorted into bins based on snapback (**Table 2.2**). Then, 1D and 2D push and pull histograms are created for specified ranges of snapback distance. The full set of push data for **1** is shown in **Figure 2.7**. The 1D push histograms plotted in **Figure 2.7.A** (top axis) confirm that the longest snapback traces  $>8 \text{ \AA}$  corresponding to 3 or more Au gold atom diameters (red) have a significantly diminished  $1 G_0$  peak. These trends are also evident in correlation plots shown in **Figure 2.6.C** and **Figure 2.6.D** where traces with longer snapback are found to have shorter  $1 G_0$  plateaus. This result indicates that these traces form larger-area metallic contacts upon being pushed together.<sup>88,113</sup> In the discussion below, we will term these “blunt electrodes.” We note that blunt electrodes may also include electrodes whose pointed tips are displaced laterally relative to each other. In these cases, the shortest distance between the electrodes where the molecules might bind is still flanked by flat metal faces, and the “blunt” designation applies, albeit with a different orientation for the flat region. In contrast, the histogram constructed from traces with short snapback shorter than  $2 \text{ \AA}$  (gray), less than the diameter of a gold atom, displays a prominent  $1 G_0$  peak. This indicates a lack of atomic reorganization upon  $1 G_0$  rupture and much higher probability for protruding gold atoms on the electrodes, in this case, to be pushed together to form a single-atom contact. We will refer to these as “sharp electrodes.”

	<b>Ferrocene</b>		<b>Ruthenocene</b>	
	Pull Traces	Push Traces	Pull Traces	Push Traces
Snapback 0 to $2 \text{ \AA}$	211	187	93	88

Snapback 2 to 5 Å	511	488	119	105
Snapback 5 to 8 Å	374	505	56	110
Snapback 8 to 12 Å	148	351	26	63

**Table 2.2** Number of push and pull traces within each snapback bin range for both ferrocene and ruthenocene.

Focusing now on the 2D histograms of molecular signatures in **Figure 2.7**, we observe that the length of the molecular plateaus, on average, increases with increasing snapback. The shortest plateaus occur on the sharp electrodes in **Figure 2.7.A**; a mix of short and long molecular plateau lengths is observed in intermediate snapback regimes (**Figure 2.7.B** and **Figure 2.7.C**), which form the bulk of experimentally observed traces. Finally, the longest molecular plateaus are observed on the blunt plateaus (**Figure 2.7.D**). Here, we focus on the sharp and blunt extrema of the distribution, reproduced in **Figure 2.8** for **1** and **Figure 2.9** for **2**. This provides a clear contrast between physical scenarios.

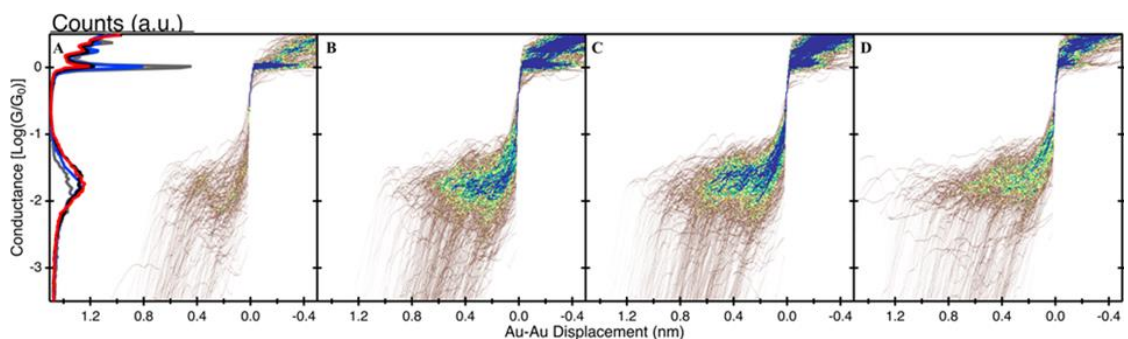


**Figure 2.7.** (A) Left: 1D conductance histogram of ferrocene push traces with snapback values in the range from 0 to 2 Å (gray), 2 to 5 Å (blue), 5 to 8 Å (black) and 8 to 12 Å (red). Main panel: 2D conductance vs inter-electrode distance histogram of ferrocene push traces with a snapback distance between 0 and 2 Å and (B) between 2 and 5 Å, (C) between 5 and 8 Å, and (D) between 8 and 12 Å.

We compare the evolution of junctions during pushing on the sharp (**Figure 2.8.A**) and blunt (**Figure 2.8.B**) electrodes. The most probable conductance, determined at each junction elongation, is indicated by the dashed black line in **Figure 2.8**. In both cases, starting from the noise floor, as the electrodes are pushed together, the conductance initially increases exponentially and then transitions to a plateau. At sufficiently small electrode separation, it rapidly increases toward  $1 G_0$ , with a profile characteristic of direct tunneling between the electrodes and reformation of Au–Au contact (**Figure 2.3.C** and **Figure 2.3.D**).

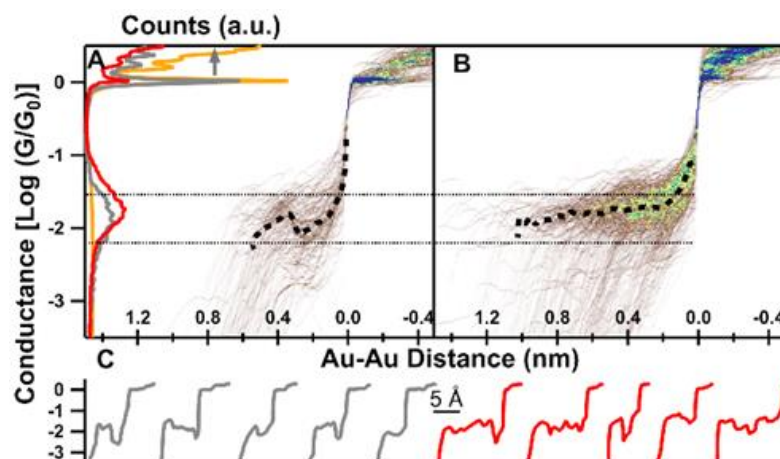


**Figure 2.8.** (A) Left: 1D conductance histogram of clean Au push traces (orange) and the ferrocene push traces filtered by snapback distance ranges of 0 to 2 Å (gray) and 8 to 12 Å (red). Main panel: 2D conductance vs inter-electrode distance histogram of ferrocene push traces with a snapback distance between 0 and 2 Å. (B) As in (A), but with snapback distance between 8 and 12 Å. Heavy dashed lines (black) in (A) and (B) indicate the most probable conductance at each distance. Light dash lines mark the half-sigma range around the most probable conductance from the 1D histogram at left. (C) Five selected traces for each case (0 to 2 Å, grey; 8 to 12 Å, red).

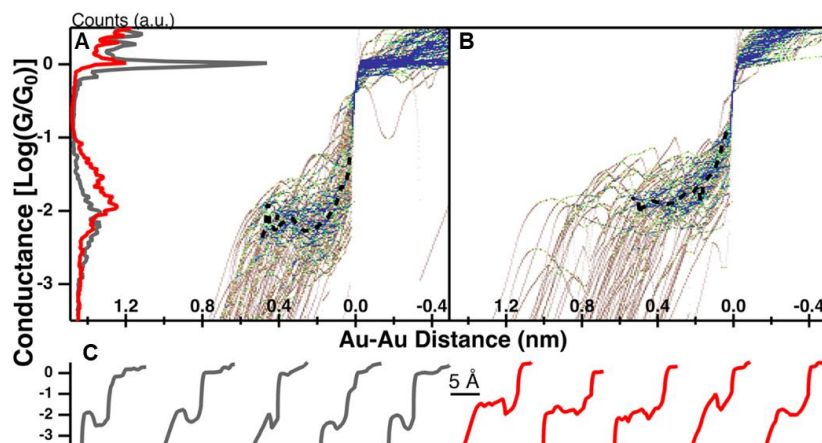


**Figure 2.9.** (A) Left: 1D conductance histogram of ruthenocene push traces with snapback values in the range from 0 to 2 Å (gray) and 8 to 12 Å (red). Main panel: 2D conductance vs inter-electrode distance histogram of ruthenocene push traces with a snapback distance between 0 and 2 Å and (B) between 8 and 12 Å. Heavy dashed line (black) indicates the most probable conductance at each distance. (C) Five selected traces for each case (0 to 2 Å, grey; 8 to 12 Å, red).

We observe specific differences depending on the snapback regime. As shown in **Figure 2.8.A**, upon pushing sharp electrodes together (small snapback), the molecular regime starts at Au–Au separation of  $\sim 5$  Å and persists within half of a standard deviation from the most likely conductance (gray dotted lines) for  $\sim 2$  Å. This is followed by a drop in conductance at  $\sim 3$  Å Au–Au separation. On the other hand, for blunt electrodes (large snapback), the molecular regime starts at an Au–Au separation of  $\sim 10$  Å and persists down to  $\sim 2$  Å, as shown in **Figure 2.8.B**. There is no dip seen in the most probable conductance profile. Remarkably, the most likely conductance we observe at Au–Au separation of  $\sim 2$  Å is unchanged from that at  $\sim 10$  Å. These distinct effects are evident in individual push traces shown in **Figure 2.8.C**. For sharp electrodes, the molecular plateau length is roughly  $\sim 2$  Å and a dip typically occurs before the rapid rise and Au–Au direct contact formation. For blunt electrodes, the plateau length is generally longer. While a dip occurs in some

traces, others display a smooth conductance transition from the molecular conductance plateau to the rapid rise toward  $1 G_0$ . Statistically, the latter evidently dominate.

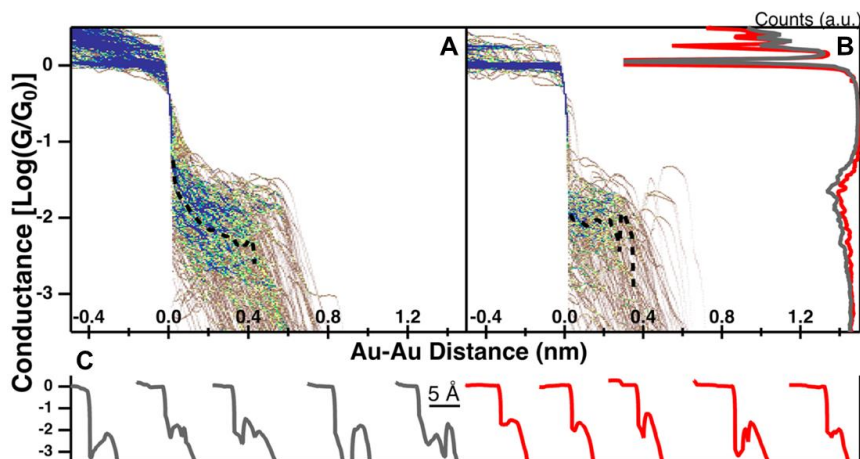


**Figure 2.10.** (A) 2D conductance vs inter-electrode distance histogram of ferrocene pull traces with a snapback distance between 0 and 2 Å and (B) Main panel: between 8 and 12 Å. Right: 1D conductance histogram of ferrocene pull traces filtered by snapback distance ranges of 0 to 2 Å (gray) and 8 to 12 Å (red). Heavy dashed line (black) indicates the most probable conductance at each distance. (C) Five selected traces for each case (0 to 2 Å, grey; 8 to 12 Å, red).

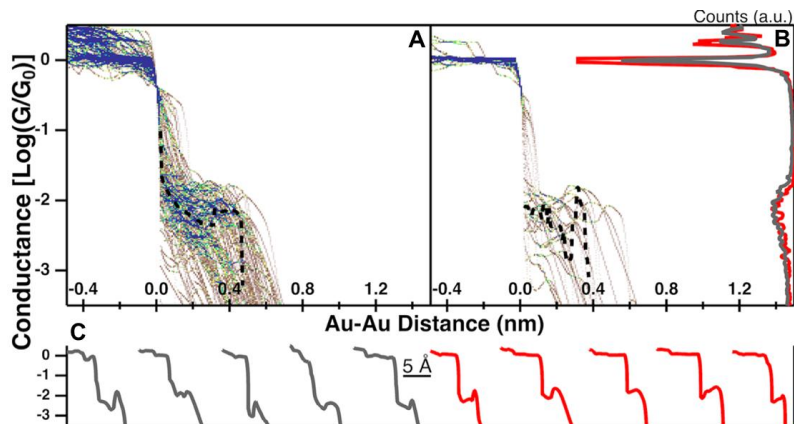


**Figure 2.11.** (A) 2D conductance vs inter-electrode distance histogram of ruthenocene pull traces with a snapback distance between 0 and 2 Å and (B) Main panel: between 8 and 12 Å. Right: 1D conductance histogram of ruthenocene pull traces filtered by snapback distance ranges of 0 to 2 Å (gray) and 8 to 12 Å (red). Heavy dashed line (black) indicates the most probable conductance at each distance. (C) Five selected traces for each case (0 to 2 Å, grey; 8 to 12 Å, red).

Conductance trajectories during pushing for **2** exhibit qualitatively similar behavior, as shown in **Figure 2.9**. Molecular plateaus are longer on blunt electrodes than on sharp ones, which display a relative dip in conductance prior to  $1 G_0$  contact formation. We note that the smaller data set collected with **2** results in greater statistical fluctuation in the average junction evolution behavior with **2**.

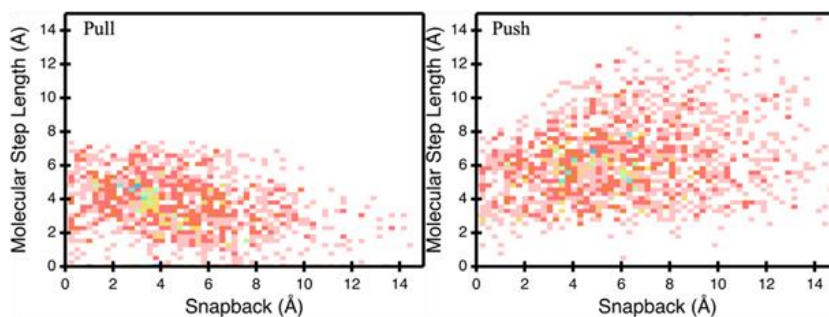


**Figure 2.12.** Correlation histogram of snapback versus molecular step length of ferrocene push and pull traces.

In comparison, the 2D pull histograms sorted by snapback for **1** (**Figure 2.10**) and **2** (**Figure 2.11**) show only a modest difference in persistence. The 2D histograms for the subsets of the data selected for small and large snapback are similar to each other as well as to 2D histogram for the full data set (**Figure 2.3.A**). This trend is also evident in **Figure 2.12** which shows that molecular plateau lengths for the pull portion remain on average constant with increasing snapback distance in contrast to push molecular plateaus, which tend to increase in length as snapback increases. **Figure 2.13** demonstrates that, although pull and push molecular plateaus tend to occur in the same trace due to the spatial clustering of molecules shown in **Figure 2.1.B**, the distribution of push molecular plateau lengths is statistically independent of the co-occurrence of a pull plateau in the same pull–

push cycle. This fact emphasizes the distinct evolution of ferrocene junctions during the opening and closing parts of the cycle with the same set of electrode tips.

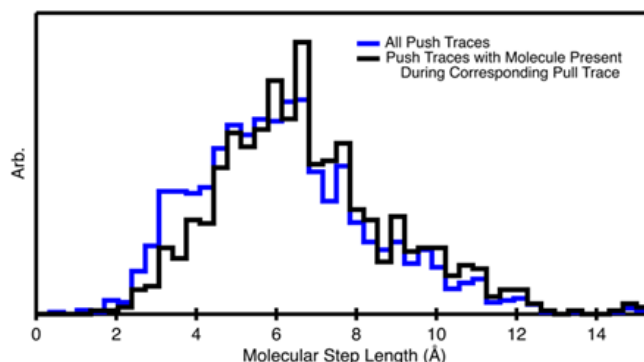


**Figure 2.13. Normalized 1D Histograms of the molecular push step length of ferrocene.**

A smaller fraction of traces with molecular plateaus on the pull compared to the push portion of the measurement prevents robust statistical analysis of small length differences in pull traces observed here. On the other hand, it is clear that overall, the pull histograms in **Figure 2.3.A** and **Figure 2.3.B** exhibit a similar molecular plateau persistence to the push histograms for sharp tips. This suggests similar bonding motifs for junction formation in these cases.

The  $\sim 2$  Å persistence length we observe for pull traces and for push traces with sharp electrodes corresponds roughly to the length of donor–acceptor bonds between gold and organic molecules reported in the literature.<sup>93,115</sup> Furthermore, the dip in the push traces suggests that the probability of junction rupture increases significantly when the Au–Au distance is shorter than  $\sim 3$  Å, comparable to the size of the molecule. The minority of traces with longer plateaus indicate more complex evolution of the junction structure. In

contrast, for push traces on dull electrodes, the average conductance is slightly higher, and the molecule can remain bound as the junction is compressed over  $\sim 8$  Å in length. Furthermore, that conductance is maintained, on average down to the Au–Au distance where direct interelectrode interactions become significant. The constant conductance plateaus that exceed the length of the molecule upon pushing on blunt electrodes suggest junction evolution trajectories where the molecular binding and electron transport is relatively insensitive to Au–Au distance. In fact, this phenomenon of constant molecular conductance over multiple Angstroms of compressing is reproduced on all but the most atomically sharp tips (snapback shorter than 2 Å) in our data set, as can be seen in **Figure 2.7.B-D**.

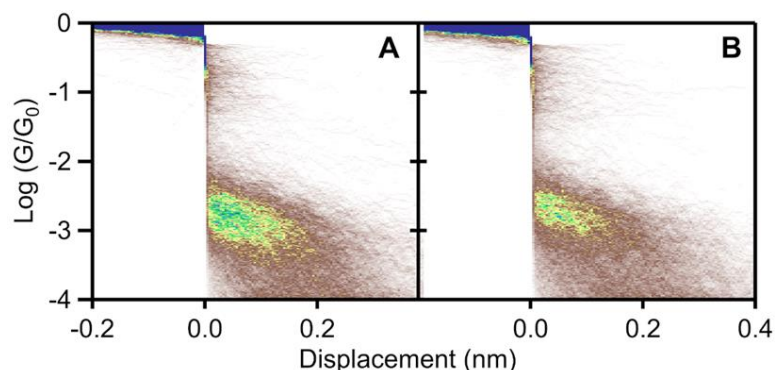


**Figure 2.14.** Pull 2D conductance versus tip displacement histograms present room temperature STMBJ measurements of 1 mM ruthenocene (A) and osmocene (B) dissolved to 1 mM in 1,4-trichlorobenzene (TCB) with Au electrodes. Conductance traces were recorded pulling the Au tip out of contact with the Au sample.

We perform room-temperature, pull conductance measurements on molecules **1–3** as described in the experimental section. Push measurements at RT conditions do not result in reproducible molecular signatures.<sup>87</sup> We also do not obtain a reliable pull conductance histogram of **1** at RT conditions. This result may be due to lower solubility of

this molecule in the nonpolar solvent used here compared to **2** and **3** or to its slightly shorter length, which may decrease its binding probability under RT junction formation conditions. 2D histograms of 4000 traces each of **2** and **3** measured in solution at room temperature during pull are shown in **Figure 2.14**. We observe similar conductance signatures for **3** compared to **2**, with average conductance values of  $0.0009 G_0$  and  $0.0008 G_0$ , respectively. This result reinforces the conclusion from cryogenic measurements above that the nature of the metal ion does not affect transport through group 8 metallocenes.

Comparing RT with cryogenic measurements, we observe a lower conductance for **2** at RT ( $0.0009 G_0$ ) compared to 5 K ( $0.008 G_0$ ). We note that the conductance peaks in 5 K and RT 1D histograms are both more than 1 order of magnitude wide, making the comparison of average conductance values less meaningful. The histograms for **2** measured at RT and 5 K do overlap, with significant counts falling between  $10^{-2}$  and  $10^{-3} G_0$ . The effect of temperature on average molecular junction conductance has been documented previously. Electrode geometries vary significantly with temperature.<sup>88</sup> Metal–molecule energy level alignment, dynamics of junction relaxation, and other details of junction formation and transport have been attributed to thermal effects. These considerations as well as solvation effects in RT measurements can result in complex dependence of transport on junction environment.<sup>88,110,116,117</sup>

### 2.3.2 DFT Calculations

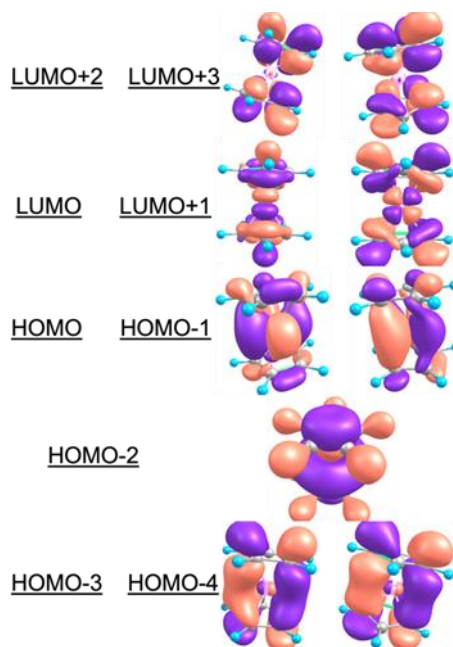


**Figure 2.15.** Calculated frontier orbitals of gas phase ferrocene using FHI-aims with PBE functional and tight basis level.

To further understand our results, we investigate the electronic properties of group 8 metallocenes and consider representative scenarios for junction formation, evolution, and the associated electronic transport. The qualitative features of the frontier electronic states of an isolated ferrocene molecule have long been understood from the interplay between the  $\pi$ -states on the Cp rings and the d-states on the central Fe.<sup>118–120</sup> Our DFT calculations in the minimum energy eclipsed conformation agree with previous results and allow us to visualize the trends in the frontier orbitals showing the combinations of the Fe 3d and the Cp  $\pi$  orbitals (**Figure 2.15**).<sup>121,122</sup> The highest occupied molecular orbital (HOMO) and HOMO–1 are degenerate with  $3d_{x^2-y^2}$  and  $3d_{xy}$  characters on Fe while the HOMO–2 exhibits  $3d_z^2$  character. The lowest unoccupied molecular orbital (LUMO) and LUMO+1, which are also degenerate, are identifiable from their  $3d_{xz}$  and  $3d_{yz}$  distributions on the Fe atom. Qualitatively, the occupied frontier orbitals have more weight on the central Fe,

while the empty orbitals have more weight on the Cp  $\pi$  orbitals. The calculated DFT orbital energies, ionization potential (IP), and electron affinity (EA) for **1** (**Table 2.3**) all suggest that the HOMO is closer to the Fermi energy of the electrodes. In comparison, for ruthenocene (**2**), the HOMO–LUMO gap and the IP are larger (**Table 2.3**), consistent with our observation of somewhat smaller conductance (**Figure 2.3**).

	Ferrocene	Ruthenocene
State	Energy (eV)	
IP	6.8	7.23
EA	-0.9	-1.2
LUMO+7	2.32	0.92
LUMO+6	1.33	0.81
LUMO+5	0.82	0.81
LUMO+4	0.82	0.31
LUMO+3	0.73	0.31
LUMO+2	0.73	0.11
LUMO+1	-1.35	-0.72
LUMO	-1.36	-0.72
HOMO	-4.34	-4.58
HOMO-1	-4.34	-4.78
HOMO-2	-4.47	-4.78
HOMO-3	-6.23	-5.93
HOMO-4	-6.23	-5.93
HOMO-5	-6.69	-7.19
HOMO-6	-6.69	-7.19
HOMO-7	-8.77	-8.8

**Table 2.3** The calculated [HOMO and LUMO from] ionization potential (IP) and electron affinity (EA) based on total energy differences. Frontier orbital energy values from the SCF calculations.

To investigate the possible binding configurations of metallocenes in Au junctions, we relax junction structures with **1** on both sharp (**Figure 2.16.A** and **Figure 2.16.B**) and blunt (**Figure 2.16.C**) electrode models. The blunt electrode model is asymmetrical with one electrode modeled by removing an apex atom and the other by a flat 4×5 Au atom slab.

A third scenario could involve two flat electrodes. However, the longest snapbacks we observe in the experiment are on the scale of 4 Au atom diameters (**Figure 2.5**), suggesting that the amount of reorganization during snapback would be unlikely to generate two flat electrodes. We find several binding geometries, as shown in **Figure 2.16**, with energies exceeding 0.5 eV per bond, where the Cp ring contacts metal electrodes. The structures shown correspond to local energy minima as a function of electrode separation, as we discuss further below. On sharp electrodes, we observe stable binding in both the trans (red) and the cis (blue) configurations as shown.

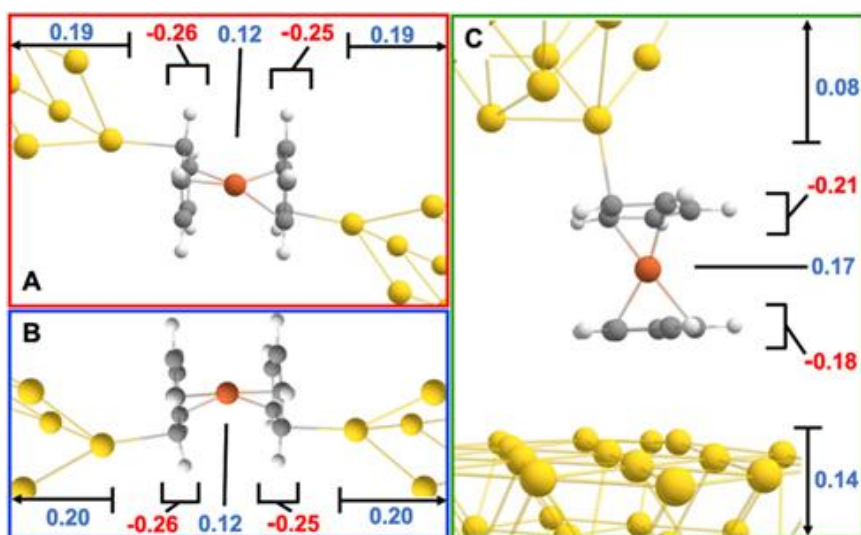


**Figure 2.16.** Calculated relaxed geometries for ferrocene bound to gold electrodes in three distinct junction motifs at a tip separation corresponding to the potential energy minimum and the corresponding charge transfer induced by bonding of the ferrocene to the electrodes. (A, red) Ferrocene bound to sharp electrodes in a trans geometry. (B, blue) Ferrocene bound to sharp electrodes in a cis geometry. (C, green) Ferrocene bound to dull electrodes. Numbers report the net change in Mulliken population in each indicated slice of the junction structure.

To understand the effect of the electrode binding on the electronic structure of the molecule, we first calculate the change in electron density that occurs upon binding using

a Mulliken population analysis. As seen in **Figure 2.16**, in all bridging configurations considered here, there is net electron transfer from ferrocene to the electrodes, consistent with expectations for the interaction between the electron-rich Cp rings and gold. In the sharp electrode case (red and blue), more net charge is transferred from the molecule to the gold. Self-consistently, the central Fe atom also gains electron density, with a greater transfer on blunt electrodes. For the sharp electrodes, this is indicative of donor–acceptor bonding to undercoordinated gold atoms on the electrodes. The Au–C bond distance found here of 2.35 Å is consistent with this interpretation. For the blunt electrode, the magnitude of charge transfer is similar to that found in studies of ferrocene and nickelocene on copper surfaces.<sup>123,124</sup> In agreement with that prior work, we find that van der Waals interactions play an important role in molecule-surface binding. We note that in the blunt case, the binding energy is higher than on sharp electrodes by 0.2 eV per electrode, while the Au–Cp distance is about 1 Å longer than Au–C donor–acceptor bond length.

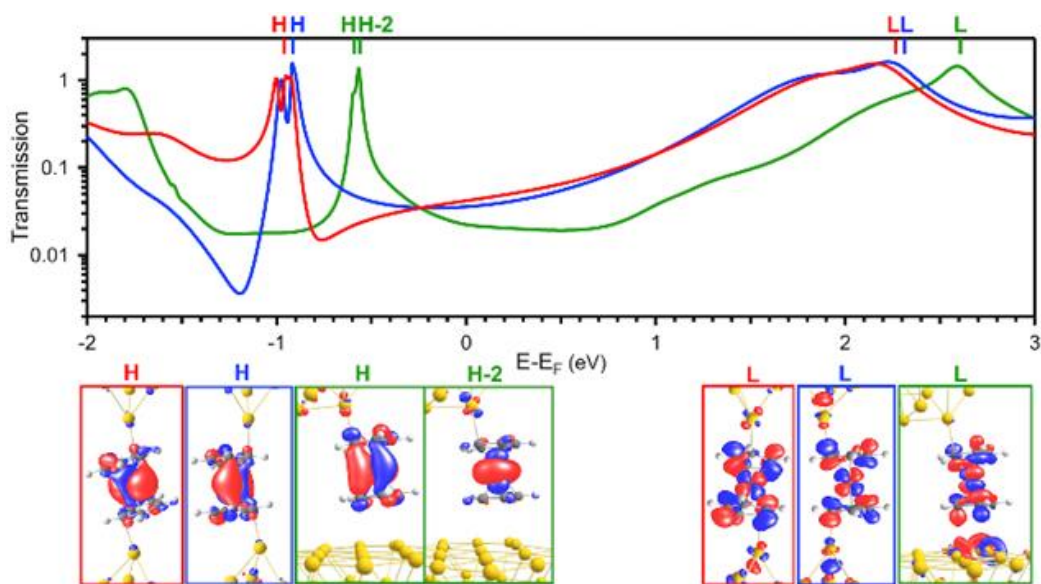


**Figure 2.17. Calculated transmission spectrum for each of the three junction structures illustrated in Figure 2.16: Sharp electrodes, trans (red); sharp electrodes, cis (blue); and dull electrodes (green). Bottom: Isosurface plots of molecular orbitals for the dominant eigenstates related to transmission.**

We calculate the electron transmission through these molecular junctions as a function of electron energy to understand how the binding geometry and the resulting charge transfer affect electron transport. Transmission results are shown in **Figure 2.17** for each of the junction structures illustrated in **Figure 2.16**. Overall, the resonances associated with occupied frontier molecular orbitals are closer to the Fermi energy than those that derive from the empty molecular orbitals. However, the latter exhibit stronger electronic coupling to the electronic states of the electrodes, as indicated by the larger width of the resonances. This is consistent with the relatively larger weight of the LUMO states on the Cp  $\pi$  orbitals of the isolated molecules (**Figure 2.15**). We also note that the greater charge transfer from the molecule to the gold in the sharp electrode case leads to a shift to lower energies of the molecular spectrum relative to the Fermi energy which will affect the dominant transport channel as we discuss below.

Isosurface plots of key frontier orbitals for molecules coupled self-consistently to the electrodes in each junction structure are shown in **Figure 2.17**. For the blunt electrodes, near degenerate molecular HOMO and HOMO-1 ( $3d_{x^2-y^2}$  and  $3d_{xy}$ ) and HOMO-2 ( $3d_z^2$ ) contribute to the primary resonances near -0.5 eV. In the junctions with sharp electrodes, the near degenerate orbitals with  $3d_{x^2-y^2}$  and  $3d_{xy}$  character contribute but not the  $3d_z^2$ . In all three junctions, the transmission spectra exhibit a characteristic asymmetric peak shape due to interference (Fano) effects among these channels. For the two junctions formed from

sharp tips, the trans versus cis bonding configuration in the junction leads to asymmetry with a broader shape to the lower versus the higher energy side of the transmission peak.

Focusing on the transmission near the Fermi energy, the transmission has a negative slope in the case of the blunt electrodes, indicating that occupied state-mediated tunneling dominates. The transmission for the junctions with sharp electrodes shows the opposite, corresponding to empty state-mediated tunneling. Several factors contribute to this contrasting behavior. First, for the sharp electrodes, the main resonances are shifted down in energy relative to the Fermi energy due to the increased charge transfer from the molecule to the gold as was described previously. This factor, combined with the stronger coupling of the empty molecular states to the electrode, results in LUMO-dominated transport. Second, for the blunt electrodes, the HOMO is higher in energy relative to  $E_F$  and the asymmetric line shape is broader on the high energy side. Taken together, this leads to HOMO-dominated tunneling for the blunt electrodes.

Despite these differences, in all three cases, the transmission at the Fermi energy is found to be in the relatively narrow range of  $2-4 \times 10^{-2} G_0$ , independent of whether it is HOMO or LUMO dominated. It is also similar to sharp and blunt electrodes. The calculated conductance magnitude is a bit larger than the measured range. This is fully consistent with the trend that is broadly observed when comparing DFT-based transmission to measured conductance for single-molecule junctions.<sup>67,125-128</sup> Corrections to the DFT-based approach or consideration of the additional screening due to neighboring molecules or a solvent can affect the level alignment and the magnitude of the calculated conductance.<sup>88,128,129</sup>

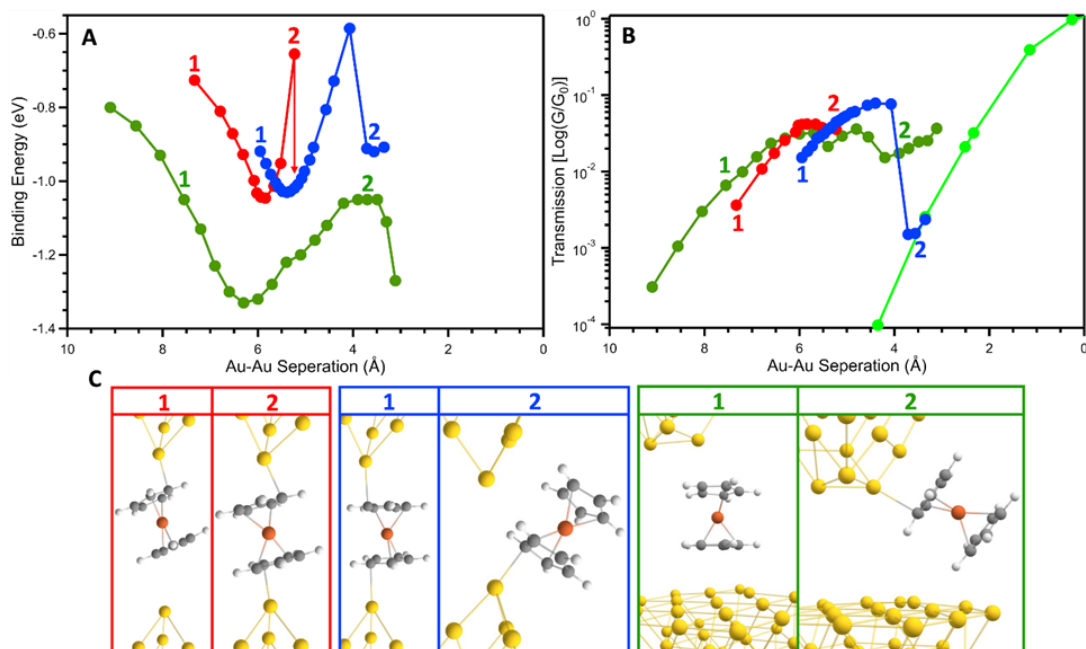


**Figure 2.18.** (A) Binding energy calculated for ferrocene bound to sharp electrodes in trans configuration (red), to sharp electrodes in cis configuration (blue) and to dull electrodes (green) versus electrode separation as the electrodes are pushed together. (B) Calculated transmission versus electrode separation for each junction structure on the three trajectories shown in (A) and for a model of Au electrodes without ferrocene (neon) as a reference. The structure of the clean Au junction is shown in Figure 2.19. (C) Ball-and-stick figures showing junction structure for the numbered snapshots from the trajectories in (A).

Next, we investigate whether this invariance of conductance to geometry can result in the extended junction plateaus measured experimentally upon pushing junctions together. We consider the evolution of the three sharp and blunt ferrocene junction structures in **Figure 2.16** as a function of Au–Au separation. We specifically model push trajectories, starting with a larger Au–Au separation (relative to the examples illustrated in **Figure 2.16**) and decreasing the separation in small steps as described in the Methods section. We plot the resulting binding energy and transmission at the Fermi energy in **Figure 2.18.A** and **Figure 2.18.B**, respectively. We note that the 0 Å on the Au–Au separation axis for our calculated geometries corresponds to the point when electrodes

come into electrical contact, just as in our experimental data in **Figure 2.3** and **Figure 2.8**, allowing us to compare the plots directly. Representative junction snapshots are shown in **Figure 2.18.C**.

We observe that the Cp-bound trans configuration (red) is most stable at  $\sim 5.5$  Å of tip–tip separation, where the molecule is fully elongated and tilted in the junction to bind to gold electrodes through the two most distant carbons on the opposite Cp rings. Upon compression, at about  $\sim 5.1$  Å of tip-sample distance as shown by the arrow, the electrode changes attachment site on the Cp ring of the molecule and switches to the cis configuration (blue). In this configuration, the most proximal carbons on opposite Cp rings are bound and the junction can accommodate the shrinking distance. As seen in **Figure 2.18.B**, this change in junction structure does not appreciably affect the calculated conductance. Finally, at  $\sim 4$  Å of displacement, the molecule breaks contact with the bottom electrode and rotates out of the junction. The concomitant decrease of conductance to the tunneling regime at this interelectrode distance, seen in **Figure 2.18.B**, indicates that the molecule no longer provides a tunneling pathway. Taken together, the combined trajectory calculated for sharp electrodes predicts a conductance plateau extending from  $\sim 6$  to  $\sim 4$  Å of Au–Au displacement, followed by a dip in conductance upon further compression.

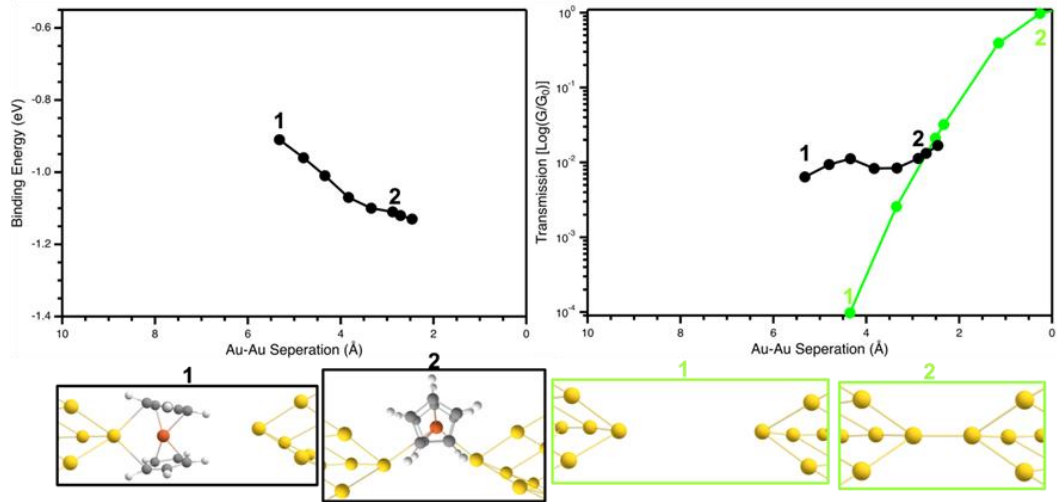


**Figure 2.19.** Left (black): Calculated binding energy versus electrode separation for ferrocene bound to Au electrodes at the iron atom. Representative junction structures for the numbered points are shown below. Right: Calculated transmission for ferrocene bound in the junction versus electrode separation, corresponding to the trajectory shown at left. Also shown is the transmission calculated for Au electrodes without a molecule present as a function of electrode separation (neon). Representative junction structures for the numbered points in the latter case are shown below.

Studies of junctions formed from vanadocene with Ag electrodes indicated an alternative junction geometry for sharp electrodes, with the electrode tip atoms directly coupled to the central metal atom of the metallocene. Our computed junction evolution with Au tip atoms directly coordinating the Fe atom is shown in **Figure 2.19**. The junction binding energy over the range of electrode separation from  $\sim 6$  to  $\sim 4$  Å is similar to that found for the Au–C bonded junctions. However, as the electrodes are further pushed together, the ferrocene is shifted aside leaving an increasing role for direct Au–Au interaction between the electrodes. The junction energy continues to drop as a consequence, and the conductance crosses over to a regime more characteristic of direct tunneling between the electrodes. As a result, no drop in conductance prior to  $1 G_0$  contact is observed for this geometry.

The computed trajectory for our model of ferrocene junction formation with blunt electrodes (green traces in **Figure 2.18**) shows a deeper and broader energy curve and correspondingly a wider plateau in the conductance as compared to the models for the sharp electrode. Nearly identical energy and conductance trajectories are found for the molecule initially bound to the flat surface or the blunt pyramid. Despite the longer equilibrium Au–Cp distance of these van der Waals-bound junctions mentioned earlier, the most stable binding energy on these blunt electrodes is  $\sim 20\%$  more than found for models of sharp electrodes, where the binding is consistent with donor–acceptor bonding. As the junction is further compressed, the metallocene progressively tilts and slides along the flat surface to accommodate the decreasing interelectrode separation. Surprisingly, even as the molecule tilts from the vertical by more than  $60^\circ$ , the binding energy decreases modestly, while the conductance remains virtually unchanged. Overall, the computed conductance rises from the tunneling regime, crossing over to form a molecular conductance plateau at  $\sim 7.5 \text{ \AA}$  that persists until the direct Au–Au tunneling path takes over as the electrodes reach  $\sim 3 \text{ \AA}$  separation. The computed tunneling conductance in the latter regime is larger than that computed for a single Au atom point contact. The upper tip in the blunt electrode structure naturally approaches a contact area with three Au atoms.

### 2.3.3 Discussion

Together, our experimental results, analysis, and computational results for model junction structures provide a clear picture for molecular junction formation and conductance characteristics with group 8 metallocenes. The experimental methodology in this study where the junction is tracked continuously through a full cycle of pull and push

enables correlation of conductance properties to electrode snapback on a trace-by-trace basis.<sup>88,98,111</sup> Clear differences in the 2D histograms emerge when they are sorted by measured snapback. Using prior correlation of electrode structure to snapback, we distinguish measured conductance characteristics for sharp and blunt electrode structures. Motivated by these results, the DFT-based calculations address these two scenarios through different model junction structures.

Overall, the group 8 metallocenes form single-molecule junctions directly, without the need for traditional linker groups. At 5 K, molecular plateaus with **1** and **2** reproducibly occur in 20–40% of junctions and result in reproducible conductance signatures both during the push and pull portions of the break junction experiment. Interestingly, the conductance measured on all electrode structures is similar, indicating that transport through metallocene molecular junctions formed without linkers is robust and insensitive to the tip structure. The DFT-based calculations corroborate this outlook, showing similar junction binding energies for both the sharp and blunt electrode scenarios. Furthermore, the computed trajectories show clear conductance plateaus with a similar magnitude of conductance.

However, the in-depth analysis of the 2D histograms sorted by snapback distance reveals a more nuanced picture with characteristics that do depend on electrode structure, particularly during the push portion of the conductance traces. On average, during all measured pull traces as well as push traces with sharp electrodes, junctions form, persist, and then rupture over a displacement distance of about 2 Å, roughly equal to an Au–C donor–acceptor bond. This suggests the formation of a specific junction motif with a

metal–molecule bond that distorts and then ruptures. A minority of junctions may involve more complex kinetic processes and changes in structure that contribute to longer plateaus. However, on pushing blunt electrodes together, we find that the metallocene molecules,  $\sim 3.5$  Å in length, can form and maintain a junction with approximately constant conductance for over  $\sim 8$  Å. Evidently, the molecule bound between blunt electrodes can rotate to accommodate a shortening distance without losing contact. At a sufficiently close approach, the direct tunneling channel between the electrodes, scaled by the area dictated by the blunt electrode structure, rises in importance, and ultimately dominates as the electrode separation tends to zero.

The DFT-based calculations show that the varied junction scenarios derive from the distinct modes of Cp–Au interaction driven by the electron-rich  $\pi$ -system on the rings and the barrel shape of the molecule. In the presence of undercoordinated Au sites, specific C–Au donor–acceptor bonds form. An alternative scenario in which Au tip atoms directly coordinate the central group A metal atom may also play a role, although it would likely be restricted to a few tip atom structures that can minimize steric hinderance with the rims of the Cp rings. When local flat, close-packed Au patches are available, nonspecific binding occurs, involving some electron transfer and further stabilized by stronger van der Waals interactions between the flat Cp ring and the surface.

These distinct bonding motifs translate to understanding the persistence of the molecular plateaus in the conductance trace of the barrel-shaped metallocenes. Typically, “rod”-shaped molecular wires bound through amines or thiols display robust conductance signatures with extended conductance plateaus during pulling because such molecules can

bind higher up on a protruding electrode and then change attachment point as the junction is stretched, while the conductance is relatively unchanged.<sup>88,110</sup> The flexible link motif adapts to bond to undercoordinated Au atoms along the side of the electrode. For the metallocenes, the electron-rich Cp rings can also form specific donor–acceptor C–Au bonds, but they are much less flexible. The repulsion from the electron-deficient sides of the barrel-shaped metallocenes (**Figure 2.1.A**) limits binding higher up on an Au electrode. Overall, this binding motif only supports relatively short ( $\sim 2$  Å) plateaus during pulling or pushing. On the other hand, the extended, flat electron-rich Cp surface promotes binding on blunt electrode patches. Our analysis and calculations demonstrate how this binding motif provides an alternative scenario for extended molecular conductance plateaus. In particular, a tilted molecule can still maintain overlap between the  $\pi$  electrons in the Cp ring and the Au electrode during pushing in this case.

More broadly, our results suggest that the 3D configuration and chemical details of the molecule, which can be synthetically manipulated, relative to the binding site have a defining effect on the selective formation and persistence of molecular junction. In particular, the metallocene substrate can be functionalized in many ways.<sup>14,35,78</sup> This offers the opportunity to manipulate the basic driving forces identified in our work to direct junction formation and tune conductance. Given the role of van der Waals interactions in the persistent conductance plateaus on flat electrodes, the  $\pi$  system of the molecular barrel could be expanded to further promote preferential blunt electrode binding by changing the Cp to an indenyl, for example.<sup>130</sup> Alternatively, functionalization of the Cp rings with electron-withdrawing or -donating substituents can tune the direction of charge transfer

between the molecule and the electrode, affecting bonding and transport properties. It can also influence the relative importance of HOMO versus LUMO-mediated conductance. Finally, such substituents could also further discourage molecular sliding along the Au electrode due to steric effects. These considerations have implications for future conductance measurements of organometallic and coordination complexes in single-molecule junctions.

## 2.4 Conclusion

Our results here provide an atomically resolved picture of the binding geometry, charge transfer processes and dynamics of the metallocenes-Au interface. Our break junction conductance measurement protocol combined with density functional theory calculations of junction electronics and geometries allows us to probe the evolution of metallocene-metal junctions which we find to be distinct from most molecules studied to date. The electron rich Cp ring on these organometallic “barrel” complexes, forms direct bonds to Au electrodes without the need for additional linker groups. We find that the formation and evolution of these junctions is dictated by the electron-rich ring binding sites and the atomic-scale shape of the metal electrodes. Specifically, the formation of specific C-Au donor-acceptor bonds does occur on sharp electrodes but is less energetically favorable than the van der Waals assisted binding of the Cp rings to blunt electrodes where more  $\pi$  overall can occur. Critically, we find that the barrel molecule shape is not compatible with the changing attachment point junction evolution scenario common for rod-like molecules. Instead, persistent plateaus occur on the blunt electrodes where the

bulky molecule can tilt and still maintain electric contact with the electrodes through van der Waals interactions.

The picture of junction formation for the barrel shaped molecules identified in this work is distinct from that for much more widely studied, rod shaped molecular wires. It offers interesting opportunities to further manipulate the formation of single molecule junctions that incorporate transition metal atom and tune the conductance characteristics

## **CHAPTER 3 Phenol is a pH-activated linker to gold: a single molecule conductance study**

### **3.1 Introduction**

A versatile toolbox of molecular components with diverse electronic transport and binding properties is a necessity for advancing the field of molecular electronics. Single molecule junction measurements such as scanning tunneling microscope break junctions (STM-BJ) and mechanically controlled break junctions (MCBJ) have been widely used to understand the ballistic transport of electrons through different families of molecules bound to atomic-scale electrodes, which are typically gold (Au), silver (Ag), or platinum (Pt).<sup>2,3,20,44,56,59,111,112,131</sup> Single molecules can bridge the source-drain gap by binding to the electrodes through chemical linker groups.<sup>50,132–134</sup> The nature of the metal electrode and hard-soft acid-base principles from synthetic chemistry determine the types of the metal-linker group interactions that enable successful single molecule junction formation.<sup>96</sup> For example, Au, which is the most used electrode material, is synthetically “soft” and thus forms strong covalent bonds with the “soft”, polarizable sulfur linker groups. Thiol-terminated molecules result in molecular junctions with disrupted Au-Au interactions due to intercalation of sulfur into electrode tips and disperse molecular conductance signatures which can make it challenging to quantify conductance trends.<sup>99</sup> Linker groups which are intermediate on the hard-soft continuum, such as imines and amines, bind to the gold electrode via a dative interaction.<sup>14,15,28,30,44–48,53,65,87,135–142</sup> Weaker than a covalent bond, this donor-acceptor interaction does not disrupt Au-Au interactions and is also selective for

specific binding geometries, limiting dispersion in single molecule conductance signatures on gold.<sup>44,50,134</sup> Notably, a certain number of donor linker groups such as the pyrrole nitrogen on imidazole require deprotonation in basic conditions to enable binding to the electrode.<sup>28,41,54,55,137</sup> In contrast to sulfur, oxygen is understood to be a “hard” donor atom. Although in the same chalcogen group as sulfur one row below it in the period table, oxygen is known as an unfavorable binding linker to the “soft” metals like Au and Pt.<sup>143</sup> Compared to sulfur, relatively few examples of oxygen-gold bonds are known in the inorganic synthetic literature, though recently phenols were found to bind to Au surfaces to form self-assembled monolayer with similar properties to thiols.<sup>144</sup> The few examples of oxygen-metal (O-M) binding in single molecule junction studies typically involve two binding moieties to form bidentate links such as with amides or with carboxyl groups to strengthen the metal-molecule interaction.<sup>41,49,55,145–147</sup> The specific monodentate O-M binding with a hydroxy group such as alcohol, phenol or ether group have not been observed in a molecular junction for conductance measurements on gold.

In this section we discover that O-Au binding can be realized in a single molecule junction through pH control which activates the oxygen on a phenol moiety for linking to gold electrodes. The resulting phenolate-bound molecules show robust single molecule conductance features. Alcohols which have a pKa higher than 14 cannot be deprotonated and activated to bind in aqueous conditions. We study the conductance of a series of phenol-terminated amino alkanes deprotonated at  $\text{pH} > 10$  and dried on gold samples prior to junction formation. We find that the conductance decays exponentially and molecular junction persistence grows linearly with molecule length as expected, confirming that

transport is occurring through the phenolate-bound molecular backbone. Our density functional theory (DFT) and Non-Equilibrium Greens Function (NEGF) calculations show that conductance through phenolate-terminated molecules is mediated by the highest occupied molecular orbital (HOMO). Using the DFT+ $\Sigma$  formalism, we accurately predict the tunneling transport characteristics of these systems. Overall, we find that O-Au binding is a promising linking strategy for environmentally controlled and robust molecular junctions. Importantly, our combined experimental and computational measurements on this novel linker system allow us to develop important insights into linker features conducive to effective anchoring on gold for molecular electronics and interface functionalization applications.

## 3.2 Methods

### *3.2.1 Break Junction Measurements*

Break junction measurements are performed using a homebuilt STMBJ previously described in detail.<sup>3,44,53</sup> The conductance measurements are made by bringing an Au tip repeatedly in and out of contact with an Au substrate at 16 nm/s, at a fixed bias below 500 mV. The pull-out portion of each cycle is recorded at 40 kHz and constitutes an individual conductance trace. Measurements in the presence of molecules are done either in solution or with molecules dried on the surface using the drop casting method as previously detailed and discussed below.<sup>15</sup> For measurements in aqueous solvent, the STM tip is coated in Apiezon wax.<sup>148</sup> Measurements made in aqueous solvent were compared to dry measurements to ensure no solvent or external factors such as ions are affecting the single

molecule conductance. Single molecule conductance measurements are also made at different junction biases, to determine if there is any bias dependence.

All aqueous solutions are prepared by initially dissolving sodium hydroxide (NaOH) in MilliQ water (purchased from Sigma Aldrich) until pH 12 is reached. The molecule of interest is then dissolved to a concentration of 0.1 mM in the pH 12 solution. The pH of the solution was then checked and adjusted back to 12 if necessary. A drop of the solution is deposited on gold coated (~150 nm, prepared by thermal evaporation) substrates and dried in a low temperature oven (less than 55 °C) for ~10 minutes, leaving the molecule deposited on the surface of the Au substrate. All molecules, solvents and Au wire are purchased from Sigma-Aldrich.

Conductance histograms are constructed out of a minimum of 5000 individual conductance traces. We bin the logarithm of all recorded traces without any data selection. 2D Histograms bin both conductance and displacement. The zero of displacement in each trace is defined as the Au-Au rupture point when the conductance drops below the metallic regime ( $1 G_0$ ) to the molecular scale.

The junction probability measurements are constructed using previously reported methods.<sup>16,87</sup> The persistence length distributions are generated from 2D histograms as described previously.<sup>87</sup> Briefly, we take vertical slices of the 2D histograms at each extension. The resulting slice conductance histogram is fit with a Gaussian fit and the peak maximum is plotted as a data point to the corresponding extension. By scanning through every extension and extracting the Gaussian fit amplitude, we achieve persistence length distributions. The persistence length quoted, corresponds to the point at which the 2D

feature amplitude decreases to 15% of the maximum and represents the ~longest extensions observed for a given molecule.

### 3.2.2 Theoretical Calculations

All DFT calculations are performed with FHI-aims to obtain relaxed atomic-scale structures as well as binding energies and configurations.<sup>103,104</sup> All calculations in FHI-aims are performed using the PBE exchange correlation functional with “tight” level basis set.<sup>108</sup> Each molecule was relaxed initially in a fully extended conformer and converged to the lowest energy state. The molecule was then bound between two Au<sub>34</sub> electrodes and the lowest energy junction distance was found by moving the electrodes in and out in steps of 0.05 Å. During each step, all atoms associated with the molecule as well as the four apex atoms for each electrode were allowed to relax, leaving the Au atoms in the final three rows frozen. This procedure identifies the most stable junction structures and equilibrium bond lengths. The interatomic potential for the O-Au bond is calculated by starting from the lowest energy geometry found above and stretching and compressing the O-Au distance in steps of 0.1 Å keeping all other relative atom positions frozen and running a single Self Consistent Field Energy calculation at each step. The total energy was scaled for each system to 0 eV at O-Au bond lengths of ~5.0 Å (broken bond) to remove long range effects in the charged systems. Each interatomic potential scan is fit to a Morse potential  $V(r)$ , given by the fitting function:

$$V(r) = D_e \left( e^{-2a(r-R_e)} - 2e^{-a(r-R_e)} \right)$$

where  $r$  is the O-Au bond length at each step in the scan,  $D_e$  is the well depth,  $a$  is the width of the potential and  $R_e$  is the equilibrium bond length.<sup>149,150</sup> Transmission of the metal-molecule-metal junction is calculated using a combination of NEGF as implemented in AITRANSS with adjustments based on DFT+ $\Sigma$  as described below.<sup>23,67,105–107,151–153</sup>

Since all transmission spectra calculated here using NEGF overestimated the conductance by more than an order of magnitude due to the presence of a HOMO resonance near the Fermi energy ( $E_F$ ). DFT+ $\Sigma$  is implemented to shift the resonance away from  $E_F$  by accounting for self-interaction energy errors and image charge effects. The DFT+ $\Sigma$  adjusted transmission at  $E-E_F=0$  eV is calculated and reported from the single energy level approximation.

The total DFT+ $\Sigma$  correction ( $\Delta\Sigma$ ) comes from the addition of a gas-phase correction ( $\Delta_1$ ) and image charge correction ( $\Delta_2$ ).

$$\Delta\Sigma = \Delta_1 + \Delta_2$$

The gas-phase correction term adjusts the calculated HOMO energy eigenvalue of the gas-phase molecule based on either experimentally measured values or on calculations using more accurate methods. The image charge correction comes from adjustments of energy levels based on the interaction of a charge distribution with a conducting surface (analogous to an image charge effect). A description of the methods used to calculate both terms is given below.

To calculate  $\Delta_1$  we determine the HOMO energy level of the gas phase deprotonated molecules by an Ionization Potential calculation,

$$E_{HOMO} = -IP = E_{N-1} - E_N$$

where  $E_{N-1}$  is the total energy of the gas phase molecule with one less electron (N-1), and  $E_N$  is the total energy of the gas phase molecule. In our case, the gas phase molecule is an anion, and the ionized gas phase molecule is neutral. All geometry relaxation and energy calculations are performed using GAUSSIAN 16 and the PBE exchange-correlation functional.<sup>108,154</sup> Since the molecules are negatively charged, all calculations were done with the Karlsruhe Def2 basis set including diffuse corrections.<sup>155,156</sup> The calculated  $E_{HOMO}$  for all molecules is checked for basis-set convergence using Def2-SVPD, Def2-TZVPD, and Def2-QZVPD, with all final values reported with the Def2-QZVPD basis set.  $\Delta_1$  was then able to be determined from the difference between  $E_{HOMO}$  and the HOMO energy eigenvalue ( $\epsilon_{HOMO}$ ) of the gas phase molecules from FHI-aims (used for transport calculations). The values of  $E_{HOMO}$ ,  $\epsilon_{HOMO}$ , and  $\Delta_1$  are shown in **Table 3.1**.

Molecule	$E_{HOMO}$ (eV)	$\epsilon_{HOMO}$ (eV)	$\Delta_1$ (eV)
NH <sub>2</sub> C <sub>1</sub> PhO <sup>-</sup>	-2.27	0.19	-2.46
NH <sub>2</sub> C <sub>2</sub> PhO <sup>-</sup>	-2.17	0.29	-2.47
NH <sub>2</sub> C <sub>3</sub> PhO <sup>-</sup>	-2.16	0.30	-2.46
NH <sub>2</sub> C <sub>4</sub> PhO <sup>-</sup>	-2.17	0.30	-2.46

**Table 3.1.** Calculated gas phase correction,  $\Delta_1$ , used for DFT+ $\Sigma$  for NH<sub>2</sub>C<sub>1</sub>PhO<sup>-</sup>, NH<sub>2</sub>C<sub>2</sub>PhO<sup>-</sup>, NH<sub>2</sub>C<sub>3</sub>PhO<sup>-</sup>, and NH<sub>2</sub>C<sub>4</sub>PhO<sup>-</sup>. The calculated HOMO energy levels from Ionization Potential calculations ( $E_{HOMO}$ ) and the HOMO energy eigenvalue from KS-DFT ( $\epsilon_{HOMO}$ ) are also shown.

The image charge correction,  $\Delta_2$ , is calculated from the relaxed molecular junction geometries. Since the molecules in the junction are anions, leading to neutral molecules when ionized, the typical practice of using a point charge in the center of the molecule to calculate the image charge offset was not applicable. Instead, the charge distribution of the

neutral molecule was treated as a partial point charge on each atom ( $q_i$ ), determined by a Mulliken charge calculation on the gas-phase neutral molecule in GAUSSIAN using PBE and Def2-SVP. The equation for  $\Delta_2$  is given by

$$\Delta_2 = \sum_i^M \frac{|q_i|^2}{4(z_i - z_{top})} + \sum_i^M \frac{|q_i|^2}{4(z_i - z_{bottom})}$$

where  $i$  is summed over all the atoms, and  $z_i - z_{top}$  ( $z_i - z_{bottom}$ ) is the distance from the atom to 1.75 Å above the plane of three Au atoms behind the apex Au atom on the top (bottom) electrode.<sup>23,153,157</sup> The calculated values of  $\Delta_2$  for the molecules studied are shown in **Table 3.2**.

Molecule	$\Delta_2$ (eV)
NH <sub>2</sub> C <sub>1</sub> PhO <sup>-</sup>	1.1
NH <sub>2</sub> C <sub>2</sub> PhO <sup>-</sup>	1.14
NH <sub>2</sub> C <sub>3</sub> PhO <sup>-</sup>	1.17
NH <sub>2</sub> C <sub>4</sub> PhO <sup>-</sup>	1.21

**Table 3.2.** Calculated values for the image-charge correction term,  $\Delta_2$ , for NH<sub>2</sub>C<sub>1</sub>PhO<sup>-</sup>, NH<sub>2</sub>C<sub>2</sub>PhO<sup>-</sup>, NH<sub>2</sub>C<sub>3</sub>PhO<sup>-</sup>, and NH<sub>2</sub>C<sub>4</sub>PhO<sup>-</sup>.

From the calculated values of  $\Delta_1$  and  $\Delta_2$  we calculate the total DFT+ $\Sigma$  correction for the HOMO energy level ( $\Delta\Sigma$ ) as shown in **Table 3.3**.

Molecule	$\Delta_1$ (eV)	$\Delta_2$ (eV)	$\Delta\Sigma$ (eV)
NH <sub>2</sub> C <sub>1</sub> PhO <sup>-</sup>	-2.46	1.1	-1.36
NH <sub>2</sub> C <sub>2</sub> PhO <sup>-</sup>	-2.47	1.14	-1.33
NH <sub>2</sub> C <sub>3</sub> PhO <sup>-</sup>	-2.46	1.17	-1.29
NH <sub>2</sub> C <sub>4</sub> PhO <sup>-</sup>	-2.46	1.21	-1.26

**Table 3.3.** Calculated total DFT+ $\Sigma$  correction ( $\Delta\Sigma$ ) from  $\Delta_1$  and  $\Delta_2$ .

We then fit the HOMO transmission resonance calculated from NEGF with a Lorentzian distribution,

$$f(x) = A \frac{\gamma^2}{(x - \epsilon_0)^2 + \gamma^2}$$

where  $A$  is the Lorentzian amplitude,  $\gamma$  is the Lorentzian width and  $\epsilon_0$  is the resonance peak position. The adjustment made with DFT+ $\Sigma$  only shifts the position of the Lorentzian peak by the calculated values of  $\Delta\Sigma$ , leaving the other parameters fixed. The  $\Delta\Sigma$  correction is subtracted from  $\epsilon_0$ , shifting the HOMO resonance away from  $E_F$ , and yielding the final DFT+ $\Sigma$  corrected HOMO resonance energy ( $\epsilon_\Sigma$ ).

### 3.3 Results and Discussion

#### 3.3.1 Experimental Measurements

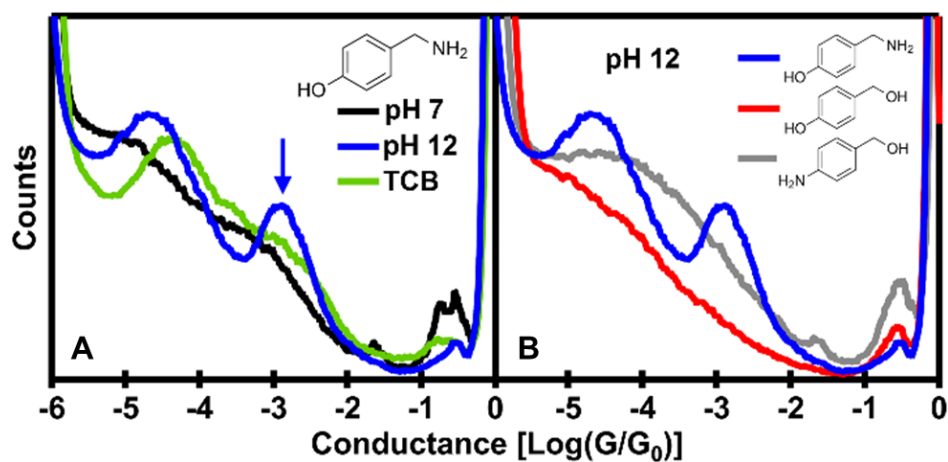


**Figure 3.1.** (A) 1D conductance measurements of 4-hydroxybenzylamine in pH 7 (black) and pH 12 (blue) aqueous conditions, as well as 4-hydroxybenzylamine in trichlorobenzene (green). (B) 1D Conductance measurements of 4-hydroxybenzylamine (blue), 4-hydroxybenzyl alcohol (red), and 4-aminobenzyl alcohol (gray) in pH 12 aqueous conditions.

Conductance histograms of 4-hydroxybenzylamine ( $\text{NH}_2\text{C}_1\text{PhOH}$ ) depicted in the inset of **Figure 3.1**, measured in various solvent conditions are shown in **Figure 3.1**.  $\text{NH}_2\text{C}_1\text{PhOH}$ , consists of a phenyl ring terminated by a hydroxy group on one end, forming a phenol, and a methylamine ( $\text{NH}_2\text{C}_1$ ) on the other, with the  $\text{NH}_2$  amine electron donor group terminating the molecule. No successful conductance measurements on a phenol have been reported in the literature to date. Our data in aprotic organic solvent 1,2,4-trichlorobenzene (TCB), plotted in green, are consistent with these prior findings, and show only a broad peak below  $10^{-4} G_0$ . Such dispersed low conductance peaks have been previously attributed to aromatic molecules containing only one functional linker group, in this case the amine, anchoring to opposite electrodes and  $\pi$ - $\pi$  stacking in the junction.<sup>158,159</sup> Here, we see that the feature is particularly pronounced in TCB, but is nearly absent in pH 7 aqueous conditions, shown in black. In TCB, amines are neutral and can bind in the junction to create  $\pi$ - $\pi$  stacked dimer junctions, while in neutral water, the amine (pKa  $\sim$ 9) is likely to be protonated and unable to anchor the molecule.<sup>49</sup> We verify this fact by measuring 1,4-benzenediamine, a standard aromatic diamine control, dissolved in pH 7 water and observe no conductance signals as shown in the **Figure 3.2**.<sup>44</sup> In pH 7 the phenol (pKa  $\sim$ 10) also remains protonated and does not bind, preventing the formation of through-bond conductance signatures with a single molecule bound to both electrodes.

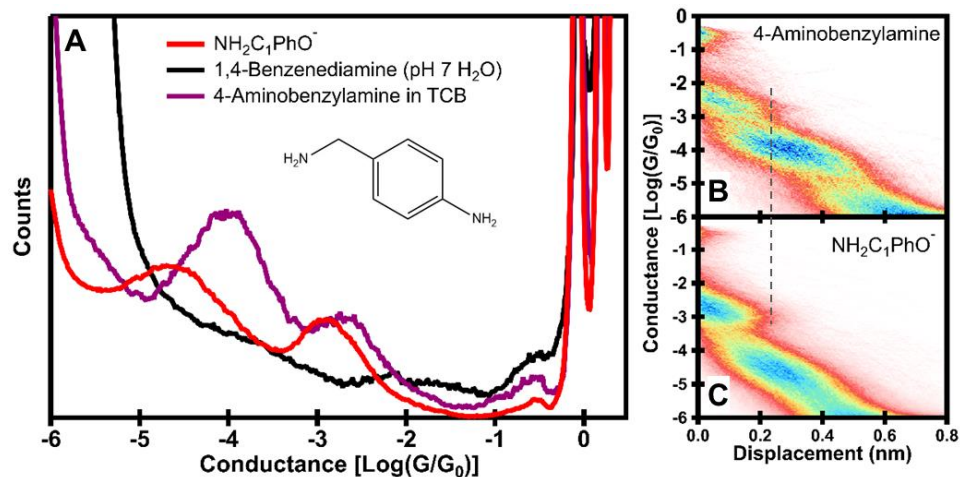


**Figure 3.2.** (A) Conductance histogram of 1 mM 1,4-benzenediamine in pH 7 H<sub>2</sub>O with a wax coated Au tip (black), 1.5 mM 4-aminobenzylamine in TCB (maroon) and NH<sub>2</sub>C<sub>1</sub>PhO<sup>-</sup> in pH 12 H<sub>2</sub>O (red). The structure of 4-aminobenzylamine is shown in the inset. (B, C) Conductance vs. displacement histogram of 4-aminobenzylamine and NH<sub>2</sub>C<sub>1</sub>PhO<sup>-</sup>. The dashed vertical line emphasizes the similar persistence of the two molecules with identical backbones but differing linkers.

Importantly, however, measurements of NH<sub>2</sub>C<sub>1</sub>PhOH in basic conditions, shown in blue in **Figure 3.1.A**, lead to the appearance of a distinct feature at a higher conductance regime indicated by an arrow and consistent with a single molecule signature where both ends are anchored to opposite electrodes. We compare these measurements on NH<sub>2</sub>C<sub>1</sub>PhOH to the conductance of an analogous diamine, 4-aminobenzilamine (4ABA), where the OH group is replaced by an amine. The results are plotted in **Figure 3.2** and show that both the single molecule and the  $\pi$ - $\pi$  stacked peak are similar in the two molecules, but the phenol has a somewhat higher conductance than the amine. We note that in pH 12 aqueous conditions, both the amine (pK<sub>a</sub> ~9) and the phenol (pK<sub>a</sub> ~10) are deprotonated so that the amine is neutral, and the phenol group becomes charged (NH<sub>2</sub>C<sub>1</sub>PhO<sup>-</sup>). These results suggest that the deprotonated phenol moiety, phenolate, can bind to gold to bridge metal-molecule junctions.

To understand which conditions, enable O-Au binding, we perform measurements, shown in **Figure 3.1.B**, on two control molecules, 4-hydroxybenzyl alcohol (red) and 4-aminobenzyl alcohol (gray) whose structures are shown in the inset. In both molecules, one of the linkers is a hydroxy moiety bound to a saturated chain (alcohol) rather than to an aromatic benzene (phenol). As a result, the pKa of these molecules is  $\sim 16$ , which is significantly higher than of a phenol and outside the accessible pH range with aqueous solvent. **Figure 3.1.B** makes clear that these molecules do not display a single molecule conductance feature, even at  $\text{pH} \gtrsim 12$  experimental conditions. We conclude that deprotonation is necessary to enable O-Au binding in the single molecule junction environment. Thus, a phenol with a pKa  $\sim 10$  is a viable linker group for single molecule conductance measurements in aqueous conditions where it can be deprotonated to phenolate at  $\text{pH} > 10$ , but an alcohol with a pKa  $\sim 16$ , is not.

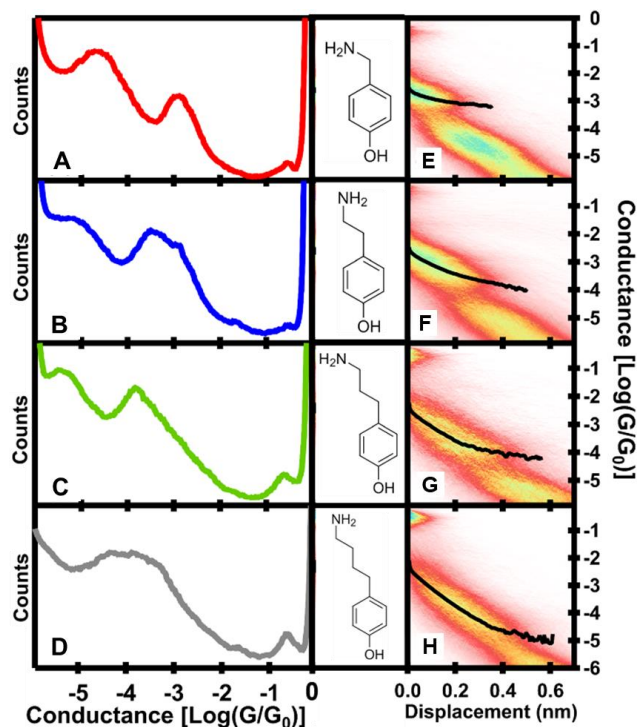


**Figure 3.3.** 1D conductance histograms and 2D conductance vs displacement histograms of  $\text{NH}_2\text{C}_1\text{PhO}^-$  (A, E),  $\text{NH}_2\text{C}_2\text{PhO}^-$  (B, F),  $\text{NH}_2\text{C}_3\text{PhO}^-$  (C, G) and  $\text{NH}_2\text{C}_4\text{PhO}^-$  (D, H). The black line in (E-H) is the gaussian fit of each vertical slice in the 2D histogram. The line cuts off after the amplitude of the Gaussian fit falls off by 85% below the maximum.

To study the conductance characteristics of phenolate ( $\text{PhO}^-$ ) as a linker group in break junction measurements, we measure the conductance decay of the series of alkanes, ranging in length from 1 to 4 methylene groups ( $\text{C}_1 = -\text{CH}_2-$ ,  $\text{C}_2 = -(\text{CH}_2)_2-$ ,  $\text{C}_3 = -(\text{CH}_2)_3-$ ,  $\text{C}_4 = -(\text{CH}_2)_4-$ ), terminated by  $\text{PhO}^-$  (measured in pH 12) and an amine, shown in **Figure 3.3**. We refer to these molecules as  $\text{NH}_2\text{C}_n\text{PhO}^-$ , where  $n$  ranges from 1 to 4. Each of the 1D conductance histograms (**Figure 3.3.A-D**), comprised of at least 5,000 individual pull-out conductance traces for all four molecules shows a pronounced single molecule conductance feature. This peak is higher in conductance than the  $\pi$ - $\pi$  stacking feature which is present in all molecules except in  $\text{NH}_2\text{C}_4\text{PhO}^-$  where it falls below the measurement

noise floor. We track the characteristic conductance of each molecule by fitting the peak to a Gaussian fit and determine the average conductance of  $\text{NH}_2\text{C}_1\text{PhO}^-$ ,  $\text{NH}_2\text{C}_2\text{PhO}^-$ ,  $\text{NH}_2\text{C}_3\text{PhO}^-$ ,  $\text{NH}_2\text{C}_4\text{PhO}^-$  to be  $10^{-2.92}$ ,  $10^{-3.37}$ ,  $10^{-3.80}$ , and  $10^{-4.06}$   $G_0$  respectively.

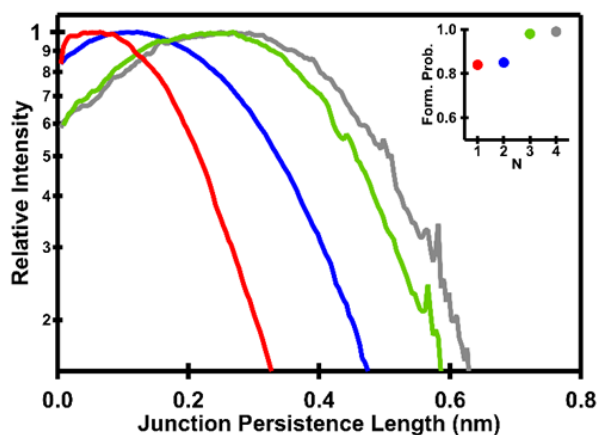


**Figure 3.4.** Junction persistence lengths of  $\text{NH}_2\text{C}_1\text{PhO}^-$  (red),  $\text{NH}_2\text{C}_2\text{PhO}^-$  (blue),  $\text{NH}_2\text{C}_3\text{PhO}^-$  (green), and  $\text{NH}_2\text{C}_4\text{PhO}^-$  (gray). The inset shows the calculated junction formation fraction for each molecule.

The 2D conductance vs. displacement histogram for these four alkanes is shown in **Figure 3.3.E-H** and provides information on the relative length of the molecular junction as well as how the conductance traces evolve during junction stretching. The black lines trace the average conductance at each junction extension determined via a Gaussian fit to a vertical slice of the 2D histogram. The extension where the Gaussian fits diminish by 85% of the peak amplitude is identified by the end of the black line and is interpreted as a representative length of a fully elongated molecular junction prior to junction rupture. The junction persistence lengths as well as junction formation probability determined for all molecules using molecular plateau length analysis techniques is shown in **Figure 3.4** and provides similar results.<sup>97</sup> Using both types of measurements, we find that as the number

of methylene groups increases, the persistence of the molecular junctions grows, so that average junction breakdown occurs at longer extensions between the electrodes. We observe a persistence length of  $\sim 3$  Å for  $\text{NH}_2\text{C}_1\text{PhO}^-$  and  $\sim 6$  Å for  $\text{NH}_2\text{C}_4\text{PhO}^-$  indicating that these molecules are fully elongated in the junction after stretching of 3 and 6 Å, respectively, beyond metallic rupture. Accounting for Au electrode relaxation (snapback) of  $\sim 5$  Å that occurs when gold point contacts break down and separate,<sup>16,97,111</sup> these lengths are consistent with the calculated molecular junction lengths of  $\sim 8$  Å and  $\sim 11$  Å for  $\text{NH}_2\text{C}_1\text{PhO}^-$  and  $\text{NH}_2\text{C}_4\text{PhO}^-$  respectively. Importantly, we find that the persistence length of  $\text{NH}_2\text{C}_1\text{PhO}^-$  and 4ABA, an analogous amine, in molecular junctions are very similar (**Figure 3.2.B**). In all cases, the extension lengths and persistence probabilities plotted in **Figure 3.3** and **Figure 3.4** are consistent with measurements done on conjugated diamine and carboxyl-linked molecules of similar length reported previously, suggesting that the phenolate-bound junctions are comparable in stability to other commonly used linkers.<sup>41,53,140,160</sup> These results and analysis confirm that the electrode binds to the fully extended molecule at the oxygen contact and not through van der Waals interaction with the phenyl ring which would result in shorter persistence in the junction.

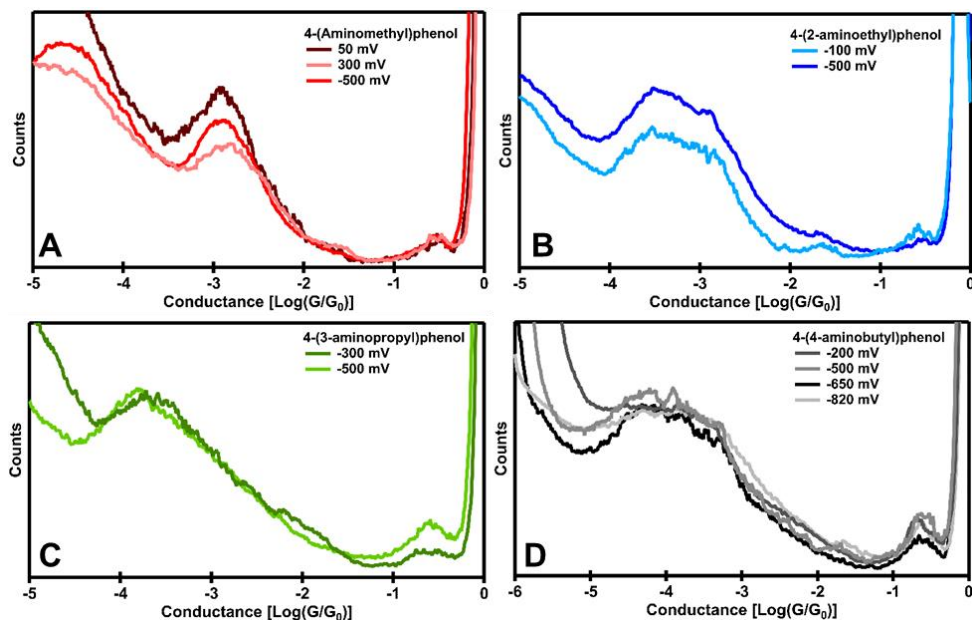


**Figure 3.5.** (A) Conductance histogram of  $\text{NH}_2\text{C}_1\text{PhO}^-$  at different junction biases (B) Conductance histogram of  $\text{NH}_2\text{C}_2\text{PhO}^-$  at different junction biases. (C) Conductance histogram of  $\text{NH}_2\text{C}_3\text{PhO}^-$  at different junction biases. (D) Conductance histogram of  $\text{NH}_2\text{C}_4\text{PhO}^-$  at different junction biases.

Additional measurements of  $\text{NH}_2\text{C}_1\text{PhO}^-$ ,  $\text{NH}_2\text{C}_2\text{PhO}^-$ ,  $\text{NH}_2\text{C}_3\text{PhO}^-$ ,  $\text{NH}_2\text{C}_4\text{PhO}^-$  are also shown in **Figure 3.5.A-D** at different junction biases, to ensure that these molecules do not have a bias dependence. Additionally, measurements were made in aqueous conditions (**Figure 3.6.A-D**) that show identical results to the measurements with molecules dried out of solution (**Figure 3.3**) that ensure there is no solvent or ion effect on the conductance of these molecules.

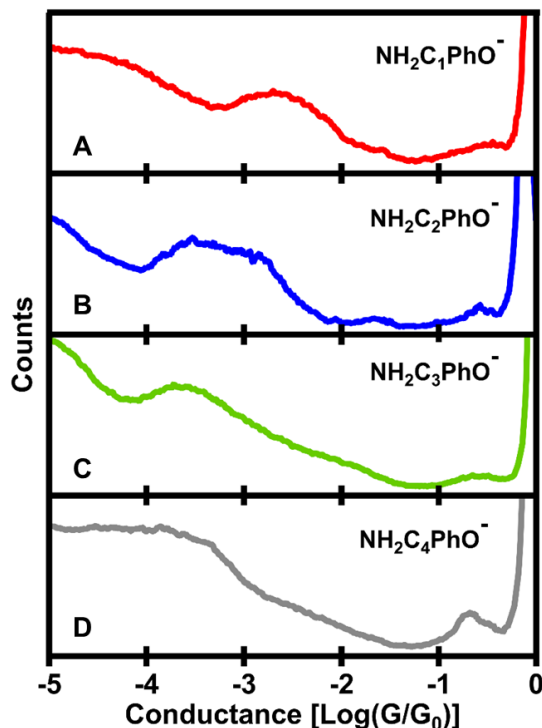


**Figure 3.6.** Conductance histograms of (A)  $\text{NH}_2\text{C}_1\text{PhO}^-$ , (B)  $\text{NH}_2\text{C}_2\text{PhO}^-$ , (C)  $\text{NH}_2\text{C}_3\text{PhO}^-$ , and (D)  $\text{NH}_2\text{C}_4\text{PhO}^-$  constructed from at least 5000 STMBJ traces collected in aqueous pH 12 conditions with a wax-coated tip at 500 mV bias.

To understand how the phenolate linker group effects conductivity through the alkane backbone, we plot the characteristic conductance values obtained from Gaussian fits of the 1D conductance histograms in **Figure 3.3.A-D**, against the number of methylene groups,  $N$  in **Figure 3.7.A** (gray). We observe a characteristic exponential decay with increasing number of methylene groups, which is a well-documented feature of off resonance tunneling in single molecule junctions. Using common practice, we fit the data with an exponential decay  $R_c^{-1}e^{-\beta N}$ , where  $\beta$  is the decay rate and  $R_c$  is the contact resistance of the two ends of the molecule. The experimental conductance decay rate,  $\beta_{\text{expt}}$ , is determined to be  $\beta_{\text{expt}} = 0.9 \pm 0.1$  per methylene. The value of  $\beta_{\text{expt}}$  matches previous

measurements for an alkane backbone which range from 0.8 to 1.1.<sup>24,44,137,161–163</sup> The measured  $R_c$  of the phenol linker is 4.5 M $\Omega$ , where we account for the  $R_c$  of the amine to be 215 k $\Omega$  as previously measured.<sup>44</sup> We note that the phenol  $R_c$  is comparable in magnitude to the  $R_c$  of similar linker groups such as pyridine, thiophenol and thioanisole, which are 1.9, 3.8-5.5, and 9 M $\Omega$  respectively.<sup>10,163,164</sup> The agreement between our measured  $R_c$  for the phenol and previously measured thiophenol further confirms that our single molecule conductance signatures are from direct O-Au binding and suggests that the electronic resistance characteristics of S-Au and O-Au links are similar.

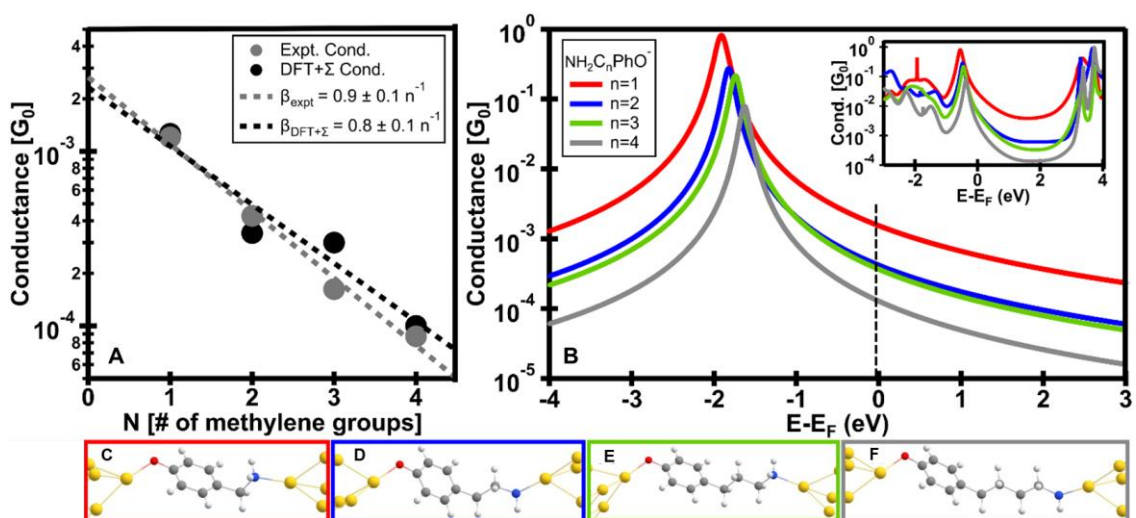


**Figure 3.7.** (A) Comparison of the experimentally determined and DFT+ $\Sigma$  calculated conductance values of  $\text{NH}_2\text{C}_n\text{PhO}^-$  ( $n=1-4$ ) including the exponential fit for both and the corresponding parameters. (B) DFT+ $\Sigma$  adjusted single level HOMO resonance involved in transmission calculated at  $E-E_F=0$  eV (dashed black line) for  $\text{NH}_2\text{C}_n\text{PhO}^-$  ( $n=1-4$ ). (B, inset) Initial transmission spectra calculated using NEGF. (C-F) Visualization of the lowest energy geometries of  $\text{NH}_2\text{C}_n\text{PhO}^-$  ( $n=1-4$ ) bound to two  $\text{Au}_{34}$  electrodes that are used for transmission calculations.

### 3.3.2 Theoretical Calculations

To investigate the binding configuration and electronic structure of phenolate terminated molecular junctions we relax each of the four alkane phenolates studied here bound to Au<sub>34</sub> electrodes (**Figure 3.7.C-F**) in the fully extended but still stable configuration. The Au-Au separation (edge-to-edge) in the order of increasing molecule lengths are found to be 7.6, 8.6, 10.1, and 11 Å which is consistent with the overall lengths and successive addition of a methylene group.<sup>44</sup> We calculate the expected electron transport of the four junctions using NEGF method from Kohn-Sham DFT (KS-DFT). The calculated transmission spectra for all four junctions are shown in the inset in **Figure 3.7.B**. We observe that the calculated low bias transmission evaluated at  $E-E_F = 0$  eV for all four junctions is  $\gtrsim 10^{-2} G_0$ , several orders of magnitude higher than the experimentally measured conductance plotted in **Figure 3.7.A**. We also find that the HOMO resonance is predicted to be within only  $\sim 0.5$  eV of  $E_F$ . This resonance near  $E_F$  magnifies effects of the known DFT underestimation of the HOMO-LUMO gap and results in a drastic overestimation of conductance.

To improve the accuracy of our calculation, we turn to DFT+ $\Sigma$  method to estimate the transmission. This method is well-suited to situations where conductance is dominated by a single resonance, in this case, the HOMO. The LUMO, at more than 3.5 eV away, can be neglected. The parameters, necessary for DFT+ $\Sigma$ , determined from the Lorentzian fits of the HOMO resonance in the inset of **Figure 3.7.B** are shown in **Table 3.4**. The final DFT+ $\Sigma$  corrected HOMO resonance energy ( $\epsilon_\Sigma$ ) for NH<sub>2</sub>C<sub>1</sub>PhO<sup>-</sup>, NH<sub>2</sub>C<sub>2</sub>PhO<sup>-</sup>, NH<sub>2</sub>C<sub>3</sub>PhO<sup>-</sup>

,  $\text{NH}_2\text{C}_4\text{PhO}^-$  is also shown in **Table 3.4** and are used to calculate transmission in **Figure**

### 3.7.B.

Molecule	A	$\gamma$ (eV)	$\epsilon_0$ (eV)	$\epsilon_\Sigma$ (eV)
$\text{NH}_2\text{C}_1\text{PhO}^-$	0.82	0.08	-0.55	-1.91
$\text{NH}_2\text{C}_2\text{PhO}^-$	0.28	0.07	-0.49	-1.82
$\text{NH}_2\text{C}_3\text{PhO}^-$	0.22	0.07	-0.45	-1.74
$\text{NH}_2\text{C}_4\text{PhO}^-$	0.08	0.07	-0.37	-1.63

**Table 3.4.** Lorentzian Fitting parameters from the NEGF transmission spectra as well as the DFT+ $\Sigma$  corrected HOMO resonance energy ( $\epsilon_\Sigma$ ).

The DFT+ $\Sigma$  predicted HOMO resonance position and width for all four molecular junctions are represented by a Lorentzian curve plotted relative to  $E-E_F$  in **Figure 3.7.B**. We find that the DFT+ $\Sigma$  correction shifts the resonance for all molecules  $\text{NH}_2\text{C}_1\text{PhO}^-$ ,  $\text{NH}_2\text{C}_2\text{PhO}^-$ ,  $\text{NH}_2\text{C}_3\text{PhO}^-$ ,  $\text{NH}_2\text{C}_4\text{PhO}^-$  by  $\sim 1.3$  eV away from the Fermi energy to -1.91, -1.82, -1.74, -1.63 eV, respectively. This shift of the HOMO in the DFT+ $\Sigma$  comes from two distinct contributions: the gas-phase correction and image charge correction.<sup>153</sup> Notably, we find the gas-phase correction for the four molecules is approximately -2.2 eV, which is significantly larger than is typical for neutral systems and emphasizes the need for DFT+ $\Sigma$  correction for this case. We note that the large offset found here for phenolates  $\text{PhO}^-$  reflects the documented difficulty of KS-DFT to predict the energy levels of anions, which exacerbates the standard HOMO-LUMO gap underestimation of DFT methods.<sup>165–167</sup> We note that further work on charged molecular junctions may require the DFT+ $\Sigma$  methodology detailed and validated here for anions bound to two electrodes. We compare the calculated conductance values, obtained by evaluating the transmission in **Figure 3.7.B** at  $E_F$  and plotted in **Figure 3.7.A** (black), with experimental measurements (gray). We

observe strong agreement for all four molecular junctions; the DFT+ $\Sigma$  calculated decay  $\beta_{DFT+\Sigma}$  falls within the statistical uncertainty of the measured  $\beta_{expt}$ , validating the application of this method to charged molecular junctions.

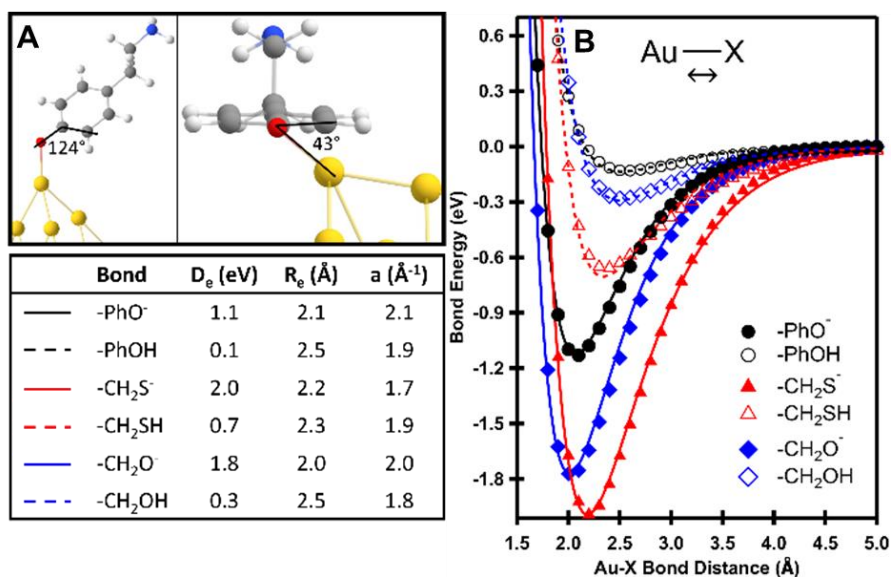


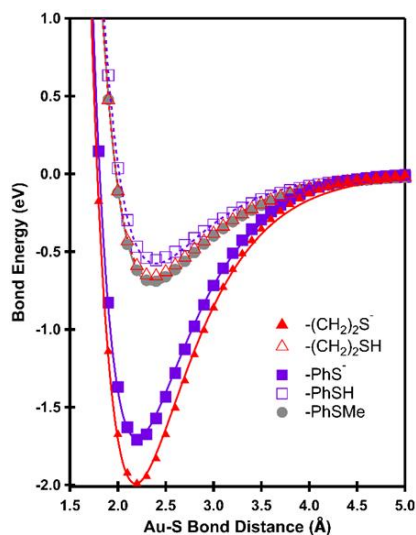
**Figure 3.8** (A) Binding configuration of Au<sub>34</sub>-NH<sub>2</sub>C<sub>2</sub>PhO<sup>-</sup>. (B) Potential energy scan against length of the Au-X (X=PhO<sup>-</sup>, PhOH, CH<sub>2</sub>S<sup>-</sup>, CH<sub>2</sub>SH, CH<sub>2</sub>O<sup>-</sup>, CH<sub>2</sub>OH) bond, with Au electrode modelled as Au<sub>34</sub>. The Au apex atom is bound to either O or S in all cases. Data points were fit with Morse potential function, plotted as solid lines.

**Table 3.5.** Morse Potential Fitting Parameters determined from Figure 3.8.A [well depth ( $D_e$ ), equilibrium bond length ( $R_e$ ), well width ( $a$ )].






We examine the character of the PhO<sup>-</sup>-Au bond by studying the geometry of the NH<sub>2</sub>C<sub>2</sub>PhO<sup>-</sup>-Au<sub>34</sub> interface, shown in **Figure 3.8.A**. We observe a ~124° angle between Au-O-C (left) with the Au-O bond rotated ~45° clockwise relative to the plane of the phenyl ring (right). These observations indicate that a distortion from the original sp<sup>2</sup> hybridization of the phenolate to sp<sup>3</sup> occurs upon binding to gold. These changes in the

electron distribution and local density of states are characteristic of a strong physisorption interaction or even of chemisorption.<sup>168–171</sup>

The strong nature of the binding is also evident in the calculated Morse potential shown in **Figure 3.8.B** (solid markers). The well depth or interaction energy ( $D_e$ ), and equilibrium bond length ( $R_e$ ) for  $\text{PhO}^-$  are 1.1 eV and 2.1 Å respectively. This is significantly stronger than the 0.6 eV dative donor acceptor interaction of amines to undercoordinated Au atoms commonly used in STMBJ measurements.<sup>46,67,172</sup> Interestingly, the Morse potential fit for a deprotonated alcohol ( $\text{CH}_2\text{O}^-$ ) binding to Au shows an even stronger bond at 1.8 eV, but it is not observed in experiment due to the high pKa of alcohol which makes deprotonation impossible in aqueous conditions. Importantly, we also note that a protonated phenol ( $\text{PhOH}$ ) or alcohol ( $\text{CH}_2\text{OH}$ ) has a binding energy of 0.1 or 0.3 eV respectively, which is insufficient for stable junction formation at room temperature.



**Figure 3.9** Potential Energy scan of the Au-S bond with molecules terminated by  $-(\text{CH}_2)_2\text{SH}$ ,  $-(\text{CH}_2)_2\text{S}^-$ ,  $-\text{PhSH}$ ,  $-\text{PhS}^-$ , and  $-\text{PhSMe}$ . Data points were fit with a Morse Potential Fitting function.

	Bond	$D_e$ (eV)	$R_e$ (Å)	$a$ (eV)
	$-(CH_2)_2S^-$	2.0	2.2	1.7
	$-(CH_2)_2SH$	0.7	2.3	1.9
	$-PhS^-$	1.7	2.2	1.8
	$-PhSH$	0.6	2.4	1.9
	$-PhSMe$	0.7	2.4	1.8

**Table 3.6 Morse Potential fitting parameters obtained from Figure 3.9.**

Interestingly, we see in **Figure 3.8.B** that the interaction strength of thiolate ( $CH_2S^-$ ) at 2.0 eV is comparable to the alcohol interaction. The thiols in **Figure 3.8.B** are alkyl thiols, but similar analysis and results were obtained with thiophenols, as shown in **Figure 3.9** and **Table 3.6**. Critically, unlike the weak binding of OH, the SH moiety binds to gold with an appreciable binding energy of 0.7eV. These calculations support recent measurements which show that thiol can retain the proton during junction formation and stretching at room temperature.<sup>57</sup> We conclude that while hydroxy moieties need to be activated through environmental removal of the proton in order to bind, the thiol will bind even in its protonated state. This donor-acceptor interaction of the protonated thiol may then be converted to a covalent bond between thiolate and gold which leads to disruptive intercalation of the thiolate into the electrode structure and the broadening of gold and molecular conductance signatures.<sup>99</sup>

These differences between phenol and thiol Au interactions are instructive for future design of linker moieties. Our results suggest that in addition to the energetics of the final binding configuration, which are similar for the S-Au and O-Au cases, the transition

state energy and the existence of intermediate stable binding configurations are important to consider. Unlike thiolates, phenolates discovered here bind strongly, but non-destructively. The lack of a stable intermediate binding configuration between the neutral protonated phenol and the gold, prevents binding in neutral conditions and results in a linker which binds strongly and can be activated using environmental pH.<sup>99,173</sup>

### 3.4 Conclusions

Our results here show that a phenol group can be used as an affective linker group for metal-molecule junctions and is activated for binding in aqueous conditions through external pH control. Our break junction measurements show a single conductance signature associated with binding to Au electrodes via the deprotonated oxygen in a phenol that is not present when phenol or alcohol is protonated. Measurements with a series of alkanes using the phenolate as a linker group match the expected alkane conductance decay with molecule length. The calculated electron transport through the series of alkane phenolates anchored on gold with direct O-Au links, matches experiment when DFT+ $\Sigma$  adjustments are made to the HOMO dominated transmission spectra. We show that the Au-phenolate interaction has characteristics similar to the Au-thiolate bond but is more selective for binding configurations where the proton is removed. This selectivity results in the ability to control binding through external environment and reduces intercalation into the gold electrodes characteristic of thiol-linked junctions. This study of a new robust linker group for molecular junction measurements offers insight into features of metal-molecule interactions necessary for successful junction formation and opens the door to a broader

range of molecular junctions and capabilities. This work points to an effective binding strategy for biological molecules rich in phenols, such as nucleic or amino acids, to gold surfaces without required labeling or modification for single molecule conductance, optical spectroscopy, or other applications.

.

## CHAPTER 4 Topological Insulator Single Molecule Junctions with Intermediate Diradicals Result in Anti-ohmic Conductance

### 4.1 Introduction

With increasing drive for miniaturization, the properties of nanoscale materials such as individual particles or molecules take on added significance for the development of future technologies. For example, passing electronic current across single molecules attached to metal electrodes has been shown to result in switching or diode-like behavior, raising the prospect of molecules as active components in next generation electronic devices.<sup>1,43,52,174–186</sup> Appealingly, the properties of such molecular circuits can be tuned using synthetic control of the molecular atomic structure and of the terminal linking elements that affect how the molecule arranges on the metal and how its electronic states hybridize with the metallic bands. A challenge in the field is that electronic states of an organic molecular bridge are typically off-resonance with the Fermi energy of the conducting electronics in the metal.<sup>187–189</sup> As a result, typical molecular junctions behave as quantum tunnel barriers, and tend to be highly insulating, with an electronic conductance that decreases exponentially with molecule length.<sup>22,189</sup> Thus, with few exceptions, molecules longer than ~2nm in length have vanishing conductance and limited usefulness as candidates for nanoscale electronics.<sup>13,190–193</sup> Developing molecular materials that overcome this limitation is an important challenge for the field.

Recent work has identified radical molecules with open-shell electronic structures containing unpaired electrons, as molecular wires with topologically non-trivial electronic

states that can sustain higher conductance over longer lengths.<sup>11,13,194</sup> At room temperature and ambient conditions, charged diradicals generated through chemical oxidation were shown to behave as 1D topological insulators and to exhibit anti-ohmic behavior, with conductance increasing in with molecular length up to  $\sim 1.5$  nm and then decreasing again.<sup>11</sup> This reversal to conductance decay in longer charged organic diradicals was attributed to decreased coupling of edge topological states across the extended molecular backbone.<sup>11,39</sup> Incorporating many charged diradicals in series in a single molecule, restored anti-ohmic trends, but required challenging experimental protocols to maintain the high oxidation charged state of a single organic wire.<sup>13</sup>

Here, we report anti-ohmic behavior at room temperature in neutral diradicaloid molecules composed of cyclic aromatic units fused together as in a flake of graphene (**Figure 4.1**). Critically, we show that these molecules require no chemical or field oxidation to reach the inverse conductance decay regime, simplifying the junction formation process and enabling further characterization of diradical junction phenomenon. We adapt and extend the 1D Su-Schrieffer-Heeger (1D-SSH) model to present and analyze the effect of topologically non-trivial electronic states on conductance in cyclic planar aromatic compounds studied here. By adjusting the 1D-SSH model parameter to reflect established bond orders in graphene-derived structures, we demonstrate that the anti-ohmic behavior observed here experimentally is intrinsic in this family of molecules. The intermediate diradical character  $y$  in such conjugated planar structures means that increasing molecular length closes the band-gap, and compensates for decreased coupling across the backbone, leading to inverse conductance decay over longer lengths scales.

Critically, our model applies to other families of conjugated cyclic planar systems and guides the discovery of highly conducting molecular circuits based on cyclic neutral diradical compounds.

## 4.2 Experimental Section

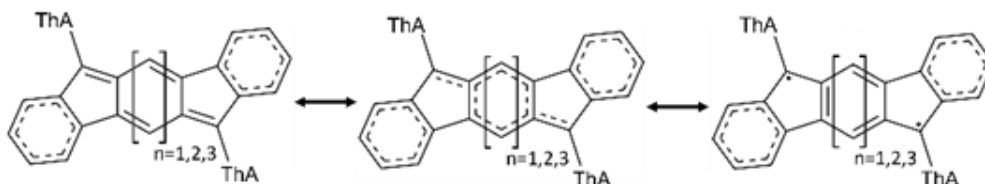


**Figure 4.1** Resonance structures converting between the quinone, delocalized and diradical form of the family of benzofused quinoids ( $BQ_n$ ) where  $n=1-3$  with thioanisole linkers (ThA).

We perform room temperature single molecule conductance measurements of the series ( $n=1, 2, 3$ ) of polycyclic aromatic compounds, benzofused quinoids ( $BQ_n$ ), shown in **Figure 4.1** using a scanning tunneling microscope break junction (STMBJ).<sup>3,44,87</sup> The  $BQ$  series are characterized by an intermediate diradical character ( $y = 0.3 - 0.7$ ) that arises from the preference for aromaticity in the diradical (**Figure 4.1** right) over the increased number of double bonds in the quinone resonance structure (left). A transition state between the two is a fully delocalized system shown in the middle. Generally, as the number of fused phenyl rings increases, the diradical character of the molecule also increases so that  $y = 0.30, 0.44, 0.61$  for  $n=1, 2, 3$  respectively, reflecting a higher residence of the molecules in the diradical structure over the quinone. Overall, these molecules have been shown to be air stable open-shell singlet diradicals with long term stability at room

temperature.<sup>195–200</sup> It is important to note that the diradical character is inherent to the molecule and independent of solvent conditions though it can be synthetically tuned.

The polycyclic core of the molecules is functionalized with a 3,5-dimethylthioanisole group (ThA in **Figure 4.1**) to bind to the Au electrodes. The methyl groups at the 3- and 5- positions ensure that the linker group is roughly perpendicular to the plane of the molecule and decrease coupling of the diradical core to the linker group and to the electrodes. No oxidation was required and, all measurements in the STMBJ were performed in 1 mM solution of bromonaphthalene (BNP), a nonpolar organic solvent.

STMBJ measurements are performed by repeatedly crashing and pulling out an Au tip from an Au substrate in the presence of molecules in solution, with a fixed bias across the two electrodes while recording the current, voltage, as well as the electrode displacement. Conductance is calculated at every displacement point during pull out by dividing current by voltage to generate a conductance trace. Plateaus in the conductance trace indicate formation of persistent junction configurations with a well-defined conductance. We statistically analyze the measurements by constructing 1D conductance histograms and 2D conductance vs displacement histograms from thousands of individually recorded raw data traces as detailed previously.<sup>16,66,87</sup> Reproducible molecular conductance plateaus result in peaks in the histograms in the conductance range below 1  $G_0$ .

### 4.3 Results and Discussion

**Figure 4.2.A** and **Figure 4.2.B** show 1D and 2D histograms, respectively, constructed from more than 5000 traces recorded in the presence of molecules BQ<sub>1-3</sub>. In the top panel of **Figure 4.2.A**, we compare the conductance histograms of BQ<sub>1-3</sub> measured at the same low bias of 100mV. We observe distinct peaks, attributable to the formation of stable single molecule junctions with each molecule. Importantly, we observe a conductance increase with increasing molecule length from 1 to 3 repeating quinone units. **Figure 4.2.C** shows the most likely conductance of each molecule, determined from gaussian fits to the histograms, plotted against the number of repeating units,  $n$ . Fitting the conductance trend to the expected Landauer model:

$$G = G_c e^{\beta L}$$

where  $G_c$  is the contact conductance,  $\beta$  is the conductance decay constant, and  $L$  is the length of the molecules, we obtain a positive beta value of  $1.7 \text{ \AA}^{-1}$  for these low bias measurements. The positive value of the beta indicates a reverse conductance decay and anti-ohmic transport trends in these molecules in the absence of chemical oxidant or high bias.

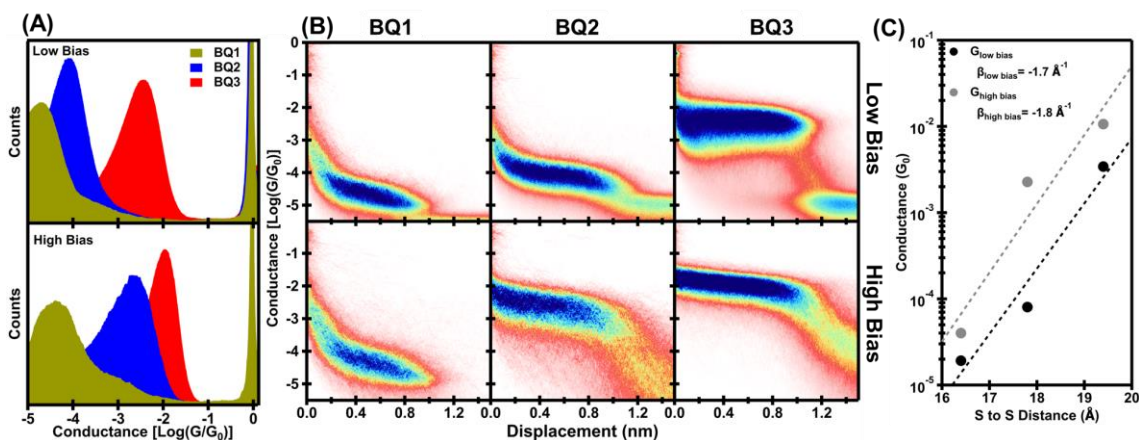


**Figure 4.2** (A) Single-molecule conductance histograms of  $BQ_n$  ( $n=1-3$ ) in BNP at low bias (-100 mV) in the top panel and high bias (-833 mV for  $BQ_{1-2}$  and -250 mV for  $BQ_3$ ) in the bottom panel. (B) Single-molecule 2D conductance vs displacement histograms of  $BQ_n$  ( $n=1-3$ ) at low bias in the top three panels and high bias in the bottom three panels. (C) Calculated conductance from gaussian fits to the peaks in Figure 4.2.A for both low bias (black) and high bias (gray) with exponential fits given by the dashed lines.

The 1D conductance histograms shown in the bottom of **Figure 4.2.A**, show conductance of the 3 molecules at a higher bias voltage of at least 250 mV. Crucially, these plots indicate a dramatic increase in single molecule junction conductance with bias, especially for  $n=2$  and  $n=3$ . We also observe in **Figure 4.2.A-B**, that the distribution of measured conductance values with  $BQ_{2-3}$  narrows at higher bias, a feature that has been previously identified as a signature of near-resonant transport.<sup>201</sup> We note that molecular conductance signatures for  $BQ_3$  are abrogated at biases above  $\sim 400$  mV as shown in the SI and discussed further below. Increases in the conductance of  $BQ_{2-3}$  at higher bias lead to an increase in anti-ohmic characteristics in these conditions, with a fit to the most likely conductance values in **Figure 4.2.C** yielding a  $\beta$  of  $1.8 \text{ \AA}^{-1}$ ; this corresponds to an unprecedented increase of nearly 3 orders of magnitude from  $n = 1$  to  $n = 3$ .

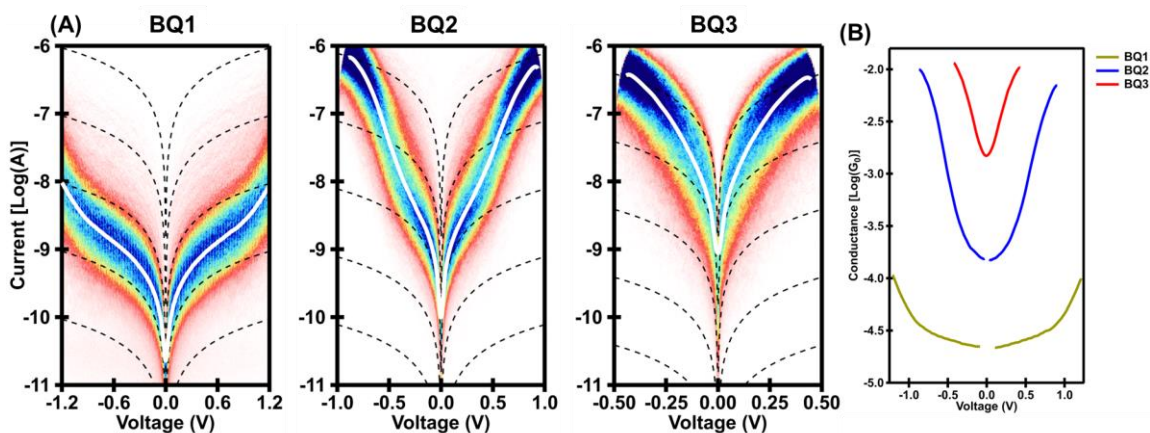


**Figure 4.3** (A) Current-Voltage histograms for  $BQ_n$  ( $n=1-3$ ) from thousands of IV curves taken while holding each molecule between two Au electrodes. Dotted lines correspond to the

**linear grid lines and the white lines are calculated from the average of gaussian fits of vertical slices of each histogram IV histogram. (B) Fits of the conductance-voltage histograms derived from the current-voltage histograms for n=1,2,3.**

To understand the voltage dependent conductance behavior of each molecule and estimate the position of the frontier electron orbitals relative to  $E_F$ , we perform single molecule current-voltage (IV) measurements by sweeping the voltage between the two electrodes while the molecule is held in the junction and recording the current using previously published protocols.<sup>52</sup> IV histograms for n=1-3, constructed from at least 5000 traces, are shown in **Figure 4.3.A**, with the average IV curve, shown in white, calculated from gaussian fits to vertical slices at each voltage; the dotted black lines are linear IVs shown for references. We observe clear differences in the IV characteristics of the three molecules. The shortest (n = 1) molecule shows a linear current-voltage relationship below ~500mV, typical of molecules with a large HOMO-LUMO gap,  $E_{\text{gap}}$ ; the current starts to increase exponentially above ~600 mV, suggesting that at the higher bias, the probed voltage range of  $\pm 300$  mV around  $E_F$  approaches a resonance feature associated with a frontier electronic state in the transmission spectrum of BQ<sub>1</sub>. The intermediate molecule (n = 2) shows exponentially increasing current at biases larger than ~50 mV, suggesting a small  $E_{\text{gap}}$ , on the order of ~100 mV. The IV curve for n = 2 resumes a linear IV relationship at high biases after the bias window opens beyond the location of the frontier states in the spectrum. The longest molecule (n = 3) shows exponential current increase even at the lowest biases. Beyond ~400 mV, BQ<sub>3</sub> conductance features switch irreversibly to a distinct lower conductance regime, suggesting a chemical change to the molecule at these higher

biases which we do not show in **Figure 4.3.B**. Overall, data in **Figure 4.3.B**, indicates a decreasing band gap in the BQ series as the number of repeating fused benzene units increases. Furthermore, at all biases measured, the conductance behaves anti-ohmically.

The key results from our experimental studies described above are two-fold. First, we establish clear anti-ohmic behavior in a family of neutral diradicaloids with the highest  $\beta$  parameter recorded to date in single molecule junctions. Second, our IV measurements at room temperature show clear evidence of a bandgap which diminishes with molecule length but is still present even for the longest molecule in the series, suggesting further increase in conductance can occur in more extended molecular wires.

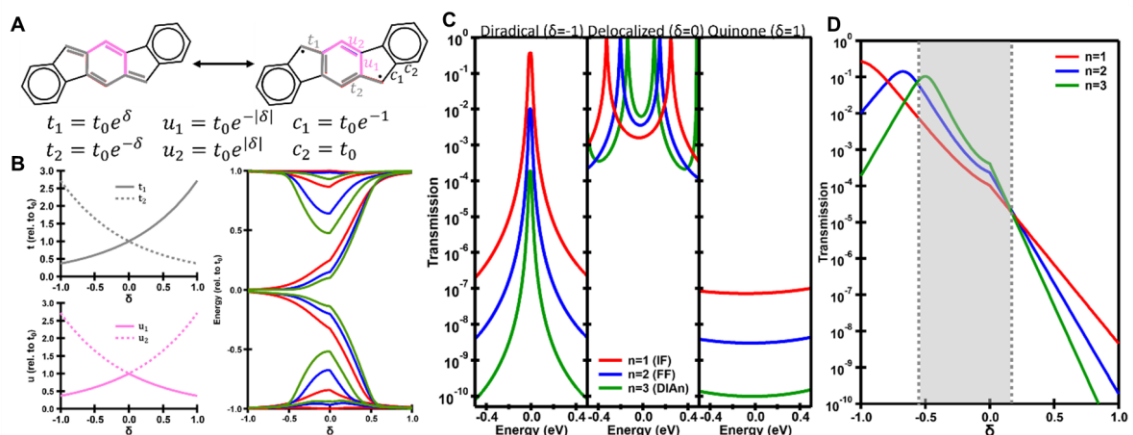


**Figure 4.4** (A) Description of the hopping terms ( $t_1, t_2, u_1, u_2, c_1, c_2$ ) describe by bond order alternation parameter ( $\delta$ ) used in the modified 1D SSH Hamiltonian. (B) Graphical representation of the hopping terms  $t_1, t_2, u_1, u_2$  and the calculated band structure for  $n=1, 2, 3$  molecules as a function of  $\delta$ . (C) Transmission spectra near  $E_f$  using NEGF from the 1D-SSH Hamiltonian for  $n=1, 2, 3$  molecules at  $\delta = -1, 0, 1$ . (D) Calculated transmission for  $n=1, 2, 3$  molecules as a function of  $\delta$ . The region of  $\delta$  where the molecules exhibit anti-ohmic conductance is shown in the shaded gray region.

To understand our experimental results, we develop a 1D-SSH model to describe the electron transport properties of cyclic systems such BQ<sub>1</sub>-BQ<sub>3</sub> studied here. In prior studies, the 1D-SSH or tight-binding Hamiltonian was used to describe linear chains such

as polyenes, which are molecules composed of a series of alternating single and double bonds, as shown in the grey path through a polycyclic molecule in **Figure 4.4.A**. In a Hamiltonian formalism, the double and single bonds correspond to a large and small hopping probability respectively.<sup>202</sup> For linear molecules, a single parameter  $\delta$  was used to parameterize the transition between resonance structures, with  $1 > \delta > -1$ , spanning the range from zero diradical character  $y = 0$ , to full diradical,  $y = 1$ , respectively. This is done by setting the hopping probability terms  $t_1$  and  $t_2$  to scale as  $e^{\pm\delta}$  as shown in **Figure 4.4.A**. In this approach, the grey bonds alternate between double (high hopping probability) and single (low hopping probability) as  $\delta$  goes between -1 ( $t_1 < t_2 \rightarrow$  diradical) and 1 ( $t_1 > t_2 \rightarrow$  polyene). Intermediate values of  $\delta$  describe intermediate scenarios, with  $\delta = 0$  corresponding to a fully delocalized electronic state. As polyene diradicals are not stable and thus experimentally inaccessible, this earlier model was shown to qualitatively describe transport trends of other non-polycyclic diradical systems.<sup>39,203</sup>

Here, we implement a 1D-SSH Hamiltonian for polycyclic systems where at least two paths through the molecule are present as shown in **Figure 4.4.A**. We observe that in the pink path, the bonds do not flip from double to single in the transition from  $\delta = -1$  (diradical aromatic) to  $\delta = 1$  (closed-shell quinone). These bonds are described by alternative hopping terms ( $u_1, u_2$ ) given by  $e^{\pm|\delta|}$  and they retain the same bond order value at  $\delta = -1$  and  $\delta = 1$ . Graphical representations of all hopping parameters as a function of  $\delta$  are shown on the left side of **Figure 4.4.B**. Critically, using this parameterization, all bonds  $t_1, t_2, u_1$  and  $u_2$  are equivalent when  $\delta = 0$  and the molecule is in a fully delocalized state.

Finally, the delocalized benzene ring at the extrema of the molecules are described as constants ( $c_1, c_2$ ), but do not participate in transport.

The band structures for the BQ series derived using the framework described above are shown in the right side of **Figure 4.4.B**. As expected, the electronic structure transitions between the quinone and diradical states as the range of  $\delta$  is scanned. We observe a wide bandgap in the quinone ( $\delta = 1$ ) structure, which closes as the molecule become a diradical ( $\delta = -1$ ). We can see a transition point near  $\delta = 0.6$  where the  $E_{\text{gap}}$  for the longest molecule is equal to the  $E_{\text{gap}}$  for the shortest molecule. At all values of  $\delta < 0.6$ , the  $E_{\text{gap}}$  for  $n = 3$  is less than that for  $n = 1$ .

We use the wideband limit within the non-equilibrium Green's function (NEGF) approach described previously to calculate the transmission spectra of molecules BQ<sub>1-3</sub>. These are shown in **Figure 4.4.C**. Focusing at the low-bias regime near  $E_F$ , we see that the molecules are insulating in the quinone structure ( $\delta = 1$ ), shown on the right of Figure 4.4. C, where the band-gap is large, with a featureless transmission spectrum around  $E_F$  and a transmission probability many orders of magnitude below unity. Furthermore, the conductance of these hypothetical closed-shell structures follow standard ohmic behavior, decreasing with molecule length. Interestingly, we see that the diradical state ( $\delta = -1$ ), shown in the left panel of **Figure 4.4.C**, also exhibits Ohmic behavior, which is distinct from our experimental results. In this topology, the transmission is on-resonance with the MO edge states, but the amplitude of the resonance decays with length due to decreased coupling of the edges through the longer molecule backbones. This is consistent with behavior of linear molecular chains described previously.<sup>39</sup> Critically, we observe that our

polycyclic 1D-SSH model predicts anti-ohmic behavior to occur at intermediate diradical character, near  $\delta = 0$  shown in the middle panel of **Figure 4.4.C**, which is consistent with experimental measurements for the BQ<sub>1-3</sub> series whose  $y$  values fall in this range.

To determine the range of  $\delta$  that leads to anti-ohmic behavior, we calculate the transmission at  $E_F$  for  $n= 1, 2, 3$  at all values of  $\delta$ , as shown in **Figure 4.4.D**. This calculation shows a range of  $\delta$  values characterized by anti-ohmic conductance, specifically  $-0.6 < \delta < 0.2$ . We emphasize that this region near  $\delta = 0$  corresponds to intermediate diradicals, with significant contributions from the closed-shell state, suggesting that fully-open shell systems are not necessarily key to achieving high conductance in longer polycyclic molecular wires. We note that this is distinct from linear polymers such as polyenes, where only non-trivial topology, which is not experimentally accessible, yields reverse conductance decay. We have identified a unique class of molecular organic diradicals with a fused polycyclic core, where the equilibrium electronic structure is optimal for conductance enhancement in longer molecular systems.

### 4.3 Conclusions

In conclusion, we characterize transport properties of polycyclic neutral diradicals at room temperature and demonstrate anti-ohmic conductance behavior in a series of molecules of varying length. We find that inverse conductance decay is intrinsic to these compounds and occurs at all bias voltages and in all solvents, in the absence of oxidants. We develop a 1D-SSH model to accurately describe qualitative features of the band structure of similar polycyclic neutral diradicals. Our results reveal that anti-ohmic

properties key to high conductance of longer molecules are characteristic of intermediate diradical character materials and guide future design of molecular compounds for single molecule electronics applications.

**BIBLIOGRAPHY**

## List of Journal Abbreviations

Acc. Chem. Res.	Accounts of Chemical Research
ACS Appl. Mater. Interfaces	American Chemical Society Applied Materials & Interfaces
ACS Nano	American Chemical Society Nano
ACS Sensors	American Chemical Society Sensors
Anal. Chem.	Analytical Chemistry
Angew. Chem., Int. Ed.	Angewandte Chemie International Edition
Appl. Phys. Lett.	Applied Physics Letters
Appl. Sci.	Applied Sciences
Biochem. Soc. Trans.	Biochemical Society Transactions
Chem. - A Eur. J.	Chemistry – A European Journal
Chem. Commun.	Chemical Communications
Chem. Phys.	Chemical Physics
Chem. Phys. Lett.	Chemical Physics Letters
Chem. Sci.	Chemical Science
Chem. Soc. Rev.	Chemical Society Reviews
Chinese Chem. Lett	Chinese Chemical Letters
Chinese J. Inorg. Chem.	Chinese Journal of Inorganic Chemistry
Comput. Phys. Commun.	Computer Physics Communications

Coord. Chem. Rev.	Coordination Chemistry Reviews
Electrochem. Commun.	Electrochemical Communications
Faraday Discuss.	Faraday Discussions
J. Am. Chem. Soc.	Journal of the American Chemical Society
J. Chem. Phys.	Journal of Chemical Physics
J. Chem. Theory Comput.	Journal of Chemical Theory and Computation
J. Electron. Mater.	Journal of Electronic Materials
J. Mater. Chem. C.	Journal of Materials Chemistry C
J. Math. Phys.	Journal of Mathematical Physics
J. Organomet. Chem.	Journal of Organometallic Chemistry
J. Phys. Chem. B	Journal of Physical Chemistry B
J. Phys. Chem. C	Journal of Physical Chemistry C
J. Phys. Chem. Lett.	Journal of Physical Chemistry Letters
J. Phys. Condens. Matter	Journal of Physics: Condensed Matter
Nano Lett.	Nano Letters
Nano Res.	Nano Research
Nanoscale Res. Lett.	Nanoscale Research Letters
Nat. Nanotechnol.	Nat Nanotechnol
Nat. Chem.	Nature Chemistry
Nat. Commun.	Nature Communications
Nat. Mater.	Nature Materials
Nat. Nanotechnol.	Nature Nanotechnology

Nat. Rev. Mater.	Nature Reviews Materials
New J. Phys.	New Journal of Physics
Org. Electron.	Organic Electronics
Organometallics	Organometallics
Phy. Chem. Chem. Phys.	Physical Chemistry Chemical Physics
Phys. Rep.	Physical Reports
Phys. Rev.	Physical Review
Phys. Rev. B	Physical Review B
Phys. Rev. Lett.	Physical Review Letters
Polyhedron	Polyhedron
PNAS	Proceedings of the National Academy of Sciences
Rev. Mod. Phys.	Reviews of Modern Physics
Rev. Sci. Instrum.	Reviews of Scientific Instruments
Sci. Adv.	Science Advances

## References

- (1) Aviram, A.; Ratner, M. A. Molecular Rectifiers. *Chem. Phys. Lett.* **1974**, *29* (2), 277–283.
- (2) Reed, M. A.; Zhou, C.; Muller, C. J.; Burgin, T. P.; Tour, J. M. Conductance of a Molecular Junction. *Science* **1997**, *278* (October), 1–3.
- (3) Xu, B.; Tao, N. J. Measurement of Single-Molecule Resistance by Repeated Formation of Molecular Junctions. *Science* **2003**, *301* (5637), 1221–1223.

- (4) Bumm, L. A.; Arnold, J. J.; Cygan, M. T.; Dunbar, T. D.; Burgin, T. P.; Jones, L.; Allara, D. L.; Tour, J. M.; Weiss, P. S. Are Single Molecular Wires Conducting? *Science* **1996**, *271* (5256), 1705–1707.
- (5) Dorogi, M.; Gomez, J.; Osifchin, R.; Andres, R. P.; Reifenberger, R. Room-Temperature Coulomb Blockade From. *Phys. Rev. B* **1995**, *52* (12), 9071–9077.
- (6) Andres, R. P.; Bein, T.; Dorogi, M.; Feng, S.; Henderson, J. I.; Kubiak, C. P.; Mahoney, W.; Osifchin, R. G.; Reifenberger, R. “Coulomb Staircase” at Room Temperature in a Self-Assembled Molecular Nanostructure. *Science* **1996**, *272* (5266), 1323–1325.
- (7) Aradhya, S. V.; Frei, M.; Hybertsen, M. S.; Venkataraman, L. Van Der Waals Interactions at Metal/Organic Interfaces at the Single-Molecule Level. *Nat. Mater.* **2012**, *11* (10), 872–876.
- (8) Huang, M.; Sun, M.; Yu, X.; He, S.; Liu, S.; Nau, W. M.; Li, Y.; Wu, T.; Wang, Y.; Chang, S.; He, J. Reliably Probing the Conductance of a Molecule in a Cavity via van Der Waals Contacts. *J. Phys. Chem. C* **2020**, *124* (29), 16143–16148.
- (9) Zang, Y.; Pinkard, A.; Liu, Z. F.; Neaton, J. B.; Steigerwald, M. L.; Roy, X.; Venkataraman, L. Electronically Transparent Au-N Bonds for Molecular Junctions. *J. Am. Chem. Soc.* **2017**, *139* (42), 14845–14848.
- (10) Li, Z.; Park, T. H.; Rawson, J.; Therien, M. J.; Borguet, E. Quasi-Ohmic Single Molecule Charge Transport through Highly Conjugated Meso-to-Meso Ethyne-Bridged Porphyrin Wires. *Nano Lett.* **2012**, *12* (6), 2722–2727.
- (11) Li, L.; Low, J. Z.; Wilhelm, J.; Liao, G.; Gunasekaran, S.; Prindle, C. R.; Starr, R. L.; Golze, D.; Nuckolls, C.; Steigerwald, M. L.; Evers, F.; Campos, L. M.; Yin, X.; Venkataraman, L. Highly Conducting Single-Molecule Topological Insulators Based on Mono- and Di-Radical Cations. *Nat. Chem.* **2022**, *14* (9), 1061–1067.

- (12) Tanaka, Y.; Kato, Y.; Tada, T.; Fujii, S.; Kiguchi, M.; Akita, M. “doping” of Polyynes with an Organometallic Fragment Leads to Highly Conductive Metallapolyynes Molecular Wires. *J. Am. Chem. Soc.* **2018**, *140* (32), 10080–10084.
- (13) Li, L.; Louie, S.; Evans, A. M.; Meirzadeh, E.; Nuckolls, C. Topological Radical Pairs Produce Ultrahigh Conductance in Long Molecular Wires. *J. Am. Chem. Soc.* **2023**, *145* (4), 2492–2498.
- (14) Sun, Y. Y.; Peng, Z. L.; Hou, R.; Liang, J. H.; Zheng, J. F.; Zhou, X. S. Y. S.; Zhou, X. S. Y. S.; Jin, S.; Niu, Z. J.; Mao, B. W. Enhancing Electron Transport in Molecular Wires by Insertion of a Ferrocene Center. *Phys. Chem. Chem. Phys.* **2014**, *16* (6), 2260–2267.
- (15) Pan, X.; Lawson, B.; Rustad, A. M.; Kamenetska, M.; Kamenetska, M.; Kamenetska, M. PH-Activated Single Molecule Conductance and Binding Mechanism of Imidazole on Gold. *Nano Lett.* **2020**, *20* (6), 4687–4692.
- (16) Kamenetska, M.; Koentopp, M.; Whalley, A. C.; Park, Y. S.; Steigerwald, M. L.; Nuckolls, C.; Hybertsen, M. S.; Venkataraman, L. Formation and Evolution of Single-Molecule Junctions. *Phys. Rev. Lett.* **2009**, *102*, 126803.
- (17) Yanson, A. I.; Rubio Bollinger, G.; Van Den Brom, H. E.; Agrait, N.; Van Ruitenbeek, J. M. Formation and Manipulation of a Metallic Wire of Single Gold Atoms. *Nature* **1998**, *395* (6704), 783–785.
- (18) Landauer, R. Conductance Determined by Transmission: Probes and Quantised Constriction Resistance. *J. Phys. Condens. Matter* **1989**, *1* (43), 8099–8110.
- (19) Kittel, C. *Introduction to Solid State Physics*, 8th ed.; John Wiley & Sons, Ltd, 2005.
- (20) Cuevas, J. C.; Scheer, E. *Molecular Electronics: An Introduction to Theory and Experiment*, 2nd ed.; World Scientific Publishing Company, 2017.

- (21) Landauer, R. Spatial Variation of Currents and Fields Due to Localized Scatterers in Metallic Conduction. *J. Math. Phys.* **1996**, *37* (10), 5259–5268.
- (22) Datta, S. Electronic Transport in Mesoscopic Systems. Cambridge University Press: Cambridge, UK 1995.
- (23) Neaton, J. B.; Hybertsen, M. S.; Louie, S. G. Renormalization of Molecular Electronic Levels at Metal-Molecule Interfaces. *Phys. Rev. Lett.* **2006**, *97* (21), 1–4.
- (24) Li, X.; He, J.; Hihath, J.; Xu, B.; Lindsay, S. M.; Tao, N. Conductance of Single Alkanedithiols: Conduction Mechanism and Effect of Molecule-Electrode Contacts. *J. Am. Chem. Soc.* **2006**, *128* (6), 2135–2141.
- (25) He, J.; Chen, F.; Li, J.; Sankey, O. F.; Terazono, Y.; Herrero, C.; Gust, D.; Moore, T. A.; Moore, A. L.; Lindsay, S. M. Electronic Decay Constant of Carotenoid Polyenes from Single-Molecule Measurements. *J. Am. Chem. Soc.* **2005**, *127* (5), 1384–1385.
- (26) Venkataraman, L.; Klare, J. E.; Nuckolls, C.; Hybertsen, M. S.; Steigerwald, M. L. Dependence of Single-Molecule Junction Conductance on Molecular Conformation. *Nature* **2006**, *442* (7105), 904–907.
- (27) Yamada, R.; Kumazawa, H.; Noutoshi, T.; Tanaka, S.; Tada, H. Electrical Conductance of Oligothiophene Molecular Wires. *Nano Lett.* **2008**, *8* (4), 1237–1240.
- (28) Capozzi, B.; Dell, E. J.; Berkelbach, T. C.; Reichman, D. R.; Venkataraman, L.; Campos, L. M. Length-Dependent Conductance of Oligothiophenes. *J. Am. Chem. Soc.* **2014**, *136* (29), 10486–10492.
- (29) Su, T. A.; Li, H.; Steigerwald, M. L.; Venkataraman, L.; Nuckolls, C. Stereoelectronic Switching in Single-Molecule Junctions. *Nat. Chem.* **2015**, *7* (3),

215–220.

- (30) Su, T. A.; Li, H.; Klausen, R. S.; Kim, N. T.; Neupane, M.; Leighton, J. L.; Steigerwald, M. L.; Venkataraman, L.; Nuckolls, C. Silane and Germane Molecular Electronics. *Acc. Chem. Res.* **2017**, *50* (4), 1088–1095.
- (31) Shankar, R. *Principles of Quantum Mechanics*, 2nd ed.; Plenum Publishing: New York, N.Y., 1994.
- (32) Markussen, T.; Stadler, R.; Thygesen, K. S. The Relation between Structure and Quantum Interference in Single Molecule Junctions. *Nano Lett.* **2010**, *10* (10), 4260–4265.
- (33) Gunasekaran, S.; Greenwald, J. E.; Venkataraman, L. Visualizing Quantum Interference in Molecular Junctions. *Nano Lett.* **2020**, *20* (4), 2843–2848.
- (34) Guédon, C. M.; Valkenier, H.; Markussen, T.; Thygesen, K. S.; Hummelen, J. C.; Van Der Molen, S. J. Observation of Quantum Interference in Molecular Charge Transport. *Nat. Nanotechnol.* **2012**, *7* (5), 305–309.
- (35) Camarasa-Gómez, M.; Hernangómez-Pérez, D.; Inkpen, M. S.; Lovat, G.; Fung, E. D.; Roy, X.; Venkataraman, L.; Evers, F. Mechanically Tunable Quantum Interference in Ferrocene-Based Single-Molecule Junctions. *Nano Lett.* **2020**, *20* (9), 6381–6386.
- (36) Zhao, X.; Kastlunger, G.; Stadler, R. Quantum Interference in Coherent Tunneling through Branched Molecular Junctions Containing Ferrocene Centers. *Phys. Rev. B* **2017**, *96* (8), 085421.
- (37) Su, W. P.; Schrieffer, J. R.; Heeger, A. J. Solitons in Polyacetylene. *Phys. Rev. Lett.* **1979**, *42* (25), 1698–1701.
- (38) Heeger, A. J.; Kivelson, S.; Schrieffer, J. R.; Su, W. P. Solitons in Conducting

Polymers. *Rev. Mod. Phys.* **1988**, *60* (3), 781–850.

- (39) Li, L.; Gunasekaran, S.; Wei, Y.; Nuckolls, C.; Venkataraman, L. Reversed Conductance Decay of 1D Topological Insulators by Tight-Binding Analysis. *J. Phys. Chem. Lett.* **2022**, *13* (41), 9703–9710.
- (40) Farzadi, R.; Milani Moghaddam, H. Greatly Enhanced Spin Filtering of Single Ferrocene Devices: An Ab Initio Study. *Org. Electron.* **2018**, *62* (August), 227–233.
- (41) Ahn, S.; Aradhya, S. V.; Klausen, R. S.; Capozzi, B.; Roy, X.; Steigerwald, M. L.; Nuckolls, C.; Venkataraman, L. Electronic Transport and Mechanical Stability of Carboxyl Linked Single-Molecule Junctions. *Phys. Chem. Chem. Phys.* **2012**, *14* (40), 13841–13845.
- (42) Adak, O.; Korytár, R.; Joe, A. Y.; Evers, F.; Venkataraman, L. Impact of Electrode Density of States on Transport through Pyridine-Linked Single Molecule Junctions. *Nano Lett.* **2015**, *15* (6), 3716–3722.
- (43) Quek, S. Y.; Kamenetska, M.; Steigerwald, M. L.; Choi, H. J.; Louie, S. G.; Hybertsen, M. S.; Neaton, J. B.; Venkataraman, L. Mechanically Controlled Binary Conductance Switching of a Single-Molecule Junction. *Nat. Nanotechnol.* **2009**, *4* (4), 230–234.
- (44) Venkataraman, L.; Klare, J. E.; Tam, I. W.; Nuckolls, C.; Hybertsen, M. S.; Steigerwald, M. L. Single-Molecule Circuits with Well-Defined Molecular Conductance. *Nano Lett.* **2006**, *6* (3), 458–462.
- (45) Hybertsen, M. S.; Venkataraman, L.; Klare, J. E.; Whalley, A. C.; Steigerwald, M. L.; Nuckolls, C. Amine-Linked Single-Molecule Circuits: Systematic Trends across Molecular Families. *J. Phys. Condens. Matter* **2008**, *20* (37), 374115.
- (46) Park, Y. S.; Whalley, A. C.; Kamenetska, M.; Steigerwald, M. L.; Hybertsen, M.

- S.; Nuckolls, C.; Venkataraman, L. Contact Chemistry and Single-Molecule Conductance: A Comparison of Phosphines, Methyl Sulfides, and Amines. *J. Am. Chem. Soc.* **2007**, *129* (51), 15768–15769.
- (47) Chen, F.; Peng, L. L.; Hong, Z. W.; Mao, J. C.; Zheng, J. F.; Shao, Y.; Niu, Z. J.; Zhou, X. S. Comparative Study on Single-Molecule Junctions of Alkane- and Benzene-Based Molecules with Carboxylic Acid/Aldehyde as the Anchoring Groups. *Nanoscale Res. Lett.* **2016**, *11* (1), 1–5.
- (48) Kamenetska, M.; Quek, S. Y.; Whalley, A. C.; Steigerwald, M. L.; Choi, H. J.; Louie, S. G.; Nuckolls, C.; Hybertsen, M. S.; Neaton, J. B.; Venkataraman, L. Conductance and Geometry of Pyridine-Linked Single-Molecule Junctions. *J. Am. Chem. Soc.* **2010**, *132* (19), 6817–6821.
- (49) Chen, F.; Li, X.; Hihath, J.; Huang, Z.; Tao, N. Effect of Anchoring Groups on Single-Molecule Conductance: Comparative Study of Thiol-, Amine-, and Carboxylic-Acid-Terminated Molecules. *J. Am. Chem. Soc.* **2006**, *128* (49), 15874–15881.
- (50) Leary, E.; La Rosa, A.; González, M. T.; Rubio-Bollinger, G.; Agraït, N.; Martín, N. Incorporating Single Molecules into Electrical Circuits. the Role of the Chemical Anchoring Group. *Chem. Soc. Rev.* **2015**, *44* (4), 920–942.
- (51) Ulrich, J.; Esrail, D.; Pontius, W.; Venkataraman, L.; Millar, D.; Doerrer, L. H. Variability of Conductance in Molecular Junctions. *J. Phys. Chem. B* **2006**, *110* (6), 2462–2466.
- (52) Capozzi, B.; Xia, J.; Adak, O.; Dell, E. J.; Liu, Z. F.; Taylor, J. C.; Neaton, J. B.; Campos, L. M.; Venkataraman, L. Single-Molecule Diodes with High Rectification Ratios through Environmental Control. *Nat. Nanotechnol.* **2015**, *10* (6), 522–527.

- (53) Tao, C. P.; Jiang, C. C.; Wang, Y. H.; Zheng, J. F.; Shao, Y.; Zhou, X. S. Single-Molecule Sensing of Interfacial Acid-Base Chemistry. *J. Phys. Chem. Lett.* **2020**, *11* (23), 10023–10028.
- (54) Li, Z.; Smeu, M.; Afsari, S.; Xing, Y.; Ratner, M. A.; Borguet, E. Single-Molecule Sensing of Environmental PH - An STM Break Junction and NEGF-DFT Approach. *Angew. Chemie - Int. Ed.* **2014**, *53* (4), 1098–1102.
- (55) Wu, B.; Guo, W.; An, J.; Li, H. Control of Molecular Conductance by PH. *J. Mater. Chem. C* **2022**, *10* (37), 13483–13498.
- (56) Kim, T.; Vázquez, H.; Hybertsen, M. S.; Venkataraman, L. Conductance of Molecular Junctions Formed with Silver Electrodes. *Nano Lett.* **2013**, *13* (7), 3358–3364.
- (57) Li, H.; Su, T. A.; Camarasa-Gómez, M.; Hernangómez-Pérez, D.; Henn, S. E.; Pokorný, V.; Caniglia, C. D.; Inkpen, M. S.; Korytár, R.; Steigerwald, M. L.; Nuckolls, C.; Evers, F.; Venkataraman, L. Silver Makes Better Electrical Contacts to Thiol-Terminated Silanes than Gold. *Angew. Chemie - Int. Ed.* **2017**, *56* (45), 14145–14148.
- (58) Makk, P.; Tomaszewski, D.; Martinek, J.; Balogh, Z.; Csonka, S.; Wawrzyniak, M.; Frei, M.; Venkataraman, L.; Halbritter, A. Correlation Analysis of Atomic and Single-Molecule Junction Conductance. *ACS Nano* **2012**, *6* (4), 3411–3423.
- (59) Kiguchi, M.; Tal, O.; Wohlthat, S.; Pauly, F.; Krieger, M.; Djukic, D.; Cuevas, J. C.; Van Ruitenbeek, J. M. Highly Conductive Molecular Junctions Based on Direct Binding of Benzene to Platinum Electrodes. *Phys. Rev. Lett.* **2008**, *101* (4), 1–4.
- (60) Brooke, R. J.; Jin, C.; Szumski, D. S.; Nichols, R. J.; Mao, B. W.; Thygesen, K. S.; Schwarzacher, W. Single-Molecule Electrochemical Transistor Utilizing a Nickel-

Pyridyl Spinterface. *Nano Lett.* **2015**, *15* (1), 275–280.

- (61) Hong, Z. W.; Chen, F.; Wang, Y. H.; Mao, J. C.; Li, D. F.; Tang, Y.; Shao, Y.; Niu, Z. J.; Zhou, X. S. The Binding Sites of Carboxylic Acid Group Contacting to Cu Electrode. *Electrochem. commun.* **2015**, *59*, 48–51.
- (62) Zhao, S.; Chen, H.; Qian, Q.; Zhang, H.; Yang, Y.; Hong, W. Non-Covalent Interaction-Based Molecular Electronics with Graphene Electrodes. *Nano Res.* **2021**, *16*, 5436–5446.
- (63) Yang, C.; Qin, A.; Tang, B. Z.; Guo, X. Fabrication and Functions of Graphene-Molecule-Graphene Single-Molecule Junctions. *J. Chem. Phys.* **2020**, *152* (12).
- (64) Villalva, J.; Develioglu, A.; Montenegro-Pohlhammer, N.; Sánchez-de-Armas, R.; Gamonal, A.; Rial, E.; García-Hernández, M.; Ruiz-Gonzalez, L.; Costa, J. S.; Calzado, C. J.; Pérez, E. M.; Burzurí, E. Spin-State-Dependent Electrical Conductivity in Single-Walled Carbon Nanotubes Encapsulating Spin-Crossover Molecules. *Nat. Commun.* **2021**, *12* (1), 1–8.
- (65) Aradhya, S. V.; Frei, M.; Halbritter, A.; Venkataraman, L. Correlating Structure, Conductance, and Mechanics of Silver Atomic-Scale Contacts. *ACS Nano* **2013**, *7* (4), 3706–3712.
- (66) Lawson, B.; Zahl, P.; Hybertsen, M. S.; Kamenetska, M. Formation and Evolution of Metallocene Single-Molecule Circuits with Direct Gold-IIIlinks. *J. Am. Chem. Soc.* **2022**, *144* (14), 6504–6515.
- (67) Quek, S. Y.; Venkataraman, L.; Choi, H. J.; Louie, S. G.; Hybertsen, M. S.; Neaton, J. B. Amine - Gold Linked Single-Molecule Circuits: Experiment and Theory. *Nano Lett.* **2007**, *7* (11), 3477–3482.
- (68) Lawson, B.; Skipper, H. E.; Kamenetska, M. Phenol Is a PH-Activated Linker to Gold: A Single Molecule Conductance Study. *Nanoscale* **2024**.

- (69) Tanaka, Y.; Kiguchi, M.; Akita, M. Inorganic and Organometallic Molecular Wires for Single-Molecule Devices. *Chem. - A Eur. J.* **2017**, *23* (20), 4741–4749.
- (70) Higgins, S. J.; Nichols, R. J. Metal/Molecule/Metal Junction Studies of Organometallic and Coordination Complexes; What Can Transition Metals Do for Molecular Electronics? *Polyhedron* **2018**, *140*, 25–34.
- (71) Bock, S.; Al-Owaedi, O. A.; Eaves, S. G.; Milan, D. C.; Lemmer, M.; Skelton, B. W.; Osorio, H. M.; Nichols, R. J.; Higgins, S. J.; Cea, P.; Long, N. J.; Albrecht, T.; Martín, S.; Lambert, C. J.; Low, P. J. Single-Molecule Conductance Studies of Organometallic Complexes Bearing 3-Thienyl Contacting Groups. *Chem. - A Eur. J.* **2017**, *23* (9), 2133–2143.
- (72) Liu, Z. F.; Wei, S.; Yoon, H.; Adak, O.; Ponce, I.; Jiang, Y.; Jang, W. D.; Campos, L. M.; Venkataraman, L.; Neaton, J. B. Control of Single-Molecule Junction Conductance of Porphyrins via a Transition-Metal Center. *Nano Lett.* **2014**, *14* (9), 5365–5370.
- (73) Bredow, T.; Tegenkamp, C.; Pfnür, H.; Meyer, J.; Maslyuk, V. V.; Mertig, I. Ferrocene-1,1' -Dithiol as Molecular Wire between Ag Electrodes: The Role of Surface Defects. *J. Chem. Phys.* **2008**, *128*, 064704.
- (74) Lu, Q.; Yao, C.; Wang, X.; Wang, F. Enhancing Molecular Conductance of Oligo(p-Phenylene Ethynylene)s by Incorporating Ferrocene into Their Backbones. *J. Phys. Chem. C* **2012**, *116* (33), 17853–17861.
- (75) Yu, J. X.; Chang, J.; Wei, R. K.; Liu, X. Y.; Li, X. D. Quantum Transport of the Single Metallocene Molecule. *Phys. E Low-Dimensional Syst. Nanostructures* **2016**, *84*, 294–297.
- (76) Getty, S. A.; Engtrakul, C.; Wang, L.; Liu, R.; Ke, S. H.; Baranger, H. U.; Yang, W.; Fuhrer, M. S.; Sita, L. R. Near-Perfect Conduction through a Ferrocene-Based

- Molecular Wire. *Phys. Rev. B - Condens. Matter Mater. Phys.* **2005**, *71*, 241401.
- (77) García-Suárez, V. M.; Ferrer, J.; Lambert, C. J. Electronic Properties of Metallocene Wires. *Proc. 2006 Int. Conf. Nanosci. Nanotechnology, ICONN 2006*, 43–45.
- (78) Farzadi, R.; Milani Moghaddam, H.; Farmanzadeh, D. Tuning the Spin Transport Properties of Ferrocene-Based Single Molecule Junctions by Different Linkers. *Chem. Phys. Lett.* **2018**, *704*, 37–44.
- (79) Broadnax, A. D.; Lamport, Z. A.; Scharmann, B.; Jurchescu, O. D.; Welker, M. E. Ferrocenealkylsilane Molecular Rectifiers. *J. Organomet. Chem.* **2018**, *856*, 23–26.
- (80) Li, Y.; Wang, H.; Wang, Z.; Qiao, Y.; Ulstrup, J.; Chen, H.-Y.; Zhou, G.; Tao, N. Transition from Stochastic Events to Deterministic Ensemble Average in Electron Transfer Reactions Revealed by Single-Molecule Conductance Measurement. *Proc. Natl. Acad. Sci.* **2019**, *116* (9), 3407–3412.
- (81) Uehara, T.; Belosludov, R. V.; Farajian, A. A.; Mizuseki, H.; Kawazoe, Y. Electronic and Transport Properties of Ferrocene: Theoretical Study. *Japanese J. Appl. Physics, Part 1 Regul. Pap. Short Notes Rev. Pap.* **2006**, *45* (4 B), 3768–3771.
- (82) Xiao, X.; Brune, D.; He, J.; Lindsay, S.; Gorman, C. B.; Tao, N. Redox-Gated Electron Transport in Electrically Wired Ferrocene Molecules. *Chem. Phys.* **2006**, *326* (1), 138–143.
- (83) Ormaza, M.; Abufager, P.; Verlhac, B.; Bachellier, N.; Bocquet, M. L.; Lorente, N.; Limot, L. Controlled Spin Switching in a Metallocene Molecular Junction. *Nat. Commun.* **2017**, *8*, 1974.
- (84) Mohr, M.; Gruber, M.; Weismann, A.; Jacob, D.; Abufager, P.; Lorente, N.;

- Berndt, R. Spin Dependent Transmission of Nickelocene-Cu Contacts Probed with Shot Noise. *Phys. Rev. B* **2020**, *101* (7), 75414.
- (85) Verlhac, B.; Bachellier, N.; Garnier, L.; Ormaza, M.; Abufager, P.; Robles, R.; Bocquet, M. L.; Ternes, M.; Lorente, N.; Limot, L. Atomic-Scale Spin Sensing with a Single Molecule at the Apex of a Scanning Tunneling Microscope. *Science* **2019**, *366* (6465), 623–627.
- (86) Pal, A. N.; Li, D.; Sarkar, S.; Chakrabarti, S.; Vilan, A.; Kronik, L.; Smogunov, A.; Tal, O. Nonmagnetic Single-Molecule Spin-Filter Based on Quantum Interference. *Nat. Commun.* **2019**, *10* (1), 5565.
- (87) McNeely, J.; Miller, N.; Pan, X.; Lawson, B.; Kamenetska, M. Angstrom-Scale Ruler Using Single Molecule Conductance Signatures. *J. Phys. Chem. C* **2020**, *124* (24), 13427–13433.
- (88) Kamenetska, M.; Widawsky, J. R.; Dell'Angela, M.; Frei, M.; Venkataraman, L. Temperature Dependent Tunneling Conductance of Single Molecule Junctions. *J. Chem. Phys.* **2017**, *146* (9), 092311.
- (89) Yelin, T.; Chakrabarti, S.; Vilan, A.; Tal, O. Richness of Molecular Junction Configurations Revealed by Tracking a Full Pull-Push Cycle. *Nanoscale* **2021**, *13* (44), 18434–18440.
- (90) Kanthasamy, K.; Ring, M.; Nettelroth, D.; Tegenkamp, C.; Butenschön, H.; Pauly, F.; Pfnür, H. Charge Transport through Ferrocene 1,1'-Diamine Single-Molecule Junctions. *Small* **2016**, *12* (35), 4849–4856.
- (91) Zahl, P.; Klust, A. *Gxsm Software Project Homepage*. <http://gxsm.sourceforge.net>.
- (92) Zahl, P.; Wagner, T. GXSM - Smart & Customizable SPM Control. *Imaging & Microscopy (GIT)*. Imaging & Microscopy (GIT) 2015.

- (93) Kamenetska, M.; Dell'angela, M.; Widawsky, J. R.; Kladnik, G.; Verdini, A.; Cossaro, A.; Cvetko, D.; Morgante, A.; Venkataraman, L. Structure and Energy Level Alignment of Tetramethyl Benzenediamine on Au(111). *J. Phys. Chem. C* **2011**, *115* (25), 12625–12630.
- (94) Braun, K. F.; Iancu, V.; Pertaya, N.; Rieder, K. H.; Hla, S. W. Decompositional Incommensurate Growth of Ferrocene Molecules on a Au(111) Surface. *Phys. Rev. Lett.* **2006**, *96* (24), 246102.
- (95) Knaak, T.; González, C.; Dappe, Y. J.; Harzmann, G. D.; Brandl, T.; Mayor, M.; Berndt, R.; Gruber, M. Fragmentation and Distortion of Terpyridine-Based Spin-Crossover Complexes on Au(111). *J. Phys. Chem. C* **2019**, *123* (7), 4178–4185.
- (96) Skipper, H. E.; May, C. V.; Rheingold, A. L.; Doerrer, L. H.; Kamenetska, M. Hard-Soft Chemistry Design Principles for Predictive Assembly of Single Molecule-Metal Junctions. *J. Am. Chem. Soc.* **2021**, *143* (40), 16439–16447.
- (97) Untiedt, C.; Yanson, A. I.; Grande, R.; Rubio-Bollinger, G.; Agraït, N.; Vieira, S.; van Ruitenbeek, J. M. Calibration of the Length of a Chain of Single Gold Atoms. *Phys. Rev. B* **2002**, *66* (8), 085418.
- (98) Trouwborst, M. L.; Huisman, E. H.; Bakker, F. L.; Van Der Molen, S. J.; Van Wees, B. J. Single Atom Adhesion in Optimized Gold Nanojunctions. *Phys. Rev. Lett.* **2008**, *100* (17), 175502.
- (99) Leary, E.; Zotti, L. A.; Miguel, D.; Márquez, I. R.; Palomino-Ruiz, L.; Cuerva, J. M.; Rubio-Bollinger, G.; González, M. T.; Agraït, N. The Role of Oligomeric Gold-Thiolate Units in Single-Molecule Junctions of Thiol-Anchored Molecules. *J. Phys. Chem. C* **2018**, *122* (6), 3211–3218.
- (100) Cabosart, D.; El Abbassi, M.; Stefani, D.; Frisenda, R.; Calame, M.; Van der Zant, H. S. J.; Perrin, M. L. A Reference-Free Clustering Method for the Analysis of

- Molecular Break-Junction Measurements. *Appl. Phys. Lett.* **2019**, *114* (14).
- (101) Hamill, J. M.; Zhao, X. T.; Mészáros, G.; Bryce, M. R.; Arenz, M. Fast Data Sorting with Modified Principal Component Analysis to Distinguish Unique Single Molecular Break Junction Trajectories. *Phys. Rev. Lett.* **2018**, *120* (1).
- (102) Lemmer, M.; Inkpen, M. S.; Kornysheva, K.; Long, N. J.; Albrecht, T. Unsupervised Vector-Based Classification of Single-Molecule Charge Transport Data. *Nat. Commun.* **2016**, *7* (May), 1–10.
- (103) Blum, V.; Gehrke, R.; Hanke, F.; Havu, P.; Havu, V.; Ren, X.; Reuter, K.; Scheffler, M. Ab Initio Molecular Simulations with Numeric Atom-Centered Orbitals. *Comput. Phys. Commun.* **2009**, *180* (11), 2175–2196.
- (104) Ren, X.; Rinke, P.; Blum, V.; Wieferink, J.; Tkatchenko, A.; Sanfilippo, A.; Reuter, K.; Scheffler, M. Resolution-of-Identity Approach to Hartree-Fock, Hybrid Density Functionals, RPA, MP2 and GW with Numeric Atom-Centered Orbital Basis Functions. *New J. Phys.* **2012**, *14*, 053020.
- (105) Arnold, A.; Weigend, F.; Evers, F. Quantum Chemistry Calculations for Molecules Coupled to Reservoirs: Formalism, Implementation, and Application to Benzenedithiol. *J. Chem. Phys.* **2007**, *126* (17), 174101.
- (106) Bagrets, A. Spin-Polarized Electron Transport across Metal-Organic Molecules: A Density Functional Theory Approach. *J. Chem. Theory Comput.* **2013**, *9* (6), 2801–2815.
- (107) Wilhelm, J.; Walz, M.; Stendel, M.; Bagrets, A.; Evers, F. Ab Initio Simulations of Scanning-Tunneling-Microscope Images with Embedding Techniques and Application to C58-Dimers on Au(111). *Phys. Chem. Chem. Phys.* **2013**, *15* (18), 6684–6690.
- (108) Perdew, J. P.; Burke, K.; Ernzerhof, M. Generalized Gradient Approximation

- Made Simple. *Phys. Rev. Lett.* **1996**, 77 (18), 3865–3868.
- (109) Tkatchenko, A.; Scheffler, M. Accurate Molecular van Der Waals Interactions from Ground-State Electron Density and Free-Atom Reference Data. *Phys. Rev. Lett.* **2009**, 102 (7), 073005.
- (110) Li, H. B.; Xi, Y.-F.; Hong, Z.-W.; Yu, J.; Li, X.-X.; Liu, W.-X.; Domulevicz, L.; Jin, S.; Zhou, X.-S.; Hihath, J. Temperature-Dependent Tunneling in Furan Oligomer Single-Molecule Junctions. *ACS Sensors* **2021**, 6, 565–572.
- (111) Yanson, A. I.; Rubio Bollinger, G.; Van Den Brom, H. E.; Agraït, N.; Van Ruitenbeek, J. M. Formation and Manipulation of a Metallic Wire of Single Gold Atoms. *Nature* **1998**, 395 (6704), 783–785.
- (112) Agraït, N.; Yeyati, A. L.; van Ruitenbeek, J. M. Quantum Properties of Atomic-Sized Conductors. *Phys. Rep.* **2003**, 377 (2–3), 81–279.
- (113) Ohnishi, H.; Kondo, Y.; Takayanagi, K. Quantized Conductance through Individual Rows of Suspended Gold Atoms. *Nature* **1998**, 395 (6704), 780–783.
- (114) Rodrigues, V.; Fuhrer, T.; Ugarte, D. Signature of Atomic Structure in the Quantum Conductance of Gold Nanowires. *Phys. Rev. Lett.* **2000**, 85 (19), 4124–4127.
- (115) Li, S.; Jiang, Y.; Wang, Y.; Hou, S. The Formation and Conducting Mechanism of Imidazole-Gold Molecular Junctions. *ChemistrySelect* **2021**, 6 (12), 2959–2965.
- (116) Hines, T.; Diez-Perez, I.; Hihath, J.; Liu, H.; Wang, Z.-S.; Zhao, J.; Zhou, G.; Müllen, K.; Tao, N. Transition from Tunneling to Hopping in Single Molecular Junctions by Measuring Length and Temperature Dependence. *J. Am. Chem. Soc.* **2010**, 132 (33), 11658–11664.
- (117) Leary, E.; Höbenreich, H.; Higgins, S. J.; Zalinge, H. van; Haiss, W.; Nichols, R.

- J.; Finch, C. M.; Grace, I.; Lambert, C. J.; McGrath, R.; Smerdon, J. Single-Molecule Solvation-Shell Sensing. *Phys. Rev. Lett.* **2009**, *102* (8), 086801.
- (118) Sohn, Y. S.; Hendrickson, D. N.; Gray, H. B. Electronic Structure of Ferricenium Ion Sir: *J. Am. Chem. Soc.* **1970**, *92* (10), 3233–3234.
- (119) Yamaguchi, Y.; Ding, W.; Sanderson, C. T.; Borden, M. L.; Morgan, M. J.; Kutal, C. Electronic Structure, Spectroscopy, and Photochemistry of Group 8 Metallocenes. *Coord. Chem. Rev.* **2007**, *251* (3–4), 515–524.
- (120) Atkins, A. J.; Bauer, M.; Jacob, C. R. The Chemical Sensitivity of X-Ray Spectroscopy: High Energy Resolution XANES versus X-Ray Emission Spectroscopy of Substituted Ferrocenes. *Phys. Chem. Chem. Phys.* **2013**, *15* (21), 8095–8105.
- (121) Haaland, A. Molecular Structure and Bonding in the 3d Metallocenes. *Acc. Chem. Res.* **1979**, *12* (11), 415–422.
- (122) Bean, D. E.; Fowler, P. W.; Morris, M. J. Aromaticity and Ring Currents in Ferrocene and Two Isomeric Sandwich Complexes. *J. Organomet. Chem.* **2011**, *696* (10), 2093–2100.
- (123) Ormaza, M.; Abufager, P.; Bachellier, N.; Robles, R.; Verot, M.; Le Bahers, T.; Bocquet, M. L.; Lorente, N.; Limot, L. Assembly of Ferrocene Molecules on Metal Surfaces Revisited. *J. Phys. Chem. Lett.* **2015**, *6* (3), 395–400.
- (124) Bachellier, N.; Ormaza, M.; Faraggi, M.; Verlhac, B.; Vérot, M.; Le Bahers, T.; Bocquet, M. L.; Limot, L. Unveiling Nickelocene Bonding to a Noble Metal Surface. *Phys. Rev. B* **2016**, *93* (19), 195403.
- (125) Toher, C.; Filippetti, A.; Sanvito, S.; Burke, K. Self-Interaction Errors in Density-Functional Calculations of Electronic Transport. *Phys. Rev. Lett.* **2005**, *95* (14), 146402.

- (126) Koentopp, M.; Burke, K.; Evers, F. Zero-Bias Molecular Electronics: Exchange-Correlation Corrections to Landauer's Formula. *Phys. Rev. B - Condens. Matter Mater. Phys.* **2006**, *73* (12), 121403.
- (127) Ke, S. H.; Baranger, H. U.; Yang, W. Role of the Exchange-Correlation Potential in Ab Initio Electron Transport Calculations. *J. Chem. Phys.* **2007**, *126* (20), 201102.
- (128) Evers, F.; Korytár, R.; Tewari, S.; Van Ruitenbeek, J. M. Advances and Challenges in Single-Molecule Electron Transport. *Rev. Mod. Phys.* **2020**, *92* (3), 035001.
- (129) Fatemi, V.; Kamenetska, M.; Neaton, J. B.; Venkataraman, L. Environmental Control of Single-Molecule Junction Transport. *Nano Lett.* **2011**, *11* (5), 1988–1992.
- (130) Nguyen, K. T.; Lane, E. E.; McMillen, C. D.; Pienkos, J. A.; Wagenknecht, P. S. Is Indenyl a Stronger or Weaker Electron Donor Ligand than Cyclopentadienyl? Opposing Effects of Indenyl Electron Density and Ring Slipping on Electrochemical Potentials. *Organometallics* **2020**, *39* (5), 670–678.
- (131) Kaneko, S.; Nakazumi, T.; Kiguchi, M. Fabrication of a Well-Defined Single Benzene Molecule Junction Using Ag Electrodes. *J. Phys. Chem. Lett.* **2010**, *1* (24), 3520–3523.
- (132) Su, T. A.; Neupane, M.; Steigerwald, M. L.; Venkataraman, L.; Nuckolls, C. Chemical Principles of Single-Molecule Electronics. *Nat. Rev. Mater.* **2016**, *1*, 16002.
- (133) A. Martin, C.; Ding, D.; Kryger Sørensen, J.; Bjørnholm, T.; M. van Ruitenbeek, J.; S. J. van der Zant, H. Fullerene-Based Anchoring Groups for Molecular Electronics. *J. Am. Chem. Soc.* **2008**, *130* (40), 13198–13199.

- (134) Cheng, Z. L.; Skouta, R.; Vazquez, H.; Widawsky, J. R.; Schneebeli, S.; Chen, W.; Hybertsen, M. S.; Breslow, R.; Venkataraman, L. In Situ Formation of Highly Conducting Covalent Au-C Contacts for Single-Molecule Junctions. *Nat. Nanotechnol.* **2011**, *6* (6), 353–357.
- (135) Chen, W.; Widawsky, J. R.; Vázquez, H.; Schneebeli, S. T.; Hybertsen, M. S.; Breslow, R.; Venkataraman, L. Highly Conducting  $\pi$ -Conjugated Molecular Junctions Covalently Bonded to Gold Electrodes. *J. Am. Chem. Soc.* **2011**, *133* (43), 17160–17163.
- (136) Pacchioni, G. A Not-so-Strong Bond. *Nat. Rev. Mater.* **2019**, *4* (4), 226.
- (137) Parameswaran, R.; Widawsky, J. R.; Vázquez, H.; Park, Y. S.; Boardman, B. M.; Nuckolls, C.; Steigerwald, M. L.; Hybertsen, M. S.; Venkataraman, L. Reliable Formation of Single Molecule Junctions with Air-Stable Diphenylphosphine Linkers. *J. Phys. Chem. Lett.* **2010**, *1* (14), 2114–2119.
- (138) Hong, Z. W.; Aissa, M. A. Ben; Peng, L. L.; Xie, H.; Chen, D. L.; Zheng, J. F.; Shao, Y.; Zhou, X. S.; Raouafi, N.; Niu, Z. J. Quantum Interference Effect of Single-Molecule Conductance Influenced by Insertion of Different Alkyl Length. *Electrochem. commun.* **2016**, *68*, 86–89.
- (139) Li, W. Q.; Huang, B.; Huang, M. L.; Peng, L. L.; Hong, Z. W.; Zheng, J. F.; Chen, W. B.; Li, J. F.; Zhou, X. S. Detecting Electron Transport of Amino Acids by Using Conductance Measurement. *Sensors (Switzerland)* **2017**, *17* (4), 1–8.
- (140) Mishchenko, A.; Zotti, L. A.; Vonlanthen, D.; Bürkle, M.; Pauly, F.; Cuevas, J. C.; Mayor, M.; Wandlowski, T. Single-Molecule Junctions Based on Nitrile-Terminated Biphenyls: A Promising New Anchoring Group. *J. Am. Chem. Soc.* **2011**, *133* (2), 184–187.
- (141) Wu, C.; Alqahtani, A.; Sangtarash, S.; Vezzoli, A.; Sadeghi, H.; Robertson, C. M.;

- Cai, C.; Lambert, C. J.; Higgins, S. J.; Nichols, R. J. In Situ Formation of H-Bonding Imidazole Chains in Break-Junction Experiments. *Nanoscale* **2020**, *12* (14), 7914–7920.
- (142) Fu, T.; Smith, S.; Camarasa-Gómez, M.; Yu, X.; Xue, J.; Nuckolls, C.; Evers, F.; Venkataraman, L.; Wei, S. Enhanced Coupling through  $\pi$ -Stacking in Imidazole-Based Molecular Junctions. *Chem. Sci.* **2019**, *10*, 9998–10002.
- (143) Miessler, G. L.; Fischer, P. J.; Tarr, D. A. *Inorganic Chemistry*, 5th ed.; Pearson Education Inc., 2014.
- (144) Menachekanian, S.; Mora Perez, C.; Pennathur, A. K.; Voegtle, M. J.; Blauth, D.; Prezhdo, O. V.; Dawlaty, J. M. Phenol as a Tethering Group to Gold Surfaces: Stark Response and Comparison to Benzenethiol. *J. Phys. Chem. Lett.* **2023**, 8353–8359.
- (145) Huang, M.; Zhou, Q.; Liang, F.; Yu, L.; Xiao, B.; Li, Y.; Zhang, M.; Chen, Y.; He, J.; Xiao, S.; Chang, S. Detecting Individual Bond Switching within Amides in a Tunneling Junction. *Nano Lett.* **2021**, *21* (12), 5409–5414.
- (146) Huang, J. R.; Huang, H.; Tao, C. P.; Zheng, J. F.; Yuan, Y.; Hong, Z. W.; Shao, Y.; Niu, Z. J.; Chen, J. Z.; Zhou, X. S. Controlling Contact Configuration of Carboxylic Acid-Based Molecular Junctions Through Side Group. *Nanoscale Res. Lett.* **2019**, *14* (1), 253.
- (147) Tong, L.; Yu, Z.; Gao, Y. J.; Li, X. C.; Zheng, J. F.; Shao, Y.; Wang, Y. H.; Zhou, X. S. Local Cation-Tuned Reversible Single-Molecule Switch in Electric Double Layer. *Nat. Commun.* **2023**, *14* (1), 3397.
- (148) Nagahara, L. A.; Thundat, T.; Lindsay, S. M. Preparation and Characterization of STM Tips for Electrochemical Studies. *Rev. Sci. Instrum.* **1989**, *60* (10), 3128–3130.

- (149) Morse, P. M. Diatomic Molecules According to the Wave Mechanics. II. Vibrational Levels. *Phys. Rev.* **1929**, *34* (1927), 57–64.
- (150) Girifalco, L. A.; Weizer, V. G. Application of the Morse Potential Function to Cubic Metals. *Phys. Rev.* **1959**, *114* (3), 687–690.
- (151) Markussen, T.; Jin, C.; Thygesen, K. S. Quantitatively Accurate Calculations of Conductance and Thermopower of Molecular Junctions. *Phys. Status Solidi Basic Res.* **2013**, *250* (11), 2394–2402.
- (152) Widawsky, J. R.; Darancet, P.; Neaton, J. B.; Venkataraman, L. Simultaneous Determination of Conductance and Thermopower of Single Molecule Junctions. *Nano Lett.* **2012**, *12* (1), 354–358.
- (153) Montes, E.; Vázquez, H. Role of the Binding Motifs in the Energy Level Alignment and Conductance of Amine-Gold Linked Molecular Junctions within DFT and DFT +  $\Sigma$ . *Appl. Sci.* **2021**, *11* (2), 1–12.
- (154) Frisch, M. J.; Trucks, G. W.; Schlegel, H. B.; Scuseria, G. E.; Robb, M. A.; Cheeseman, J. R.; Scalmani, G.; Barone, V.; Petersson, G. A.; Nakatsuji, H.; Li, X.; Caricato, M.; Marenich, A. V.; Bloino, J.; Janesko, B. G.; Gomperts, R.; Mennucci, B.; Hratchian, H. P.; Ortiz, J. V.; Izmaylov, A. F.; Sonnenberg, J. L.; Williams-Young, D.; Ding, F.; Lipparini, F.; Egidi, F.; Goings, J.; Peng, B.; Petrone, A.; Henderson, T.; Ranasinghe, D.; Zakrzewski, V. G.; Gao, J.; Rega, N.; Zheng, G.; Liang, W.; Hada, M.; Ehara, M.; Toyota, K.; Fukuda, R.; Hasegawa, J.; Ishida, M.; Nakajima, T.; Honda, Y.; Kitao, O.; Nakai, H.; Vreven, T.; Throssell, K.; Montgomery, J. A., Jr.; Peralta, J. E.; Ogliaro, F.; Bearpark, M. J.; Heyd, J. J.; Brothers, E. N.; Kudin, K. N.; Staroverov, V. N.; Keith, T. A.; Kobayashi, R.; Normand, J.; Raghavachari, K.; Rendell, A. P.; Burant, J. C.; Iyengar, S. S.; Tomasi, J.; Cossi, M.; Millam, J. M.; Klene, M.; Adamo, C.; Cammi, R.; Ochterski, J. W.; Martin, R. L.; Morokuma, K.; Farkas, O.; Foresman, J. B.; Fox, D. J. GAUSSIAN 16. Wallingford, CT 2016.

- (155) Weigend, F.; Furche, F.; Ahlrichs, R. Gaussian Basis Sets of Quadruple Zeta Valence Quality for Atoms H-Kr. *J. Chem. Phys.* **2003**, *119* (24), 12753–12762.
- (156) Rappoport, D.; Furche, F. Property-Optimized Gaussian Basis Sets for Molecular Response Calculations. *J. Chem. Phys.* **2010**, *133* (13).
- (157) Smith, N. V.; Chen, C. T.; Weinert, M. Distance of the Image Plane from Metal Surfaces. *Phys. Rev. B* **1989**, *40* (11), 7565–7573.
- (158) Wu, S.; González, M. T.; Huber, R.; Grunder, S.; Mayor, M.; Schönenberger, C.; Calame, M. Molecular Junctions Based on Aromatic Coupling. *Nat. Nanotechnol.* **2008**, *3* (9), 569–574.
- (159) Martín, S.; Grace, I.; Bryce, M. R.; Wang, C.; Jitchati, R.; Batsanov, A. S.; Higgins, S. J.; Lambert, C. J.; Nichols, R. J. Identifying Diversity in Nanoscale Electrical Break Junctions. *J. Am. Chem. Soc.* **2010**, *132* (26), 9157–9164.
- (160) Mishchenko, A.; Vonlanthen, D.; Meded, V.; Bürkle, M.; Li, C.; Pobelov, I. V.; Bagrets, A.; Viljas, J. K.; Pauly, F.; Evers, F.; Mayor, M.; Wandlowski, T. Influence of Conformation on Conductance of Biphenyl-Dithiol Single-Molecule Contacts. *Nano Lett.* **2010**, *10* (1), 156–163.
- (161) Arroyo, C. R.; Leary, E.; Castellanos-Gómez, A.; Rubio-Bollinger, G.; González, M. T.; Agraït, N. Influence of Binding Groups on Molecular Junction Formation. *J. Am. Chem. Soc.* **2011**, *133* (36), 14313–14319.
- (162) Li, H.; Garner, M. H.; Su, T. A.; Jensen, A.; Inkpen, M. S.; Steigerwald, M. L.; Venkataraman, L.; Solomon, G. C.; Nuckolls, C. Extreme Conductance Suppression in Molecular Siloxanes. *J. Am. Chem. Soc.* **2017**, *139* (30), 10212–10215.
- (163) Klausen, R. S.; Widawsky, J. R.; Steigerwald, M. L.; Venkataraman, L.; Nuckolls, C. Conductive Molecular Silicon. *J. Am. Chem. Soc.* **2012**, *134* (10), 4541–4544.

- (164) Gulcur, M.; Moreno-García, P.; Zhao, X.; Baghernejad, M.; Batsanov, A. S.; Hong, W.; Bryce, M. R.; Wandlowski, T. The Synthesis of Functionalised Diaryltetraynes and Their Transport Properties in Single-Molecule Junctions. *Chem. - A Eur. J.* **2014**, *20* (16), 4653–4660.
- (165) Bryenton, K. R.; Adeleke, A. A.; Dale, S. G.; Johnson, E. R. Delocalization Error: The Greatest Outstanding Challenge in Density-Functional Theory. *Wiley Interdiscip. Rev. Comput. Mol. Sci.* **2023**, *13* (2), 29–32.
- (166) Jensen, F. Describing Anions by Density Functional Theory: Fractional Electron Affinity. *J. Chem. Theory Comput.* **2010**, *6* (9), 2726–2735.
- (167) Kim, M. C.; Sim, E.; Burke, K. Understanding and Reducing Errors in Density Functional Calculations. *Phys. Rev. Lett.* **2013**, *111* (7), 1–5.
- (168) Jarvis, S. P.; Taylor, S.; Baran, J. D.; Thompson, D.; Saywell, A.; Mangham, B.; Champness, N. R.; Larsson, J. A.; Moriarty, P. Physisorption Controls the Conformation and Density of States of an Adsorbed Porphyrin. *J. Phys. Chem. C* **2015**, *119* (50), 27982–27994.
- (169) Zhang, Q.; Zheng, X.; Kuang, G.; Wang, W.; Zhu, L.; Pang, R.; Shi, X.; Shang, X.; Huang, X.; Liu, P. N.; Lin, N. Single-Molecule Investigations of Conformation Adaptation of Porphyrins on Surfaces. *J. Phys. Chem. Lett.* **2017**, *8* (6), 1241–1247.
- (170) Ceccatto Dos Santos, A.; Herrera-Reinoza, N.; Pérez Paz, A.; Mowbray, D. J.; De Siervo, A. Reassessing the Adsorption Behavior and On-Surface Reactivity of a Brominated Porphyrin on Cu(111). *J. Phys. Chem. C* **2021**, *125* (31), 17164–17173.
- (171) Safari, M. R.; Matthes, F.; Ernst, K.-H.; Bürgler, D. E.; Schneider, C. M. Deposition of Chiral Heptahelicene Molecules on Ferromagnetic Co and Fe Thin-

Film Substrates. *Nanomaterials*. **2022**, 12, 19, 3281-3299.

- (172) Hoft, R. C.; Ford, M. J.; McDonagh, A. M.; Cortie, M. B. Adsorption of Amine Compounds on the Au(111) Surface: A Density Functional Study. *J. Phys. Chem. C* **2007**, 111 (37), 13886–13891.
- (173) Xue, Y.; Li, X.; Li, H.; Zhang, W. Quantifying Thiol-Gold Interactions towards the Efficient Strength Control. *Nat. Commun.* **2014**, 5, 4348.
- (174) Zhou, P.; Fu, Y.; Wang, M.; Qiu, R.; Wang, Y.; Stoddart, J. F.; Wang, Y.; Chen, H. Robust Single-Supramolecule Switches Operating in Response to Two Different Noncovalent Interactions. *J. Am. Chem. Soc.* **2023**, 145 (34), 18800–18811.
- (175) Zhu, Y.; Zhou, Y.; Ren, L.; Ye, J.; Wang, H.; Liu, X.; Huang, R.; Liu, H.; Liu, J.; Shi, J.; Gao, P.; Hong, W. Switching Quantum Interference in Single-Molecule Junctions by Mechanical Tuning. *Angew. Chemie - Int. Ed.* **2023**, 62 (19), 1–7.
- (176) Pei, L. Q.; Horsley, J. R.; Seng, J. W.; Liu, X.; Yeoh, Y. Q.; Yu, M. X.; Wu, X. H.; Abell, A. D.; Zheng, J. F.; Zhou, X. S.; Yu, J.; Jin, S. Mechanically Induced Switching between Two Discrete Conductance States: A Potential Single-Molecule Variable Resistor. *ACS Appl. Mater. Interfaces* **2021**, 13 (48), 57646–57653.
- (177) Gao, T.; Pan, Z.; Cai, Z.; Zheng, J.; Tang, C.; Yuan, S.; Zhao, S. qiang; Bai, H.; Yang, Y.; Shi, J.; Xiao, Z.; Liu, J.; Hong, W. Electric Field-Induced Switching among Multiple Conductance Pathways in Single-Molecule Junctions. *Chem. Commun.* **2021**, 57 (58), 7160–7163.
- (178) Wang, Z.; Palma, J. L.; Wang, H.; Liu, J.; Zhou, G.; Ajayakumar, M. R. Electrochemically Controlled Rectification in Symmetric Single-Molecule Junctions. *Proc. Natl. Acad. Sci.* **2022**, 119 (39), 1–9.

- (179) Yuan, S.; Zhou, Y.; Gao, T.; Chen, L.; Xu, W.; Duan, P.; Wang, J.; Pan, Z.; Tang, C.; Yang, Y.; Huang, R.; Xiao, Z.; Hong, W. Electric Field-Driven Folding of Single Molecules. *Chinese Chem. Lett.* **2024**, *35* (1), 108404.
- (180) Yin, X.; Zang, Y.; Zhu, L.; Low, J. Z.; Liu, Z. F.; Cui, J.; Neaton, J. B.; Venkataraman, L.; Campos, L. M. A Reversible Single-Molecule Switch Based on Activated Antiaromaticity. *Sci. Adv.* **2017**, *3* (10), 1–6.
- (181) Batra, A.; Meisner, J. S.; Darancet, P.; Chen, Q.; Steigerwald, M. L.; Nuckolls, C.; Venkataraman, L. Molecular Diodes Enabled by Quantum Interference. *Faraday Discuss.* **2014**, *174* (c), 79–89.
- (182) Yuan, L.; Nerngchamng, N.; Cao, L.; Hamoudi, H.; Del Barco, E.; Roemer, M.; Sriramula, R. K.; Thompson, D.; Nijhuis, C. A. Controlling the Direction of Rectification in a Molecular Diode. *Nat. Commun.* **2015**, 6324–6335.
- (183) Koepf, M.; Koenigsmann, C.; Ding, W.; Batra, A.; Negre, C. F. A.; Venkataraman, L.; Brudvig, G. W.; Batista, V. S.; Schmuttenmaer, C. A.; Crabtree, R. H. Controlling the Rectification Properties of Molecular Junctions through Molecule-Electrode Coupling. *Nanoscale* **2016**, *8* (36), 16357–16362.
- (184) Jago, D.; Liu, C.; Daaoub, A. H. S.; Gaschk, E.; Walkey, M. C.; Pulbrook, T.; Qiao, X.; Sobolev, A. N.; Moggach, S. A.; Costa-Milan, D.; Higgins, S. J.; Piggott, M. J.; Sadeghi, H.; Nichols, R. J.; Sangtarash, S.; Vezzoli, A.; Koutsantonis, G. A. An Orthogonal Conductance Pathway in Spiropyran for Well-Defined Electrosteric Switching Single-Molecule Junctions. *Small* **2023**, *2306334*, 1–8.
- (185) Yongjiu, L.; Xu, W.; Zhiye, W.; Jianghao, Z.; Haijian, C.; Lei, L.; Yunchuan, L.; Bohuai, X.; Shuai, C. Effect of Modified Thiophene Anchor on Molecule-Electrode Bonding. *Chinese J. Inorg. Chem.* **2023**, *39* (11), 1–6.
- (186) Yu, Z.; Li, J. Q.; Wang, Y. H.; Su, J. Q.; Fu, J. Y.; Zou, J. W.; Zheng, J. F.; Shao,

- Y.; Zhou, X. S. Visualizing an Electrochemically Induced Radical Cation of Bipyridine at Au(111)/Ionic Liquid Interfaces toward a Single-Molecule Switch. *Anal. Chem.* **2022**, *94* (3), 1823–1830.
- (187) Perrin, M. L.; Perrin, M. L.; Eelkema, R.; Thijssen, J.; Grozema, F. C.; Van Der Zant, H. S. J. Single-Molecule Functionality in Electronic Components Based on Orbital Resonances. *Phys. Chem. Chem. Phys.* **2020**, *22* (23), 12849–12866.
- (188) Lambert, C. J. Basic Concepts of Quantum Interference and Electron Transport in Single-Molecule Electronics. *Chem. Soc. Rev.* **2015**, *44* (4), 875–888.
- (189) Lambert, C. J. *Quantum Transport in Nanostructures and Molecules*, 1st ed.; IOP Publishing: Bristol, UK, 2021.
- (190) Lovley, D. R. Long-Range Electron Transport to Fe(III) Oxide via Pili with Metallic-like Conductivity. *Biochem. Soc. Trans.* **2012**, *40* (6), 1186–1190.
- (191) Sedghi, G.; García-Suárez, V. M.; Esdaile, L. J.; Anderson, H. L.; Lambert, C. J.; Martín, S.; Bethell, D.; Higgins, S. J.; Elliott, M.; Bennett, N.; MacDonald, J. E.; Nichols, R. J. Long-Range Electron Tunnelling in Oligo-Porphyrin Molecular Wires. *Nat. Nanotechnol.* **2011**, *6* (8), 517–523.
- (192) Xu, W.; Leary, E.; Sangtarash, S.; Jirasek, M.; González, M. T.; Christensen, K. E.; Abellán Vicente, L.; Agraït, N.; Higgins, S. J.; Nichols, R. J.; Lambert, C. J.; Anderson, H. L. A Peierls Transition in Long Polymethine Molecular Wires: Evolution of Molecular Geometry and Single-Molecule Conductance. *J. Am. Chem. Soc.* **2021**, *143* (48), 20472–20481.
- (193) Tanaka, Y.; Kato, Y.; Sugimoto, K.; Kawano, R.; Tada, T.; Fujii, S.; Kiguchi, M.; Akita, M. Single-Molecule Junctions of Multinuclear Organometallic Wires: Long-Range Carrier Transport Brought about by Metal-Metal Interaction. *Chem. Sci.* **2021**, *12* (12), 4338–4344.

- (194) Park, J. W.; Do, E.; Shin, J. S.; Song, S. K.; Stetsovych, O.; Jelinek, P.; Yeom, H. W. Creation and Annihilation of Mobile Fractional Solitons in Atomic Chains. *Nat. Nanotechnol.* **2022**, *17* (3), 244–249.
- (195) Dressler, J. J.; Teraoka, M.; Espejo, G. L.; Kishi, R.; Takamuku, S.; Gómez-García, C. J.; Zakharov, L. N.; Nakano, M.; Casado, J.; Haley, M. M. Thiophene and Its Sulfur Inhibit Indenoindenodibenzothiophene Diradicals from Low-Energy Lying Thermal Triplets. *Nat. Chem.* **2018**, *10* (11), 1134–1140.
- (196) Choppella, S.; Paramasivam, G.; Sambasivam, S.; Ravva, M. K. Understanding the Stability of  $\pi$ -Conjugated Diradicaloid Organic Molecules. *J. Electron. Mater.* **2023**, *52* (3), 1681–1690.
- (197) Dressler, J. J.; Haley, M. M. Learning How to Fine-Tune Diradical Properties by Structure Refinement. *J. Phys. Org. Chem.* **2020**, *33*, 1–13.
- (198) Frederickson, C. K.; Rose, B. D.; Haley, M. M. Explorations of the Indenofluorenes and Expanded Quinoidal Analogues. *Acc. Chem. Res.* **2017**, *50* (4), 977–987.
- (199) Rudebusch, G. E.; Zafra, J. L.; Jorner, K.; Fukuda, K.; Marshall, J. L.; Arrechea-Marcos, I.; Espejo, G. L.; Ponce Ortiz, R.; Gómez-García, C. J.; Zakharov, L. N.; Nakano, M.; Ottosson, H.; Casado, J.; Haley, M. M. Diindeno-Fusion of an Anthracene as a Design Strategy for Stable Organic Biradicals. *Nat. Chem.* **2016**, *8* (8), 753–759.
- (200) Hayashi, H.; Barker, J. E.; Cárdenas Valdivia, A.; Kishi, R.; Macmillan, S. N.; Gómez-García, C. J.; Miyauchi, H.; Nakamura, Y.; Nakano, M.; Kato, S. I.; Haley, M. M.; Casado, J. Monoradicals and Diradicals of Dibenzofluoreno[3,2-b]fluorene Isomers: Mechanisms of Electronic Delocalization. *J. Am. Chem. Soc.* **2020**, *142* (48), 20444–20455.

- (201) Li, S.; Yu, H.; Li, J.; Angello, N.; Jira, E. R.; Li, B.; Burke, M. D.; Moore, J. S.; Schroeder, C. M. Transition between Nonresonant and Resonant Charge Transport in Molecular Junctions. *Nano Lett.* **2021**, *21* (19), 8340–8347.
- (202) Tsuji, Y.; Movassagh, R.; Datta, S.; Hoffmann, R. Exponential Attenuation of Through-Bond Transmission in a Polyene: Theory and Potential Realizations. *ACS Nano* **2015**, *9* (11), 11109–11120.
- (203) Li, L.; Nuckolls, C.; Venkataraman, L. Designing Long and Highly Conducting Molecular Wires with Multiple Nontrivial Topological States. *J. Phys. Chem. Lett.* **2023**, *14*, 5141–5147.

**CURRICULUM VITAE**

